

Instituto Tecnológico y de Estudios Superiores de Monterrey

Campus Monterrey

School of Engineering and Sciences



**Thermo-hydraulic performance modeling of thermal energy systems
using parabolic trough solar collectors**

A dissertation presented by

Pablo Daniel Tagle Salazar

**Submitted to the
School of Engineering and Sciences
in partial fulfillment of the requirements for the degree of**

Doctor of Philosophy

In

Engineering Science

Major in Environmental Systems and Energy

Monterrey Nuevo León, December 26th, 2018

Instituto Tecnológico y de Estudios Superiores de Monterrey

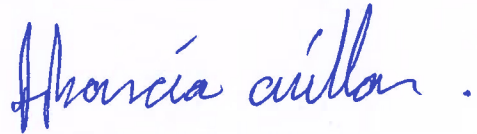
Campus Monterrey

School of Engineering and Sciences

The committee members, hereby, certify that have read the dissertation presented by Pablo Daniel Tagle Salazar and that it is fully adequate in scope and quality as a partial requirement for the degree of Doctor of Philosophy in Engineering Sciences, with a major in Environmental Systems and Energy.



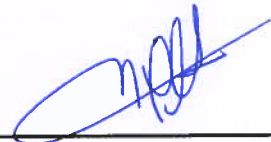
Dr. Carlos Iván Rivera Solorio
Tecnologico de Monterrey
School of Engineering and Sciences
Principal Advisor



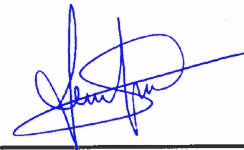
Dr. Alejandro Javier García Cuéllar
Tecnologico de Monterrey
School of Engineering and Sciences
Committee Member



Dr. Miguel Angel Gijón Rivera
Tecnologico de Monterrey
School of Engineering and Sciences
Committee Member or Co-advisor



Dr. José Luis López Salinas
Tecnologico de Monterrey
School of Engineering and Sciences
Committee Member



Dr. Loreto Valenzuela Gutiérrez
Plataforma Solar de Almería
Committee Member



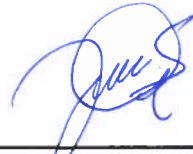
Dr. Rubén Morales Menéndez
Dean of Graduate Studies
School of Engineering and Sciences

Monterrey Nuevo León, December 26th, 2018

Declaration of Authorship

I, Pablo Daniel Tagle Salazar, declare that this dissertation titled, Thermo-hydraulic performance modeling of thermal energy systems using parabolic trough solar collectors and the work presented in it are my own. I confirm that:

- **This work was done wholly or mainly while in candidature for a research degree at this University.**
- **Where any part of this dissertation has previously been submitted for a degree or any other qualification at this University or any other institution, this has been clearly stated.**
- **Where I have consulted the published work of others, this is always clearly attributed.**
- **Where I have quoted from the work of others, the source is always given. With the exception of such quotations, this dissertation is entirely my own work.**
- **I have acknowledged all main sources of help.**
- **Where the dissertation is based on work done by myself jointly with others, I have made clear exactly what was done by others and what I have contributed myself.**



Pablo Daniel Tagle Salazar
Monterrey Nuevo León, December 26th, 2018

**@2018 by Pablo Daniel Tagle Salazar
All rights reserved**

Dedication

In memoriam of my father, Arnaldo, and in honor to my mother, Julia.
For my professors, the ones who has forged my identity.
For my friends, the people who was there, everyone who is here now, and the ones who will come.

Acknowledgements

The author acknowledges to all professors of Tecnológico de Monterrey who contributed with this research and the support of the Energy and Climate Change Research Group. I would like to acknowledge to CONACYT for support for living. I also would like to express my gratitude to the staff from Plataforma Solar de Almería for their support and collaboration during my research internship, in special to Loreto Valenzuela.

Thermo-hydraulic performance modeling of thermal energy systems using parabolic trough solar collectors

By

Pablo Daniel Tagle Salazar

Abstract

Solar energy is one of the most important emerging renewable energy resources. Parabolic trough solar collectors are one of the most used technologies for solar concentrating applications. The main purpose of this research is to develop a mathematical model for predicting thermodynamics and hydraulics of solar-to-heat conversion of thermal systems using parabolic trough collectors.

Thermal model is based on energy balance of a one-dimensional steady-state heat transfer thermal resistance circuit. The receiver and its surroundings are considered as the control volume of the analysis. Heat transfer coefficients are obtained using experimental correlations found in the literature. The model considers single-phase and two-phase flow with phase-change effects, where pressure drop is solved simultaneously with thermal energy balance. The input data corresponds to optics properties, design of collector, weather data, and basic hydraulic parameters (for series or parallel configurations). Parabolic trough collectors with Al_2O_3 /water nanofluid is also considered as a case of study.

Computational simulations are carried out using Engineering Equation Solver (EES), a software developed to solve complex systems of non-linear equations. This software was selected due to its simplicity in programming systems of non-linear equations and the available database of thermophysical properties of number of substances, including water and steam. Experimental data is used to validate the model, comparing with simulation results. Simulations are realized using same ambient and inlet operational conditions as described in test results. Sources of experimental data are test results of four collectors (for efficiency curves case), a M.Sc. Thesis previously presented (for nanofluid case), and from data provided by Plataforma Solar de Almeria (for direct steam generation case).

Results show a good agreement between simulations and experiments. Thermal parameters (such as thermal efficiency and temperatures) are predicted with high accuracy. There was obtained a global absolute error of around $1.5\text{ }^\circ\text{C}$ for temperatures and 2% in thermal efficiency. Comparison of temperature and pressure profiles using simulation results and experimental data of a direct steam generation system in once-trough mode show that the model can predict phase-change phenomena with high accuracy. Although, the model fails in predicting pressure drop with high steam quality two-phase flow.

List of Figures

Fig. 2.1 – Classification of solar energy technologies.....	18
Fig. 2.2 – Parabolic Trough Solar Collector.....	21
Fig. 2.3 – Geometrical errors in mirrors.....	22
Fig. 2.4 – PTC solar receiver.....	24
Fig. 2.5 – Operation of active trackers. a) closed-loop, b) open-loop.	29
Fig. 2.6 – Temperature range of some potential thermal applications for PTCs.....	30
Figure 2.7 - CSP plant diagrams a) Direct SG, b) Indirect SG integrated to a combined cycle.....	31
Fig. 2.8 – Absorption solar cooling systems. a) single effect, b) double effect	33
Fig. 2.9 – Adsorption solar cooling system.....	33
Fig. 2.10 – Evolution of solar cell technology. Borrowed from NREL website (www.nrel.gov/pv).....	37
Fig. 2.11 – Classification of thermal performance analysis.	38
Fig. 2.11 – Definition of acceptance angle	42
Fig. 2.12 – Geometry of a PTC	42
Fig. 2.13 – Description of end-effect losses	43
Fig. 2.14 – Thermal efficiency curve and components of heat losses	44
Fig. 3.1 - Boundary of the analysis of the collector.....	57
Fig. 3.2 - Thermal resistance model for the receiver	58
Fig. 3.3 - Energy balance around the fluid.....	59
Fig. 3.4 - Thermal resistance model for interconnecting piping	62
Fig. 3.5 - Energy balance around the interconnecting piping	62
Fig. 3.6 - Nu vs. Re for single-phase internal forced convection ($Pr=0.7$, $Pr/Pr_w=1$).	63
Fig. 3.7 - f vs. Re for single-phase flow	64
Fig. 3.8 - Typical flow pattern map for two-phase flow	67
Fig. 3.9 – Behavior of flow patterns.....	67
Fig. 3.10 - Flowchart algorithm.....	68
Fig. 3.11 – Thermo-hydraulic parameters vs. quality in two-phase phenomena	70
Fig. 3.12 – Temperature vs. entropy diagrams for phase change phenomena	72
Fig. 3.13 – Nu vs. Re for internal forced convection using Al_2O_3 /water nanofluid ($Pr/Pr_w=1$).....	74
Fig. 3.14 – Inputs for ambient conditions of collector system	77

Fig. 3.15 – Inputs for collector design used in thermal analysis	78
Fig. 3.16 – Inputs for system description section.	79
Fig. 3.17 – Defining variable limits	79
Fig. 3.18 – Warning message for convergence	80
Fig. 3.19 – Temperature, pressure and quality of steam profiles.	80
Fig. 4.1 – Efficiency curve for LS-2 with PTR-70 receiver	88
Fig. 4.2 – Comparison of output parameters for LS-2 with PTR-70 receiver	88
Fig. 4.3 – Absolute errors' boxplots of output parameters for LS-2 with PTR-70 receiver	89
Fig. 4.4 – Efficiency curve for LS-2 using UVAC receiver and Cermet coating	90
Fig. 4.5 – Efficiency curve for LS-2 using UVAC receiver and Black Chrome coating ..	90
Fig. 4.6 – Comparison of output parameters for LS-2 using UVAC receiver and Cermet coating.....	91
Fig. 4.7 – Comparison of output parameters for LS-2 using UVAC receiver and Black Chrome coating	91
Fig. 4.8 – Absolute errors' boxplots of output parameters for LS-2 with UVAC receiver and Cermet coating. a) Air in annulus, b) Vacuum in annulus.....	92
Fig. 4.9 – Absolute errors' boxplots of output parameters for LS-2 with UVAC receiver and Black Chrome coating. a) Air in annulus, b) Vacuum in annulus.	92
Fig. 4.10 – Efficiency curve for URSSA Trough PTC	94
Fig. 4.11 – Comparison of output parameters for URSSA Trough	95
Fig. 4.12 – Absolute errors' boxplots of output parameters for URSSA Trough	95
Figure 4.13 – Efficiency curve of CAPSOL PTC	96
Fig. 4.14 – Comparison of output parameters for CAPSOL	97
Fig. 4.15 – Absolute errors' boxplots of output parameters for CAPSOL	97
Fig 4.16 – Hydraulic diagram for experimental tests with nanofluids.....	98
Fig. 4.17 – Efficiency curve of experiments and simulations for the Al ₂ O ₃ -water nanofluid with 1% of volume concentration	100
Fig. 4.18 – Schematic diagram of DISS facility loop (PSA).	101
Fig. 4.19 – Operational conditions of the DISS plant at 2/April/2001	103
Fig. 4.20 - Operational conditions of the DISS plant at 13/May/2001	104
Fig. 4.21 – Operational conditions of the DISS plant at 15/May/2001	105
Fig. 4.22 – Comparison of simulated and experimental temperature / pressure profiles (2/Apr). a) 16h, b) 17h, c) 18h	107

Fig. 4.23 – Comparison of simulated and experimental temperature / pressure profiles (13/May). a) 13.45h, b) 14:30h, c) 15h	108
Fig. 4.24 – Comparison of simulated and experimental temperature / pressure profiles (15/May). a) 14h, b) 15h.....	109
Fig. 4.25 – Schematic diagram of solar field	110
Fig. 4.26 – Outlet pressure for a flow rate of 9 GPM, inlet pressure of 25 barg, and ambient temperature of 18 °C.	111
Fig. 4.27 – Selection of operational region of solar field.....	111
Fig. 4.28 – Level curves for mass flow, thermal power, and over-heating temperature difference.	113
Fig. A.1 – Inlet data in system description section for different types of analysis. a) Single-phase flow without nanofluids, b) Single-phase flow using nanofluids, c) Two-phase flow	119
Fig. A.2 – Solution window	120
Fig. A.3 – Arrays table.....	120
Figure A.4 – Fixing limits for manual phase-change prediction	121
Figure A.5 – Error message for manual phase-change prediction	122
Fig. B.1 – Windows for parametrization. a) selecting the variable, b) deactivating the variable, c) Variable deactivated.	123
Fig. B.2 – Defining new parametric table.....	124
Fig. B.3 – New parametric table. a) Table, b) defining values of parametric variables	124

List of Tables

Table 1.1 – Software tools used for analysis with PTCs [8-14]	4
Table 1.2 – Studies and models of thermal analysis of PTCs.	6
Table 2.1 - Comparison of solar concentrating technologies.....	19
Table 2.2 – Advantages and Disadvantages of PTC technology	21
Table 2.3 - Types of mirrors and their properties	23
Table 2.4 - Characteristics of some receivers available in market	26
Table 2.5 - Heat transfer fluids used on PTC fields	27
Table 2.6 – Characteristics of concentrating photovoltaic applications	36
Table 2.7 - Experimental studies of collectors.....	39
Table 2.8 – Correlations for incidence angle and slope angle of surface for PTC.....	43
Table 2.9 – Reliability and performance tests included in each standard.....	45
Table 3.1 – Heat transfer modes in thermal resistance model	59
Table 3.2 - Constants for (3.47)	66
Table 3.3 - Equations for pressure drop modeling	69
Table 3.4 – Mathematical model for other heat transfer phenomena	75
Table 3.5 - Constants for Zhukauskas correlation.....	76
Table 4.1 – Resume of geometrical parameters of simulated collectors	87
Table 4.2 – Descriptive statistics for absolute errors (LS-2 + PTR-70).....	89
Table 4.3 – Descriptive statistics for absolute errors (LS-2 + UVAC and Cermet)	92
Table 4.4 – Descriptive statistics for absolute errors (LS-2 + UVAC and Black Chrome)	93
Table 4.5 – Descriptive statistics for absolute errors (URSSA Trough)	94
Table 4.5 – Descriptive statistics for absolute errors (CAPSOL)	97
Table 4.6 – Characteristics of PT-110	98
Table 4.7 – Experimental and simulation data comparison for the Al ₂ O ₃ -water nanofluid with 1% of volume concentration.....	99
Table 4.8 – Coefficients thermal efficiency curve for the Al ₂ O ₃ -water nanofluid with 1% of volume concentration	99
Table 4.9 – Descriptive statistics for absolute errors (PT-110 with nanofluid as HTF)	100
Table 4.10 – Characteristics of LS-3 collector.....	102
Table 4.11 – Steady-state temporal intervals	102
Table 4.12 – Resume of operational conditions for simulations	106

Table 4.13 – Error in inlet temperature between experiments and simulations (°C)....	106
Table 4.14 – Error in pressure drop between experiments and simulations (barg)	106
Table 4.15 – Statistics of absolute errors	109
Table 4.16 – Characteristics of PT250 collector.....	110
Table 4.17 – Variation of outlet conditions.	112

Contents

Abstract.....	v
List of Figures.....	vi
List of Tables.....	ix
Chapter 1 Problem statement.....	1
1.1 Background	1
1.1.1 Software available in market	2
1.1.2 Thermal models in the literature	3
1.2 Problem statement.....	12
1.3 Objectives.....	12
1.4 Scope	13
1.5 General Assumptions	13
1.6 Expected results	13
1.7 Nomenclature	14
1.7.1 Acronyms	14
1.8 References	14
Chapter 2 Introduction to Parabolic Trough Technology	18
2.1 A brief description of the Parabolic-Trough collector technology	18
2.1.1 Background	18
2.1.2 Components.....	21
2.1.2.1 Mirrors.....	22
2.1.2.2 Supporting structure.....	24
2.1.2.3 Receiver.....	24
2.1.2.4 Heat transfer Fluid	25
2.1.2.5 Solar tracking system.....	25
2.2 Industrial applications	30
2.2.1 Heating.....	30
2.2.2 Cooling	32
2.2.3 Seawater desalination	34
2.2.4 Water decontamination	35
2.2.5 Concentrating photovoltaics	35

2.3	Performance analysis methods.....	36
2.3.1	Thermal performance	36
2.3.2	Optical performance	41
2.4	Basic concepts on performance of Parabolic-Trough collectors	41
2.4.1	Geometric factors	41
2.4.2	Thermal efficiency curve.....	43
2.5	Nomenclature	47
2.5.1	Acronyms	47
2.5.2	Symbols.....	47
2.5.3	Greek letters.....	48
2.6	References	48
Chapter 3	Description of modeling	57
	Abstract	57
3.1	Thermo-hydraulic model	57
3.1.1	Energy Balance Equations for Receiver	58
3.1.2	Energy Balance Equations for Interconnecting Piping.....	61
3.1.3	Single-phase Internal Forced Convection.....	62
3.1.4	Two-phase Internal Forced Convection.....	64
3.1.5	Modeling phase change phenomena	71
3.1.6	Internal forced convection using Al ₂ O ₃ /water nanofluids	73
3.1.7	Other Heat Transfer Phenomena	74
3.1.7.1	Natural annular convection	74
3.1.7.2	Natural external convection.....	74
3.1.7.3	Cross-flow external forced convection	76
3.1.7.4	External convection in extended surfaces.....	76
3.1.7.5	Radiation in Annular region.....	76
3.1.7.6	External radiation	76
3.2	A brief description of thermal analysis using Engineering Equation Solver	77
3.2.1	Background	77
3.2.2	Input data window	77
3.2.3	Convergence	79
3.2.4	Output data window.....	80
3.3	Nomenclature	80

3.4 References	84
Chapter 4 Results and discussion	86
4.1 Case 1: Thermal efficiency curves.....	86
4.1.1 LS-2 with a PTR-70 receiver	86
4.1.2 LS-2 with an UVAC receiver.....	89
4.1.3 URSSA Trough.....	93
4.1.4 CAPSOL.....	95
4.2 Case 2: Parabolic trough using nanofluids	97
4.3 Case 3: Direct steam generation	101
4.4 Case 4: Estimation of thermal power for steam generation in a dairy plant	110
4.5 Nomenclature	113
4.6 References	114
Chapter 5 Conclusions	116
Conclusions	116
Recommendations.....	117
Future work.....	117
Appendix A General user manual of windows in Engineering Equation Solver	119
A.1 Input data window.....	119
A.2 Solution in Single-phase flow.....	120
A.3 Solution in two-phase flow	121
Appendix B Parametric analysis in Engineering Equation Solver	123
Published papers	125
Curriculum Vitae.....	129

Chapter 1 Problem statement

The main idea of this chapter is to establish the general scene of the research. Scope, objectives, and expected results are presented. There is given a brief description of background of previous research and computational tools used to simulate solar conversion systems. The organization of this thesis is also described below.

1.1 Background

The penetration of renewable technologies in the international power generation market has increased in recent years all around the world. The principal reason is the growing interest of governments in implementing renewable energy generation systems to mitigate greenhouse gas (GHG) emissions and provide better energy security. At the end of 2015, around 150 countries implemented energy improvement policies, and at least 128 established energy efficiency strategies and targets [1]. One of the most important applications for Parabolic Trough Collector (PTC) technology is electricity generation. The installed capacity of power plants with PTC technology has increased in the last decade, with the United States and Spain being the principal contributors in solar thermal power generation. Most of the electricity generation systems using solar thermal resources are PTC-based, accounting for approximately 85% of total current installed capacity worldwide [2].

In 2014, the demand of thermal energy in industry was around 85.3EJ, equivalent to 74% of industrial energy needs [3]. Near 52% of this demand is applied into low-to-medium temperature heating applications, which shows a high potential of Solar Heating Industrial Processes (SHIPs) for industrial thermal energy supply. PTCs are one of the technologies used in SHIPs that have recently been developed and implemented in small-to-medium scale plants around the world. Small-aperture collectors are the most used PTCs in these applications, which can reach temperatures up to 250°C [4]. Nowadays, the technology applied to SHIPs is still under development. Although, a number of installations and collectors with substantial technical improvements have been reported around the world with good experience in performance and economics during the last years [5].

The principal advantages of this technology are their reduced risk (compared with volatility of fossil fuel prices), zero fuel cost, localized production, and low GHG emission. Nevertheless, it still needs to overcome the barriers of the investment cost and complexity of the systems in order to have a good penetration into industry. Other barriers are the lack of technical information transfer, suitable design guidelines, and analysis tools [6]. For small-aperture PTCs, the technology still needs to prove a strong suitability in industry, taking their advantages and experiences in SHIPs and other small-to-medium scale applications. However, the actual tendency shows an increment in interest, investment, and developing of this technology [6]; principally for industrial thermal energy supply. International Energy Agency (IEA) considers that there is potential market and technological development due to around 28% of the overall demand of thermal energy in European Union countries are heat processes with temperatures below 250°C [7].

Software tools are useful in engineering for designing systems. They simulate the system using mathematical models and formulae to determine its behavior. This makes possible to “test” the system under a variety of conditions without making costly and/or complex experimentation, which leads to a decrement of costs and time in design process. Mathematical formulae depend on the phenomena involved into the process, and its accuracy on the phenomena and quality of equations included in the model. For the case of solar-to-heat energy conversion with concentrating technologies; Heat transfer, fluid mechanics, and optics are the basic phenomena to be considered.

There are many parameters in solar energy applications that are essential but not easy to obtain numerically, being thermal efficiency one of the most important. There are also models in the literature and software that can analyze thermal systems with solar collectors. Thermal models found in the literature are limited due to the quality of formulae used, limitations, and assumptions to simulate the thermal system.

1.1.1 Software available in market

There is few software available in the market to make evaluation of solar collectors. The approaches used in software depend on applicability and desired parameters to be determined. Some of them can realize techno-economic analysis, or optics. The characteristics of some software available to simulate solar thermal systems, and mathematical models found in the literature are described below. Table 1.1 shows the principal characteristics of the software described.

- **ASAP:** This is a software specialized on optical analysis using ray-tracing. It can simulate optical effects such as refraction, diffraction, reflection, and polarization. It is focus on illumination systems, but it can also be applied to determine optical performance of collectors.
- **CFD software packages:** A Computational Fluid Dynamics (CFD) software solves governing equations of heat transfer and fluid mechanics in a numerical way to obtain temperature and velocity fields in the fluid. Thermal parameters can be obtained based on those fields. Methods used are Finite Volume Method (FVM) and Finite Element Method (FEM). This kind of software are capable to simulate also complex phenomena such as chemical reactions, mass transfer, transient-state, and others. The most common software in industry are FLUENT (which uses FVM) and COMSOL (which uses FEM).
- **SAM:** System Model Advisor (SAM) is a software for thermo-economic modeling of on-grid power generation systems. Simulations are carried out by adding subroutines according to the components used in power system, including PTCs. SAM uses a random-generating data for renewable resources to evaluate the system and estimate converted energy and economics. It also uses parametric optimization (comparing many systems at the same time) and sensitivity analysis. It only simulates power systems which uses fluids in single-phase flow (thermal oils as they are the most commons heat transfer fluid used in those applications).

- **SolTrace:** This software is used to determine optical performance of solar collectors using ray-tracing. It can simulate single, multi-planar or curved reflective surfaces. This software is specifically developed for solar energy applications.
- **Thermoflex:** Thermoflex is a software designed to estimate thermo-economic analysis of complex off-grid power generation systems for decision making, principally used for non-renewable technologies. This software uses libraries to simulate different components, where one of them are thermal systems with PTCs.
- **TRNSYS:** TRAnSient SYstem Simulation is a software that realize dynamic system analysis. It is capable to simulate not only thermo-electric systems, but also industrial, traffic, biological, and other dynamic processes. Similar to Thermoflex, it uses libraries for components of the system and resources. One of these libraries is exclusive to simulate solar collectors using its characteristic curve. There are other library that links Engineering Equation Solver (EES) or Fortran codes

1.1.2 Thermal models in the literature

There are many studies in the literature related with performance analysis of solar collectors. Table 1.2 describes the type of analysis done and a brief explanation of the method used of some studies found in the literature about thermal systems with PTCs. Macroscopic analysis refers to the use of experimental correlations to calculate heat transfer coefficients, while microscopic analysis refers to numerical solution of governing equations. There are some models that considers multi-dimensional heat transfer. Some of the studies show validation of the model comparing results with experimental data. There are many approaches to analyze thermal systems with solar collectors such as thermo-economics, exergetic performance, comparison of methodologies to determine performance, experimental analysis of optics and heat losses, and others. This demonstrates the applicability of solar collectors in industry, and the impact of research for improving methodologies used to determine performance of solar thermal systems.

Based on studies presented, the most used type of modeling is one-dimensional steady-state for thermal performance of collectors. A few models presented considers pressure drop in performance analysis. Some models analyzed solar fields, but they do not specify its hydraulic design (series, parallel, or combined). Thermal performance analysis with thermal resistance modeling and thermal parameter characterization (performance curve) are the most frequently used methods in energy balance using a macroscopic approach. However, for a microscopic approach, CFD modeling is the most common methodology used. Many studies in the literature use these methodologies with experimental validation of mathematical modeling, as shown in Table 1.2.

Table 1.1 – Software tools used for analysis with PTCs [8-14]

Name	Developer	Analysis	Method	Strengths / Weaknesses
Advanced System Analysis Program (ASAP)	Breault Research Organization Inc.	Optical performance	Ray Tracing by Gaussian beam decomposition	<ul style="list-style-type: none"> - Gaussian-beam decomposition treats the light as a wave rather than as a particle (as usual Monte Carlo methods). - Compatible with CAD programs to simulate complex shapes. - Not free software.
Fluent	ANSYS Inc.	Thermo / hydro dynamics	CFD by FVM	<ul style="list-style-type: none"> - Compatible with CAD programs. - Use an external software to configured the mesh-grid, materials and boundary conditions. - Not free software. - It needs a re-configuration (from the beginning) of all the analysis if the design changes.
Comsol	Comsol Inc.	Thermo / hydro dynamics	CFD by FEM	<ul style="list-style-type: none"> - Compatible with CAD programs. - Meshing component is integrated to the software - Quick convergence with Multiphysics phenomena. - Not free software. - It needs a re-configuration (from the beginning) of all the analysis if the design changes.
Solar Advisor Model (SAM)	NREL	Thermo-economics	Energy balance and cashflows	<ul style="list-style-type: none"> - For not only renewable energy-based systems, but also conventional fossil-fueled power systems. - It can simulate various configurations at the same time. - Free software. - Limited design with pre-coded or characterized collector models.

Table 1.1 – Continuation

Name	Developer	Analysis	Method	Strengths / Weaknesses
SolTrace	NREL	Optical performance	Ray tracing by Monte Carlo method	<ul style="list-style-type: none">- Exclusive for concentrating solar technology.- Definition of surfaces by coordinates.- Free software.
Thermoflex	Thermoflow Inc.	Thermo-economics	Energy balance and cashflows	<ul style="list-style-type: none">- Software specialized in conventional power plant design.- It can analyze one system at a time.- Not free software
Transient System Simulation (TRNSYS)	University of Wisconsin	Thermal analysis	Energy balance	<ul style="list-style-type: none">- It simulates transient behavior of systems.- Compatible with Engineering Equation Solver.- Not free software.- Limited design with pre-coded or characterized collector models.

Table 1.2 – Studies and models of thermal analysis of PTCs.

Authors	Year	Ref.	Analysis		State		Dimensions			Experiments		Description
			Macroscopic	Microscopic	Steady	Transient	1D	2D	3D	Indoor	Outdoor	
Kalogirou et. al	1997	[15]	x			x	x				√	Thermal analysis and parametric optimization model for a PTC system with energy storage for direct steam generation. Thermal performance parameters of the collector are required.
Forristal	2003	[16]	x		x		x	*			√	Thermal resistance model with energy balance around the receiver. The author reported 4 models, one of them analyzes a series PTC system with pressure drop.
Lüpfert et. al	2008	[17]									x	Experimental comparison of three methodologies (steady state, quasi-dynamic and surface temperature measurement) to obtain heat losses in a receiver.
García-Valladares y Velázquez	2009	[18]	x			x	x				√	Discretized thermal model to compare radial heat transfer in tubular and annular flow in the receiver. Annular flow is analyzed as a counter flow heat exchanger.

Table 1.2 – Continuation

Authors	Year	Ref.	Analysis		State		Dimensions			Experiments		Description
			Macroscopic	Microscopic	Steady	Transient	1D	2D	3D	Indoor	Outdoor	
Schiricke et al.	2009	[19]									x	Experimental study of optical efficiency of a PTC using photogrammetry and heat flux measurement. Ray tracing simulation is used to compare the results.
Montes et al.	2010	[20]	x		x		x		*			Numerical study based on energy and exergy balance of a CSP plant to compare thermal performance with 4 HTFs. The thermal model used is a thermal resistance circuit, but the study does not specify the conditions and details of this model.
Qu et. al.	2010	[21]	x			x	x				?	Thermal analysis of a heating / absorption cooling system for a building. The thermal model is based on thermal parameters of the collector. Simulations are realized using TRNSYS.
Montes et. al.	2011	[22]	?			?	x					Thermo-economic analysis of a combined cycle power plant using a PTC system to heat the steam, compared with a non-solar-assisted power plant.

Table 1.2 – Continuation

Authors	Year	Ref.	Analysis		State		Dimensions			Experiments		Description	
			Macroscopic	Microscopic	Steady	Transient	1D	2D	3D	Indoor	Outdoor		
Powell y Edgard	2011	[23]		x		x	x					Thermal analysis model based on energy balance for a PTC receiver and thermal storage of a steam generation plant. The mathematical model is based on numerical resolution of governing equations using finite difference method.	
Roesle et al.	2011	[24]		x	x			x			?	Thermal analysis of a evacuated receiver with non-uniform angular radiation flux using CFD simulations.	
Vázquez-Padilla et al.	2011	[25]	x			x					√	Thermal analysis using thermal resistance energy balance model with pressure drop. Comparison with experimental data and Forristal's thermal model.	
Kalogirou	2012	[26]	x			x					√	Thermal resistance model with energy balance around a glass covered receiver. This model is similar to the Forristal's model, but it does not consider heat losses by brackets.	
Roldán et al.	2012	[27]		x		x					x	√	CFD simulation of a receiver used in direct steam generation plant. Superheated steam is the HTF. Surface temperature measurements are used as experimental validation.

Table 1.2 – Continuation

Authors	Year	Ref.	Analysis		State		Dimensions			Experiments		Description	
			Macroscopic	Microscopic	Steady	Transient	1D	2D	3D	Indoor	Outdoor		
Zaversky et al.	2012	[28]										Probabilistic thermal model to obtain useful energy of a PTC system using Latin hypercube method.	
Lobón et al.	2013	[29]		x		x				x	√	Thermal analysis of a PTC system for direct steam generation. Different conditions of pressure, temperature, incident radiation and mass flow are analyzed. The method used is CFD simulation using k-ε turbulence model.	
Silva et al.	2013	[30]	x				x			x	√	Thermo-hydraulic analysis with 3-D non-linear heat transfer model in transient state for a steam generation PTC system. Simulations are realized in SolTrace, TRNSYS and Modelica (a code developed by the authors) simultaneously. Comparison with experimental data is presented in the study.	
Valenzuela et al.	2014	[31]										x	Experimental methodology to obtain the thermo-optical performance of a PTC with outdoor tests.

Table 1.2 – Continuation

Authors	Year	Ref.	Analysis		State		Dimensions			Experiments		Description	
			Macroscopic	Microscopic	Steady	Transient	1D	2D	3D	Indoor	Outdoor		
Xu et al.	2014	[32]									x	Comparison of three experimental methods (ASHRAE 93, EN 12975-2 and a dynamic-method presented by the authors) to determine thermal performance.	
Biencinto et al.	2015	[33]	x			x		x				x	Thermal performance analysis of a PTC system for direct steam generation. A Quasi-dynamic method is used. It is based on finite-difference method in temporal dimension and thermal performance parameter of the collector.
Bellos et al.	2016	[34]		x		?						x	Comparative study in thermal enhancement of a PTC using nano-fluids (oil based) and conventional fluids (oil and pressurized water). Inner surface configurations (smooth and corrugated) in the pipe receiver are also compared.
Toghyani et al.	2016	[35]	x			x			x				Thermodynamic analysis of a PTC system integrated to a Rankine cycle power plant. Thermal performance of oil based nanofluid with 4 different nano-particles are compared.

Table 1.2 – Continuation

Authors	Year	Ref.	Analysis		State		Dimensions			Experiments		Description	
			Macroscopic	Microscopic	Steady	Transient	1D	2D	3D	Indoor	Outdoor		
Widyolar et al.	2016	[36]		x	x						?	?	Design, simulating and test of a two-stage reflective hybrid thermal/photovoltaic PTC. Finite element analysis is used for thermal analysis, ray tracing for optical performance, and efficiency parameter for electric performance.
Srivastara and Reddy	2017	[37]		x	x							x	Numerical study of hybrid thermal / photovoltaic PTC and secondary reflector. Various configurations for solar cells are analyzed. Nanofluid is used for cooling the solar cells. ASAP is used for optical performance, and finite volume method for thermal analysis.

√ Validated with experiments.

* Hydrodynamics with pressure drop.

? Not specified.

1.2 Problem statement

There was shown software available to evaluate performance of thermal systems with PTCs. CFD software have the potential of be very precise in results, but they are focus on design of a specific parabolic trough rather than global analysis of a system (which is the main purpose of this study). Other software considers economic analysis, but they are exclusive for evaluation of concentrating solar power plants, mostly with thermal oil as heat transfer fluid. There was not found a software that can analyze direct steam generation systems, but there are studies about performance of this kind of plants using CFD analysis [27,29,30].

Most common thermal models are focus on thermal performance analysis using heat transfer and fluid mechanics separately, which is possible to consider when heat transfer fluid flows in single-phase conditions. A few models consider two-phase flow phenomena. Recent studies are focus on performance evaluation using other-than-common fluids, such as molten salts or nanofluids. The main idea of this research is to design a thermal model that combines heat transfer and fluid mechanics into one thermal energy-balance modeling, so two-phase or phase-change phenomena can be considered into performance analysis (i.e. direct steam generation systems).

1.3 Objectives

Principal objective

To develop a mathematical model for performance evaluation of solar thermal systems with parabolic trough collectors able to predict thermo-hydraulic behavior of the whole system and each collector section using computational simulations based on a discrete one-dimensional steady-state heat transfer and pressure drop model.

Secondary objectives

1. To develop a computational code able to simulate heat transfer and hydraulic phenomena involved in solar-to-heat energy conversion using parabolic trough collectors.
2. The model should be able to simulate the solar field under a variety of ambient and operational conditions. It should also allow change design parameters (such as thermophysical properties, optical properties, dimensions) of the collector used in solar field.
3. The code should be adaptable to change or update mathematical formulae of heat transfer, fluid mechanics, and/or thermophysical properties of substances.
4. To validate the model comparing simulation results with experimental data.
5. The model should be able to simulate single-phase and two-phase phenomena in order to cover applications where phase-change occurs (such as steam generation).

1.4 Scope

The model presented in this work should include the effects of heat transfer and fluid mechanics in the receiver and its surroundings as the boundary of the analysis. Heat transfer under steady-state is a must of the model and experimental data (to compare for validation). The model can predict thermo-hydraulic behavior, using design parameters, operational conditions, and measured or estimated ambient parameters as inputs. Optics (such as incident angle modifier) are inputs of the model. Thermophysical properties of substances can be entered as datum, table data, equation (temperature dependent as preferable), or using the database of the software.

As a thermal system, the boundary of the analysis presented in this work is only the solar field. Thermal storage and other types of energy conversion are not included in this analysis. Simulation of direct steam generation systems are included in the scope of this model. Only once-trough operational mode of this kind of plants is included in the thermal model. Two-phase flow phenomena are exclusive for water as transfer fluid.

1.5 General Assumptions

- Steady-state was selected for simplicity of the model.
- Temperature gradients are higher in radial direction (above 100 °C/m) compared to heat transfer in axial direction (lower than 10 °C/m), which justify one-dimensional heat transfer.
- Angular direction is not considered due to the assumption of constant heat flux at the surface of the receiver.
- All thermophysical properties of substances are considered isotropic (independent of direction of heat transfer) and they may be dependent of temperature.
- Single-phase flow of the fluids is considered fully developed, and with constant velocity profile at inlet and outlet.
- Two-phase flow is considered with constant profile of velocity for each phase.
- Gasses (in the annulus, and outside the receiver) are considered as non-participative media in radiation.
- Incident radiation at the receiver considers only reflected radiation from mirrors.

1.6 Expected results

Thermal model is developed using EES as software of analysis. Thermal simulations are carried out using single-phase and two-phase flow. Phase-change simulations are realized using water as heat transfer fluid only. Validation of the model is done by comparing results from simulations and experiments. There is expected that simulations results show good agreement with experimental data (same order of magnitude), proving that it predicts thermo-hydraulic performance with high accuracy. Parameters to be compared are measured variables such as thermal efficiency, temperatures and pressures. It is also expected to obtain mathematical correlations between thermo-hydraulic parameters and input ambient/operational conditions using results from

simulations. These correlations may be used for determining better operation, system's design, or for sensitivity analysis of a given thermal system.

1.7 Nomenclature

1.7.1 Acronyms

CFD	Computational Fluid Dynamics
EES	Engineering Equation Solver
FEM	Finite Element Method
FVM	Finite Volume Method
GHG	Greenhouse Gas
IEA	International Energy Agency
SAM	System Model Advisor
PTC	Parabolic Trough Collector
SHIP	Solar Heat Industrial Process

1.8 References

- [1] REN21. Renewables 2016: Global status report. Paris: REN21 Secretariat; 2016. 272p
- [2] International Renewable Energy Agency. Renewable power generation costs in 2014. IRENA Publications; 2015. 54 p.
- [3] SANEDI. Solar heat for industry [pdf on internet]. [cited 2018 Mar 06]. Available from: https://www.sanedi.org.za/img/Brochure%20Solar%20PayBack_4.pdf.
- [4] IEA. Process Heat Collectors: State of the Art and available medium temperature collectors [pdf on internet]. 2015 [cited 2018 Mar 07]. Available from: http://task49.iea-shc.org/data/sites/1/publications/Task%2049%20Deliverable%20A1.3_20160504.pdf.
- [5] Hess S. Solar thermal process heat (SPH) generation. In: Stryi-Hipp G, editor. Renewable heating and cooling: Technologies and applications. 2016. p. 41-66.
- [6] IRENA, ETSAP. Solar heat for industrial processes: Technology brief. 2015.
- [7] Philipps S, Bett A, Horowitz K, Kurtz S. Current status of concentrator photovoltaic (CPV) technology. Golden (CO, USA): NREL; 2016. 26 p. Report No.: NREL/TP-6A20-63916.
- [8] Ho C. Software and codes for analysis of concentrating solar power technologies. Albuquerque (NM, USA): SANDIA; 2008. 35p. Report No.: SAND2008-8053.
- [9] Breault Reserach Organization Inc. ASAP Capabilities [internet]. Tucson, AZ (USA): BRO; [cited 2017 Jun 27]. Available from: <http://www.breault.com/software/asap-capabilities>.

- [10] ANSYS. Fluent [internet]. ANSYS [cited 2017 Jun 27]. Available from: <http://www.ansys.com/Products/Fluids/ANSYS-Fluent>.
- [11] COMSOL Inc. CFD Module [internet]. Burlington, MA (USA): COMSOL Inc; [cited 2017 Jun 27]. Available from: <https://www.comsol.com/cfd-module>.
- [12] National Renewable Energy Laboratory. System Advisor Model (SAM) [internet]. Golden, CO (USA): NREL; [cited 2017 Jun 27]. Available from: <https://sam.nrel.gov/>.
- [13] Thermoflow Inc. Thermoflex & Peace: Solar thermal modelling [internet]. Southborough, MA (USA): Thermoflow Inc; [cited 2017 Jun 27]. Available from: https://www.thermoflow.com/solarthermal_overview.html.
- [14] Thermal Energy Systems Specialist LLC. TRNSYS [internet]. Madison, WI (USA): TESS; [cited 2017 Jun 27]. Available from: <http://www.trnsys.com/#1>.
- [15] Kalogirou S, Lloyd S, Ward J. Modelling, optimisation and performance evaluation of a parabolic trough solar collector steam generation system. *Sol Energy*. 1997;60(1):49–59.
- [16] Forristall R. Heat transfer analysis and modelling of a parabolic trough solar receiver implemented in Engineering Equation Solver. Golden (CO): NREL; 2003. 164p. Report No.: NREL/TP-550-34269.
- [17] Lüpfert E, Riffelmann K-J, Price H, Burkholder F, Moss T. Experimental Analysis of Overall Thermal Properties of Parabolic Trough Receivers. *J Sol Energy Eng*. 2008;130(2):021007.
- [18] García-Valladares O, Velázquez N. Numerical simulation of parabolic trough solar collector: Improvement using counter flow concentric circular heat exchangers. *Int J Heat Mass Transf*. 2009;52(3-4):597–609.
- [19] Schirricke B, Pitz-Paal R, Lüpfert E, et al. Experimental verification of optical modeling of parabolic trough collectors by flux measurement. *J. Sol. Energy Eng*. 2009;131(1):011004-011004-6.
- [20] Montes M, Abánades A., Martínez-Val J. Thermofluidynamic model and comparative analysis of parabolic trough collectors using oil, water/steam, or molten salt as heat transfer fluids. *J Sol Energy Eng*. 2010;132(2):021001.
- [21] Qu M, Yin H, Archer D. A solar thermal cooling and heating system for a building: Experimental and model based performance analysis and design. *Sol Energy*. 2010;84(2):166–82.

- [22] Montes M, Rovira A, Muñoz M, Martínez-Val J. Performance analysis of an Integrated Solar Combined Cycle using Direct Steam Generation in parabolic trough collectors. *Appl Energy*. 2011;88(9):3228–38.
- [23] Powell KM, Edgar TF. Modeling and control of a solar thermal power plant with thermal energy storage. *Chem Eng Sci*. 2012;71:138–45.
- [24] Roesle M, Coskun V, Steinfeld A. Numerical analysis of heat loss from a parabolic trough absorber tube with active vacuum system. ASME 2011 5th International Conference on Energy Sustainability, Parts A, B, and C. 2011.
- [25] Vasquez-Padilla R, Demirkaya G, Goswami D, Stefanakos E, Rahman M. Heat transfer analysis of parabolic trough solar receiver. *Appl Energy*. 2011;88(12):5097-5110
- [26] Kalogirou SA. A detailed thermal model of a parabolic trough collector receiver. *Energy*. 2012;48(1):298–306.
- [27] Roldán M, Valenzuela L, Zarza E. Thermal analysis of solar receiver pipes with superheated steam. *Appl Energy*. 2013;103:73–84.
- [28] Zaversky F, García-Barberena J, Sánchez M, Astrain D. Probabilistic modeling of a parabolic trough collector power plant – An uncertainty and sensitivity analysis. *Sol Energy*. 2012;86(7):2128–39.
- [29] Lobón DH, Baglietto E, Valenzuela L, Zarza E. Modeling direct steam generation in solar collectors with multiphase CFD. *Appl Energy*. 2014;113:1338–48.
- [30] Silva R, Pérez M, Fernández-García A. Modeling and co-simulation of a parabolic trough solar plant for industrial process heat. *Appl Energy*. 2013;106:287–300.
- [31] Valenzuela L, López-Martín R, Zarza E. Optical and thermal performance of large-size parabolic-trough solar collectors from outdoor experiments: A test method and a case study. *Energ*. 2014;70:456–64.
- [32] Xu L, Wang Z, Li X, Yuan G, Sun F, Lei D, et al. A comparison of three test methods for determining the thermal performance of parabolic trough solar collectors. *Sol Energy*. 2014;99:11–27.
- [33] Biencinto M, González L, Valenzuela L. A quasi-dynamic simulation model for direct steam generation in parabolic troughs using TRNSYS. *Appl Energy*. 2016;161:133–42.
- [34] Bellos E, Tzivanidis C, Antonopoulos K, Gkinis G. Thermal enhancement of solar parabolic trough collectors by using nanofluids and converging-diverging absorber tube. *Renew Energy*. 2016;94:213–22.

[35] Toghyani S, Baniasadi E, Afshari E. Thermodynamic analysis and optimization of an integrated Rankine power cycle and nano-fluid based parabolic trough solar collector. *Energy Conversion and Management*. 2016;121:93–104.

[36] Widyolar BK, Abdelhamid M, Jiang L, Winston R, Yablonovitch E, Scranton G, et al. Design, simulation and experimental characterization of a novel parabolic trough hybrid solar photovoltaic/thermal (PV/T) collector. *Renew Energy*. 2017;101:1379–89.

[37] Srivastava S, Reddy K. Simulation studies of thermal and electrical performance of solar linear parabolic trough concentrating photovoltaic system. *Sol Energy*. 2017;149:195–213.

Chapter 2 Introduction to Parabolic Trough Technology

This chapter is a brief explanation about the technology used in this study. Basic information about components, functionality, applicability, and methods used for thermal evaluation are presented. Industrial applications (such as heating, cooling, or concentrating photovoltaics), processes of solar energy conversion, and advances in these areas are also presented. A general description of performance evaluation of parabolic collectors is also presented, with focus on thermal behavior evaluation.

2.1 A brief description of the Parabolic-Trough collector technology

2.1.1 Background

Many technologies have been developed around the world to meet energy demands using renewable and non-renewable resources. Solar energy is one of the most important emerging renewable energy resources. Solar technologies can be classified as shown in Figure 2.1. Active solar systems differ from passive since they use external components to convert solar energy (e.g. pumps, tracking, electronic controls, etc.). Concentrated solar technologies are considered as active because they need external components, which are generally related to fluid transport or solar tracking, to realize energy conversion. All concentrating technologies use the same principle to convert solar energy. They reflect or refract solar radiation from a large area (collection) to a smaller area (receiver) using mirrors or lenses, so the heat flux at the receiver area is intensified. The intensity of radiation can be measured by the concentration factor, which is a dimensionless ratio between the collection area and the receiver area.

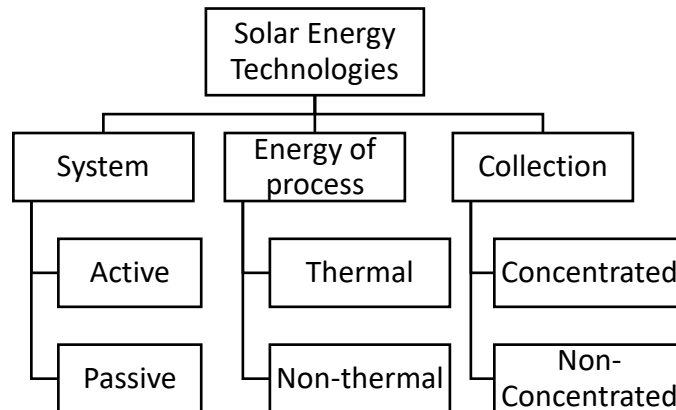


Fig. 2.1 – Classification of solar energy technologies

There are four main solar concentrating technologies: Parabolic Trough (PTC), Solar Tower (ST), Linear Fresnel (LFC), and Parabolic Dish (PD). There are two characteristics that differ from one to another technology: type of focus (where the sunlight is concentrated, linear or point) and type of receiver (mobile or stationary). Linear-focus use one-axis tracking, while point-focus use two-axis tracking. Receivers and reflectors/refractors follows the sun in mobile-receivers, while only reflectors/refractors

track the sun in stationary-receivers. Parabolic Trough collectors are linear-focus mobile-receiver, Solar Tower are point-focus stationary-receiver, Linear Fresnel are linear-focus stationary-receiver, and finally Parabolic Dish are point-focus mobile-receiver. Table 2.1 shows the most characteristic differences among all these technologies.

Table 2.1 - Comparison of solar concentrating technologies [1,2]





				
	Parabolic Trough	Solar Tower	Linear Fresnel	Parabolic Dish
Typical capacity (MW)	10 - 300	10 – 200	10 - 200	0.01 – 0,025
Maturity	Commercially proven	Commercially proven	Recent commercial project	Demonstration projects
Technology development risk	Low	Medium	Medium	Medium
Operating temperature (°C)	350 - 400	250 – 565	250 - 350	550 – 750
Plant peak efficiency (%)	14 - 20	23 – 35*	18	30
Annual solar-to-electricity efficiency (%)	11 – 16	7 – 20	13	12 – 25
Annual capacity factor (%)	25 – 28 (no TES) 29 – 43 (7h TES)	55 (10h TES)	22 - 24	25 – 28
Concentration factor	10 – 80	> 1000	> 60	Up to 10 000
Receiver absorber	/ Absorber attached to collector, moves with collector, complex design	External surface or receiver, fixed	Fixed absorber, no evacuation secondary reflector	Absorber attached to collector, moves with collector

Table 2.1 – Continuation

	Parabolic Trough	Solar Tower	Linear Fresnel	Parabolic Dish
Storage system	Indirect two-tank molten salt at 380°C ($\Delta T=100K$)	Direct two-tank molten salt at 550°C ($\Delta T=300K$)	Short-term pressurized steam storage (<10 min)	No storage for Stirling dish, chemical storage under development.
Hybridisation	Yes and direct	Yes	Yes, direct (steam boiler)	Not planned
Grid stability	Medium to high (TES or hybridisation)	High (large TES)	Medium (back-up firing possible)	Low
Cycle	Superheated Rankine steam cycle	Superheated Rankine steam cycle	Saturated Rankine steam cycle	Stirling
Steam conditions (°C / bar)	380 – 540 / 100	540 / 100 – 160	260 / 50	n.a.
Maximum slope of solar field (%)	< 1 - 2	< 2 – 4	<4	10 or more
Water requirement (m ³ /MWh)	3 (wet cooling) 0.3 (dry cooling)	2 – 3 (wet cooling) 0.25 (dry cooling)	3 (wet cooling) 0.2 (dry cooling)	0.05 – 0.1 (mirror washing)
Application type	On-grid	On-grid	On-grid	On-grid / off-grid
Suitability for air cooling	Low to good	Good	Low	Best
Storage with molten salt	Commercially available	Commercially available	Possible, but not proven	Possible, but not proven

TES: Thermal Energy Storage.

* upper limit if the solar tower powers a combined cycle turbine.

A PTC consists on a reflective surface (mirror) with a linear parabolic shape and a receiver located on the focal line of the cylindrical parabola. Sunrays are reflected by mirrors so the receiver can collect concentrated solar radiation. This radiation is then transformed into heat, and transmitted to a fluid transported through the receiver. Figure 2.2 shows the process to convert solar radiation into heat, as explained before. PTCs operate at low-to-medium temperatures, with the working fluid reaching between 50°C and 400°C

[3], a range of temperatures where many industrial processes are carried out. Table 2.2 show information about general advantages and disadvantages of PTC technology.

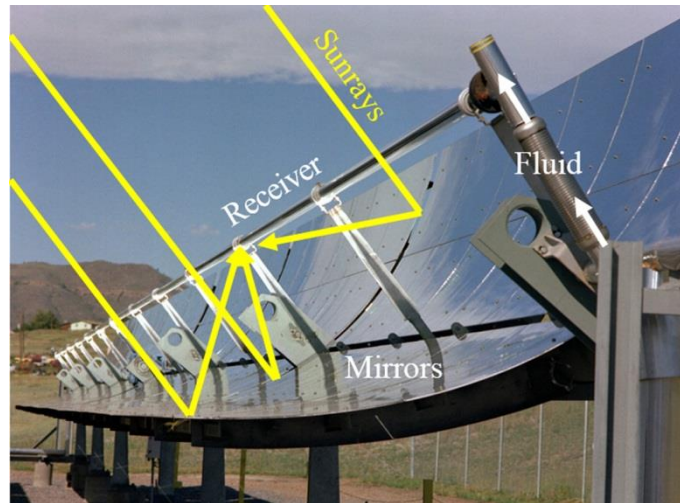


Fig. 2.2 – Parabolic Trough Solar Collector

Table 2.2 – Advantages and Disadvantages of PTC technology

Advantages	<ul style="list-style-type: none"> - Low emissions to the environment during lifespan: According to Burkhardt et al. [4] and Klein and Rubin [5], a Concentrating Solar Power (CSP) plant releases up to 30-70kgCO₂eq/MWh, which is lower compared to 400kgCO₂eq/MWh reported for a natural gas plant. - Lower maintenance and operating (O&M) costs: SEGS plants (California, USA) operates with an estimated cost of USD \$ 0.04/kWh [1]. - Long lifespan: PTCs have longer lifespan because they operate at moderate temperatures.
Disadvantages	<ul style="list-style-type: none"> - Large land area required: Large areas or land are required to collect enough heat to meet the energy load of the process due to the diffuse nature of solar radiation. - High initial investment and medium-long term recovery: The general cost of manufacturing and materials affects the total capital cost, recovery, and levelized cost of energy. - Intermittence of the resource: PTCs use direct solar radiation, so intermittence is a rule as energy cannot be collected at night.

2.1.2 Components

PTCs mainly consists of five principal components: mirrors, a supporting structure, a receiver, working fluid, and a tracking system. Each component accomplishes a specific

purpose and is made using materials according to its functions and desired properties. These components are explained in detail below.

2.1.2.1 Mirrors

Mirrors reflect and concentrate solar radiation into the receiver. They are made of high-reflective material layers (aluminum or silver) with protective-material layers against abrasion or corrosion. The most commonly used materials are silvered glass mirror, anodized sheet aluminum (sometimes coated with a polymer film), aluminized polymers and silvered polymer films. Table 2.3 shows desired properties of materials for mirrors.

Optical performance of mirrors can be affected by the surrounding atmosphere, manufacturing, or during normal operation; resulting in a decrement of thermal performance of the collector. Dirt, abrasion, and corrosion can affect the integrity of the mirrors, so it is important to protect them with appropriate coatings. Selecting the appropriate coating based on the desired properties of the reflective surface is mandatory for high thermal performance.

Geometrical errors take place in the collector during manufacturing and normal operation, and affect the concentration and consequently, optical efficiency. The most important errors are shape error, slope error, receiver deviation error, specularity error, tracking error, and frame deformation. Shape error estimates the eccentricity of the focal line (where the receiver is) due to deviations and misalignments of the mirrors. Slope error measures the deviation of the rays due to slightly ripples presented in the mirror shape. The receiver is not completely aligned to the focal line, so this misalignment is measured by the receiver deviation error. Specularity error refers to the error due to imperfect reflection of mirrors (no-ideal reflective materials). Due to the collector is not always perfectly pointing to the sun, tracking error takes place during operation (See section 2.1.2.5). Another factor that affects the geometry of the collector during operation is normal loading (principally by self-weight, wind, and torsional loads), which deforms the frame of the collector. These errors are represented in Figure 2.3 (the deviations are exaggerated to illustrate the origin of error).

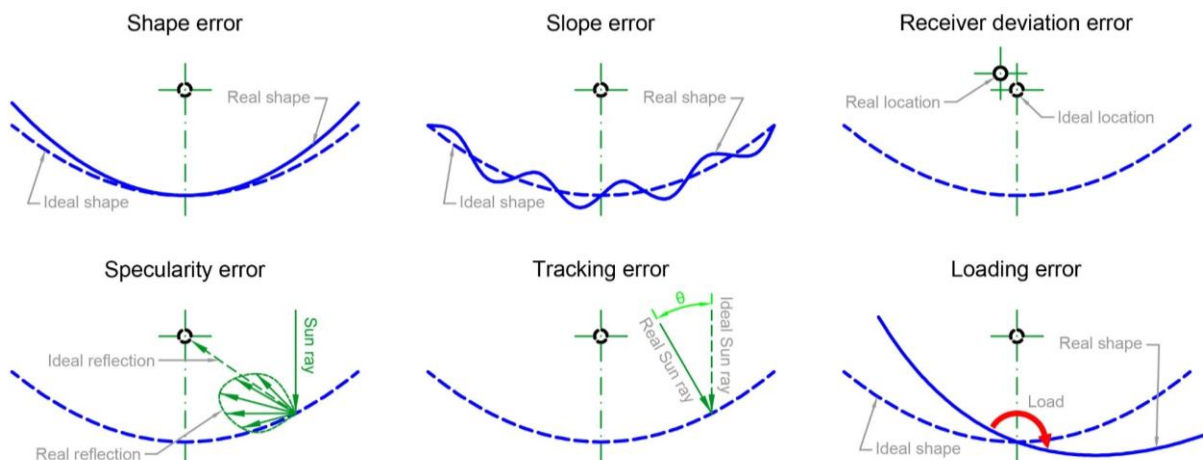


Fig. 2.3 – Geometrical errors in mirrors

Table 2.3 - Types of mirrors and their properties [7-13]

Type	Description	Typical hemispherical reflectance	Cost (\$/m ²) [14]	Properties
Silvered glass mirrors	A copper substrate (replaced by a water-insoluble precipitate layer in recent years) protected by paint coatings in the back, with a silvered-based coating and a high-transmittance low-reflective glass as cover (superstrate, usually a low-iron glass).	Up to 0.96	20 – 30	<ul style="list-style-type: none"> - High resistance to corrosion. - Commercially deployed. - Heavy and fragile.
Aluminized reflectors	Polished aluminum sheet with an aluminum-based reflective layer and oxide-enhancing layer.	Up to 0.9	< 20	<ul style="list-style-type: none"> - Lightweight and flexible. - Low cost. - High variability of durability. - More applicable for low-enthalpy concentrators. - Low durability in polluted locations.
Silvered polymer reflectors	Silvered-reflective layer coated with flexible polymer and a very thin UV-screening film superstrate.	0.9 – 0.95	20 – 30	<ul style="list-style-type: none"> - Under development - Less expensive. - High reflectance and lightweight. - Higher flexibility. - Long term performance needs to be proven.

2.1.2.2 Supporting structure

The main function of the structure is to provide stability and rigidity, fixing the receiver and mirrors principally. It is made by structural materials, such as aluminum or steel. The structure can be divided into 3 main sections:

- **Main support:** It serves as anchorage of the collector to the ground. Structurally, the main support must withstand wind loads due to the aperture of the collector being exposed to the wind [15].
- **Frameworks:** Provides rigidity to the mirror in order to maintain its cylindrical parabolic shape.
- **Brackets:** Fix the receiver at the focal line of the parabola.

A correct design of frameworks prevents misalignments during operation. The most important mechanical effects to avoid are bending and torsion of the framework, which are principally produced by self-weight and wind forces. Giannuzzi et al. [15] proposed structural design criteria for parabolic trough solar collectors, presenting a methodology to calculate loads for structural designs based on European codes. Common framework designs for PTCs used in CSP plants around the world are the torque box, torque tube, and struts.

2.1.2.3 Receiver

The principal function of the receiver is to absorb as much of the reflected solar radiation and to transfer this energy to the Heat Transfer Fluid (HTF) as heat. Receivers are made by a metal pipe coated with a selective material and covered with a glass. The cover glass minimizes heat losses on the pipe and protects it from degradation. A vacuum is applied in the annular region between the glass and the pipe to diminish heat losses and the receiver is sealed to prevent vacuum losses. Figure 2.4 shows the elements of a typical evacuated solar receiver for PTCs.

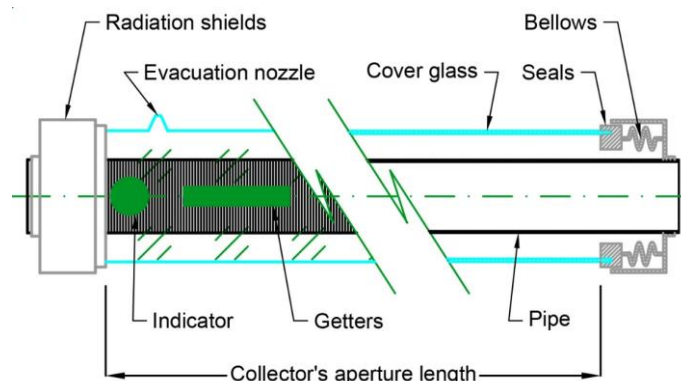


Fig. 2.4 – PTC solar receiver

The ideal material for a pipe receiver should have high resistance to corrosion, low thermal expansion, and high thermal conductivity. The most commonly used materials are stainless steels. Stainless steels have low thermal conductivity, a high resistance to

corrosion, and they are malleable (so fabrication of tubes is easy). The cover glass is made of a material with high transmittance, low reflectance, and low refractive index. It should transmit the highest possible amount of the incident radiation reflected from the mirrors. Anti-reflective coatings (ARCs) are applied to the external surface of the cover glass to enhance its transmittance. They create a transition on the refractive index from air to the cover [16]. The most commonly used types of glass in solar applications are silica and low-iron glasses (for example, borosilicate is extensively employed in solar applications) [17]. The selective coatings (SCs) absorb as much solar radiation as possible and transmit it to the pipe receiver. They are applied to the external surface of the pipe to increase heat flux absorption. The selective coating should have high short-wave absorptance, low long-wave emittance, good surface adhesion, and chemical stability in the working temperature range of collectors. Table 2.4 shows some pre-fabricated receivers and their characteristics.

2.1.2.4 Heat transfer Fluid

The HTF (also called “working fluid”) is a substance that captures heat coming from the receiver and use it as resource of energy in the process. This fluid should have high thermal capacity and thermal conductivity, low thermal expansion, low viscosity, minimal corrosive activity, low toxicity and thermal and chemical stability throughout its operating temperature range. Properties, advantages, and disadvantages of HTFs used in PTC are shown in Table 2.5.

Water and steam are commonly used in low-to-medium enthalpy process, including steam generation. Thermal oils are most used in solar power generation plants, along with a heat exchanger to generate steam for use in a Rankine cycle. Pressurized air is commonly used for drying and heating in buildings using Flat Plate Collectors, but it has been studied as an option for using in PTCs [18]. In fact, some studies suggest good performance in power plants with solar-assisted gas turbines [19-22]. Recently, the use molten salts and ionic liquids with good heat transfer capabilities have been reported in the literature. However, both molten salts and ionic liquids should overcome some challenges such as cost and operational aspects. Nanofluids have been developed for solar energy applications during recent years. A nanofluid is a fluid containing suspended solid nanometer-sized particles called nanoparticles, which increase the heat capacity and thermal conductivity of the mixture. These particles are commonly metals (in natural form or oxides). In the literature, there are some studies on nanofluids with applications in concentrated solar technology.

2.1.2.5 Solar tracking system

Main function of solar tracking system is to align the collector with the sun to maximize collector performance by one-axis rotation. Solar trackers can be classified as either passive and active. Passive trackers use the thermosiphon effect to align the collector, whereas active trackers use electronic signal conversion. Passive trackers are not commonly used in PTCs because they could be highly misaligned by wind during operation.

Table 2.4 - Characteristics of some receivers available in market [23-29]

Manufacturer	Archimede Solar Energy			Siemens ^(a)	Rioglass			Sunda			
Country	Italy			Germany	Spain			China			
Model	HCEMS11	HCEOI12	HCESHS12	UVAC 2010	UVAC 70-7G	UVAC 90-7G	PTR 4G	70-	SEIDO 6-1	SEIDO 6-2	SEIDO 6-3
Metal Receiver											
Length (m)	4.06	4.06	4.06	4.06	4.06	4.06	4.06	2	2	4.06	
Diam. (mm)	70	70	70	70	70	88.9	70	38	63.5	70	
Material	Stainless Steel										
Cover Glass											
Length (m)	3.9	3.9	3.9	NS	NS	NS	NS	NS	NS	NS	NS
Diam (mm)	125	125	125	115	115	135	125	102	102	115	
Thickness (mm)	3	3	3	NS	3	3	2.5	NS	NS	NS	
Material	Borosilicate (AR coated)										
Transmittance	0.966	0.966	0.966	0.964	0.967	0.964	0.97	0.95	0.95	0.95	
Selective Coating											
Absorptance	0.95	0.96	0.95	0.96	0.962	0.962	0.94	0.94	0.94	0.94	
Emittance (@ 400°C)	0.073	0.085	0.073	0.09	0.095	0.095	0.095	0.12	0.12	0.12	
Other characteristics											
Max. operating conditions	30 barg, 580°C	37 barg, 400°C	104 barg, 550°C	NS	40 barg, 350°C	40 barg, 350°C	41 barg, 350°C	15 barg, 300°C	30 barg, 390°C	40 barg, 450°C	
Lifetime (yr)	25	25	25	25	25	25	25	NS	NS	NS	
Annulus Pressure (mbar)	< 10 ⁻⁴	< 10 ⁻⁴	< 10 ⁻⁴	< 10 ⁻⁴	< 10 ⁻⁴	< 10 ⁻⁴	< 10 ⁻⁴	NS	NS	NS	

NS = Not specified

^(a) Rioglass bought Siemens CSP assets [25]

Table 2.5 - Heat transfer fluids used on PTC fields [30-41]

Fluid	Working temperature (°C)	General properties	Advantages	Disadvantages
Water	Up to 100	Odorless, relative low viscosity, non-toxic.	<ul style="list-style-type: none"> - No environmental risks (pollution or fire). - Low operational pressures. - Simple plant design. 	<ul style="list-style-type: none"> - Only for low enthalpy applications. - Requires water treatment.
Glycols	-50 - 300	High heat transfer properties (with combined with water), low viscosity, toxic (depending on the preparation).	<ul style="list-style-type: none"> - Anti-freezing properties (with the proper concentration). 	<ul style="list-style-type: none"> - Environmental risks (toxicity). - Used only in low enthalpy applications (when mixed with water). - Degradation with long-term operation.
Steam	Up to 500	High pressure and temperature applications.	<ul style="list-style-type: none"> - Higher working temperature. - Secondary HTF no needed. - No environmental risks (pollution or fire). - Easier plant design. 	<ul style="list-style-type: none"> - Evaporation (two-phase flow, heat losses in flashing). - Higher operational pressures. - Requires water treatment. - More complex solar field control. - Lack of suitable TES system.
Pressurized air	Up to 500	Low cost because of its abundance from atmosphere, low viscosity, low energy density, need to be dehumidified.	<ul style="list-style-type: none"> - Higher steam temperature. - Thermal storage enhancement. - No environmental risks (pollution or fire). 	<ul style="list-style-type: none"> - Poor heat transfer in the receiver. - More complex solar field control. - Higher operational pressures.

Table 2.5 – Continuation

Fluid	Working temperature (°C)	General properties	Advantages	Disadvantages
Synthetic oils	-90 - 400	High thermal capacity, low flow properties (compared with water), flammable, toxic.	- Higher thermal efficiencies is achieved (compared with others).	- Requires fire protection system.
Mineral oils	-10 - 300	Stability against thermal degradation and oxidation, relatively inexpensive, non-corrosive and non-toxic, flammable.	- Relative low operational pressures. - Relative lower power consumption (due to its low viscosity and density compared with others).	- Environmental risk (toxicity). - Heat exchangers required (for power generation).
Silicon oils	-40 - 400	Odorless, low pour point, nontoxic, low viscosity, expensive, flammable.	- Higher working temperature. - Lower operating pressures at high temperatures. - No pollution or fire hazards - Higher heat capacity. - Smaller TES size.	- High melting and freezing point (heat-tracing is required). - Highly corrosive at high temperatures. - More complex design. - Not proven technology.
Molten Salts	200 - 500	For high temperature applications, stable at high temperatures, low viscosity, high thermal capacity and density, corrosive, non-flammable.	- Lower freezing and melting point (compared with molten salts). - Reduced environmental risks (pollution).	- Higher power consumption (pump system). - Not proven technology.
Ionic liquids	-70 - 400	High thermal properties, wide liquid temperature range, low melting point, high viscosity and density, high chemical stability at high temperature, low volatility and flammability, expensive.	- Thermal enhancement.	- Sedimentation, clogging, and erosion. - Under investigation.
Nanofluids	-	Properties depend on type, size and concentration of the particle; the base fluid and additives. High concentration of particle increases both thermal conductivity and viscosity.		

There are three types of active trackers: closed-loop, open-loop, and hybrid-loop. Figure 2.5 shows how closed and open loop trackers work. Closed-loop trackers use a feedback-control signal conversion to align the collector. A light sensor detects the misalignment and send a signal to the control that moves the driver to align the collector until the sensor does not send signal (feedback). The principal advantage of this tracking method is its high tracking accuracy, but it is affected by shadowing. The control system can hardly recover the direction of the sun under long cloudy periods.

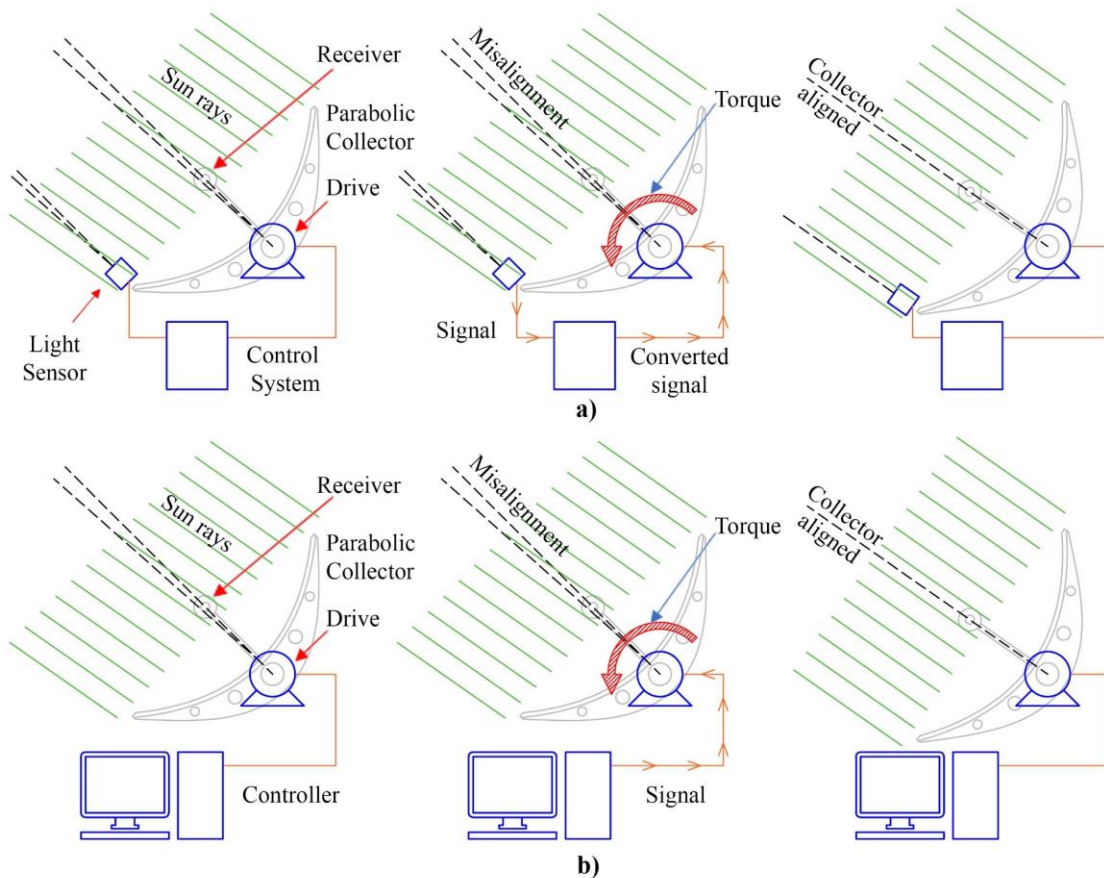


Fig. 2.5 – Operation of active trackers. a) closed-loop, b) open-loop.

Open-loop trackers can be classified as timed and altitude/azimuth. Both types use incremental movements to align the collector, the difference is the algorithm used to make the movements. Timed-control open-loop trackers are based on periodic movements, whereas altitude/azimuth-control trackers use astronomical data depending on location and time. The disadvantage of these methods is the accuracy of the equations used in the algorithms, which can lead to high misalignments.

Hybrid-loop trackers are a combination of both open-loop and closed-loop trackers. This kind of trackers overcome the disadvantages of both open-loop and closed-loop trackers. The basic strategy is to align the collector using the algorithm (open-loop) and then correct alignments using feedback sensors (closed-loop). Sensors are used in case of needed (high error in algorithm to track the sun).

2.2 Industrial applications

2.2.1 Heating

This group is the most deployed and mature application of PTC technology. Basic functionality is to heat the HTF and use its enthalpy as energy source in a heat process. Applications with a temperature lower than 100°C are considered as “low temperature applications”, while “medium temperature applications” are achieved by temperatures up to 450°C. Low-temperature PTC systems are commonly used in preheating and drying processes in commercial, residential, and industrial sectors, also called Solar Heating Industrial Processes (SHIPs). Steam generation (SG) and CSP are the principal applications for medium-temperature PTC systems. Figure 2.6 shows typical temperature range of some potential heating industrial applications.

CSP plants consist on replacing the boiler by a solar collector field to generate steam and impulse a turbine as a common Rankine cycle. Typical CSP plants have a thermal storage system, as shown in Figure 2.7. Thermal oils are the most used HTF in these systems due to their cost, chemical stability and operational temperature range in liquid state. This kind of CSP plants use heat exchangers to transmit heat from the oil to water. The installed capacity of CSP plants has increased in the last decade from approximately 500MW to 4500 MW, with the United States and Spain being the principal contributors in solar thermal power generation. Most of the electricity generation systems using solar thermal resources are PTC-based, accounting for approximately 85% of total current installed capacity worldwide [1].

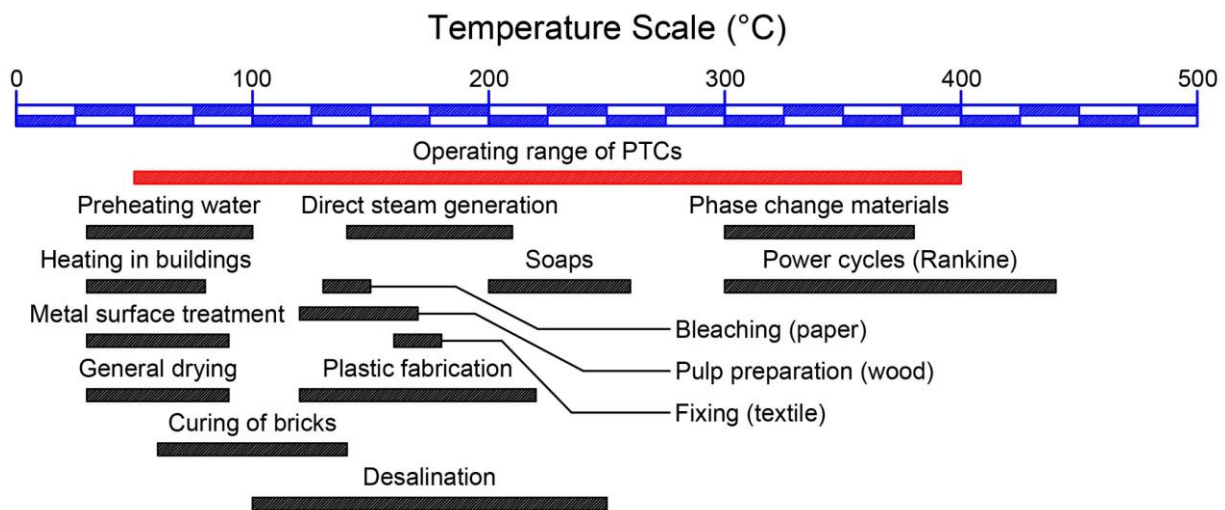


Fig. 2.6 – Temperature range of some potential thermal applications for PTCs

One of the most important applications for PTC technology is electricity generation (CSP plants). The installed capacity of CSP plants has increased in the last decade, with the United States and Spain being the principal contributors in CSP generation. Most of the electricity generation systems using solar thermal resources are PTC-based, accounting for approximately 85% of total current installed capacity worldwide [1].

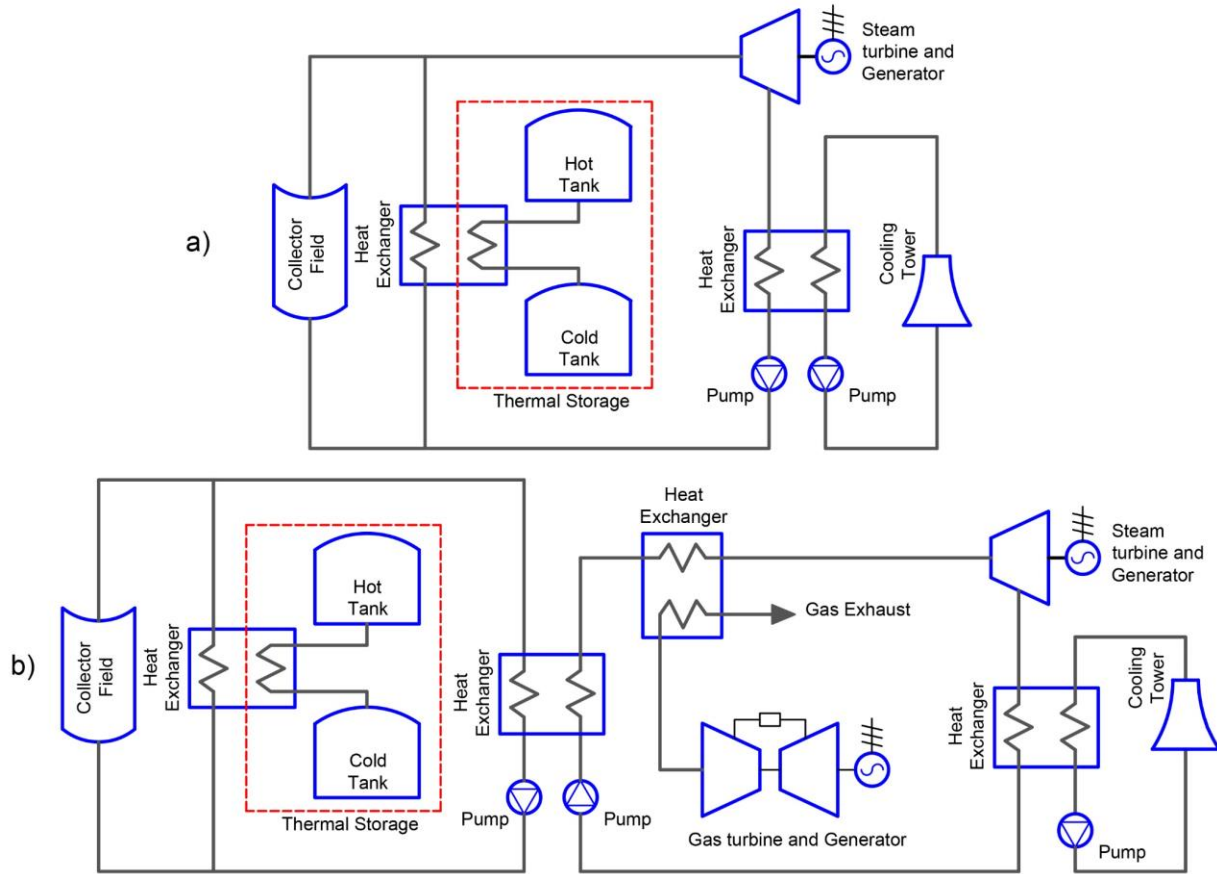


Figure 2.7 - CSP plant diagrams a) Direct SG, b) Indirect SG integrated to a combined cycle.

The U.S. National Renewable Energy Laboratory (NREL), in collaboration with the international program SolarPACES, has compiled data on functional and projected power plants that use solar concentration. A list of those plants is available on the internet, and can be classified by technology, country, or status [42].

PTCs are one of the technologies used in SHIPs that have recently been developed and implemented in small-to-medium scale plants around the world. Small-aperture collectors are the most used PTCs in these applications, which can reach temperatures up to 250°C [43]. Nowadays, the technology applied to SHIPs is still under development. Although, a number of installations and collectors with substantial technical improvements have been reported around the world, with good experience in performance and economics during the last years [44]. The principal advantages of this technology are their reduced risk (compared with volatility of fossil fuel prices), zero fuel cost, localized production, and low greenhouse gases (GHG) emission. Nevertheless, it still needs to overcome the barriers of the investment cost and complexity of the systems in order to have a good penetration into industry. Other barriers are the lack of technical information transfer, suitable design guidelines, and analysis tools [45].

2.2.2 Cooling

Solar radiation is used in solar cooling processes as thermal energy source to cool a space. Absorption and adsorption are the two main methods of solar cooling, both of them replace the compressor of conventional cooling processes with a “thermal compressor”. Both processes use heat to cool a fluid and then produced the extraction of heat from a space.

Absorption is the most common method of solar cooling. This process uses a fluid-fluid mixture (also called working pair) as the refrigerant. Basic phenomena is a volumetric effect of two fluids. The fluids of the working pair make a strong solution when mixed at low temperatures and they can be separated when the mixture is heated. The solute is converted into a gas and the solvent remains in liquid state when the mixture is heated. Later, the mixture release heat to the ambient and it captures the solute to make the solution. The cycle consists on the following steps.

1. The mixture is separated in the generator by heating.
2. The solute (gas) is condensed, and it rejects heat to the ambient space. The solute is then expanded and later evaporated by heat collected from the refrigerated space (as in traditional cooling systems).
3. The heated solute is then mixed with the solvent in the absorber.
4. The mixture is pumped to the generator and preheated by a heat exchanger with pure solvent coming from the generator.
5. The mixture is heated again in the generator, closing the cycle.

Single-effect and double-effect cycles are the most common processes in absorption cooling. Figure 2.8 shows a schematic diagram of single and double effect absorption cycles. Double effect solar cooling consists on a two-steps thermal compression. The most commonly used working pair in solar absorption systems are lithium-bromide and water-ammonia. Marcriss et al. [46] reported on other combinations of working pairs.

Solar adsorption cooling processes are completely different from absorption processes. The physical principle behind adsorption cooling is a surface-based phenomenon where a porous material (adsorbent) captures vapor from a fluid (refrigerant). The adsorbent is regenerated by heating. Adsorption processes differ from absorption because the working pair consists of a solid-fluid combination and because the heating intermittent, not continuous (the adsorbent is heated whenever it is saturated) [47]. Adsorption cycles require very low or no mechanical or electrical input, but thermal input (e.g., from the collector field) is important, and it works intermittently with the solar resource.

The most commonly used adsorbent materials are zeolite, activated carbon, and silica gel, and the most commonly used refrigerants are ammonia, methanol, and water. Sumathy et al. [48], Masesh [49] and Fernandes et al. [50] reviewed solar adsorption processes and the material characteristics of adsorption working pairs. A general adsorption cycle works as follow, and Figure 2.9 shows a schematic diagram of an adsorption solar cooling system.

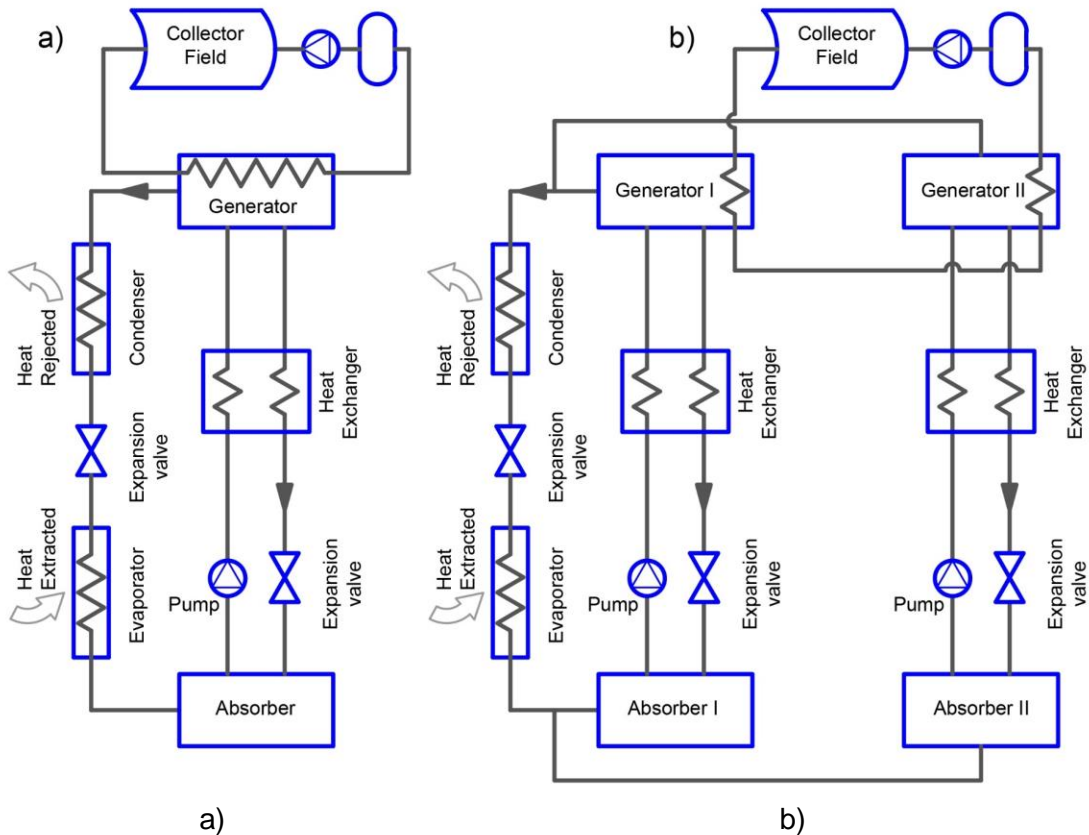


Fig. 2.8 – Absorption solar cooling systems. a) single effect, b) double effect

1. The refrigerant is evaporated by heat from the refrigerated space.
2. In the adsorption chamber, the vaporized refrigerant is adsorbed.
3. When the adsorption chamber is heated, the vapor is released and condensed, rejecting heat to the ambient space.
4. The condensates are stored in a tank.
5. Finally, the condensates are evaporated again, closing the cycle.

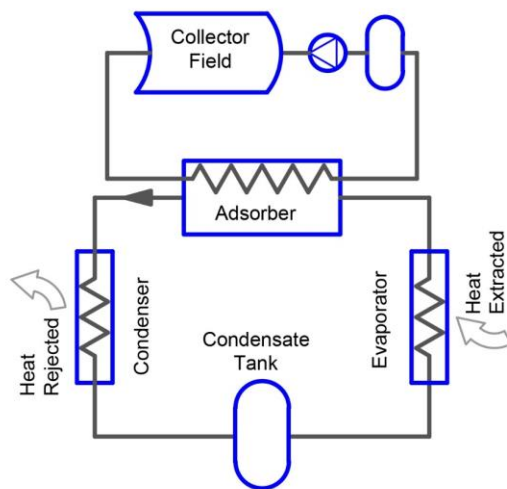


Fig. 2.9 – Adsorption solar cooling system

The general advantage of solar cooling technologies is a lower energy consumption than conventional vapor-compressor systems. The working pair (in a liquid phase) is pumped in solar absorption cooling rather than using a compressor in conventional cooling processes, and there is almost no mechanical input in adsorption cooling, as described before. Other advantages are that solar cooling systems has low noise and low vibration because they have fewer moving parts. The principal disadvantage is their low coefficient of performance (COP), with reported a COP of around 0.7 for single-effect absorption, 1.2 for double-effect absorption, and 0.1 – 0.2 for adsorption [51], compared with a COP of 3 – 4 for conventional vapor-compression systems.

Nowadays, the market of cooling systems is principally dominated by non-concentrating technologies. Up to 3% of the installed capacity is driven by concentrated technologies [52]. Nevertheless, concentrating technologies are suitable to be connected to solar-assisted double-effect absorption systems in locations with high solar radiation (e.g., Southern Europe or North America) [53]. International Energy Agency (IEA) SHC Task 53 is on the effort to assist sustainability of solar driven cooling systems and heating in buildings [54].

2.2.3 *Seawater desalination*

Seawater desalination is the process by which minerals are separated from seawater to produce fresh water. There are four types of desalination systems which are explained below.

- a) Thermal processes (phase change) uses thermal energy to separate the brine, and the most commonly used methods are multi-stage flash (MSF) and multi-effect distillation (MED).
- b) Single-phase processes use mechanical separation by passing seawater through filter membranes that trap minerals. Reverse osmosis (RO) and forward osmosis (FO) are the most frequently used methods in single-phase processes.
- c) Electric processes are based on cationic and anionic ion-exchange effects. Cathode and anode membranes are arranged alternately and exposed to an electric field, allowing them to trap salt particles and separate them from seawater. The principal methods of electric processes are electro-dialysis, ion-exchange, and capacitive deionization.
- d) Hybrid processes usually mix phase-change with single-phase processes, such as membrane distillation method.

Solar seawater desalination with PTC technology has direct participation only in phase-change processes as PTCs provide thermal energy. However, there are some reports on single-phase processes powered by organic Rankine cycles based on PTCs [55-58]. Patil et al. [59] suggested that the approach of PTC-based CSP-powered RO processes could provide better economical and operational characteristics.

In desalination applications, there have been noted that PTC technology is still under development for proven installations. Buenaventura and García-Rodríguez [60] reviewed

about the potential of solar energy in desalination applications. They also expose the comparison of different methods and technologies used. The authors conclude that RO/PTC systems driven Organic Rankine Cycle have the opportunity to address market development.

2.2.4 Water decontamination

Disinfection is the process of removing hazardous compounds such as heavy metals, organic compounds, and chemical substances from water. Advanced oxidation processes (AOPs) offer a feasible and sustainable alternative for disinfecting water, specially the degradation of resistant material prior to a biological treatment and treatment of refractory organic compounds [61]. Kabra et al. [62] reviewed methods for treatment of hazardous organic and inorganic compounds. They presented a list of previous studies on the removal of heavy metals using photocatalysis. AOPs generate a high concentration of oxidants (usually hydroxyl radical, OH^\cdot) to oxidize polluting matter that would not be easy to separate by biological degradation. There are some AOPs that use UV radiation as an energy source to produce the oxidants, but heterogeneous photocatalysis (HPC) with TiO_2 and photo-Fenton process (PFP) are the most commonly used methods in solar applications. These processes generate hydroxyl radicals ($^\cdot\text{OH}$) when UV radiation activates the catalyst in an atmosphere with oxygen. Malato et al. [63] presented a review on disinfection by photocatalysis, and compared HPC and PFP reactor design requirements.

Solar disinfection is usually realized in batch mode [64-65]. General purposes of water decontamination are for drinking water or agricultural applications [66]. The process consists on mixing the catalyst in water to suspend particles in the fluid, then the mixture is pumped to the solar field to realize the chemical processes before returning to the mixer. This process repeats continuously until the pollutants are degraded. The collector has the same characteristics as explained before, but the receiver is replaced with a glass pipe that is transparent to solar UV radiation. Historically, the first photoreactors were based on PTCs [63], but non-concentrating collector (NCC) and compound parabolic collector (CPC) technologies have scaled up in the past few decades. It is not easy to compare solar disinfection systems against conventional systems, which is an obstacle to industrial application. However, solar photocatalysis is a promising technology when compared to others because of its low impact, according to Malato et al. [63].

2.2.5 Concentrating photovoltaics

Concentrating photo-voltaic (CPV) generation is the direct conversion of solar energy into electrical energy using semiconductor materials under concentrated sunlight. The physical principle behind the operation of the solar cell is the photoelectric effect, which consists of generating a potential difference within a semiconductor when it is exposed to sunlight. The first photovoltaic cells appeared in the late nineteenth century, but the first performance test records of photovoltaic cells under concentrated light occurred during the early 1960s [67]. Research on photovoltaic concentrator (PVC) technology has

increased since then, and now, PTC technology can actively participate in this application because of its advantages and maturity.

A PVC operates in the same way as thermal concentrator, but with a modified receiver with photovoltaic (PV) cells in its surface. Concentrated sunlight strikes the PV cells, which convert solar radiation into electricity. It is known that PV cells do not convert all the incident energy into electricity, and most of this rejected energy is converted into heat. This heat causes the temperature of the cell to increase, affecting its efficiency. A way to diminish this effect is to cool the cells with a fluid flowing in the inside-side of the receiver. These collectors are known as thermal-photovoltaic concentrators (T-PVC). PV cells used in concentrating photovoltaics are designed to resist high incident radiation, so the use of Si-based cells depends on the concentration factor of the PVCs, as shown in Table 2.6.

Table 2.6 – Characteristics of concentrating photovoltaic applications

Concentration type	Concentration factor	Collector Type	Cell type
High	> 400	PD	Multi Junction
Medium	3 – 100	PTC, LFC	Silicon and others
Low	3	CPC	Silicon

Principal advantages of PVCs over non-concentrating PV systems is that they have a higher efficiency and require fewer PV cells. Nowadays, there are number of PV cells that operate under high concentrated sunlight with higher efficiencies than common Si-based cells, as shown in Figure 2.10. Green et al. [68] published a list of efficiencies of PV cells and modules for PV technologies. Concentrating photovoltaics is still under development and is not yet a commercially proven technology. However, it has good future potential, according to [69-75].

2.3 Performance analysis methods

Performance analysis can be classified into two main types: thermal and optical. Thermal performance analysis quantifies the solar-energy-to-heat conversion that a collector can supply to a thermal load. Optical performance analysis measures the quantity of radiative incident energy in the receiver compared to the energy flux in the collection area. These types of analysis are explained in detail below.

2.3.1 Thermal performance

Thermal performance can be classified as shown in Figure 2.11. Mathematical models use formulas to define heat transfer and fluid mechanics to numerically obtain thermal performance. Experiments are based on field measurements taken to obtain a more realistic performance. The principal advantage of experiments is that they consider complex phenomena (implicit in the measurements) that may be difficult to incorporate into models. The advantages of mathematical models are their simplicity and low cost compared to experiments.

Best Research-Cell Efficiencies

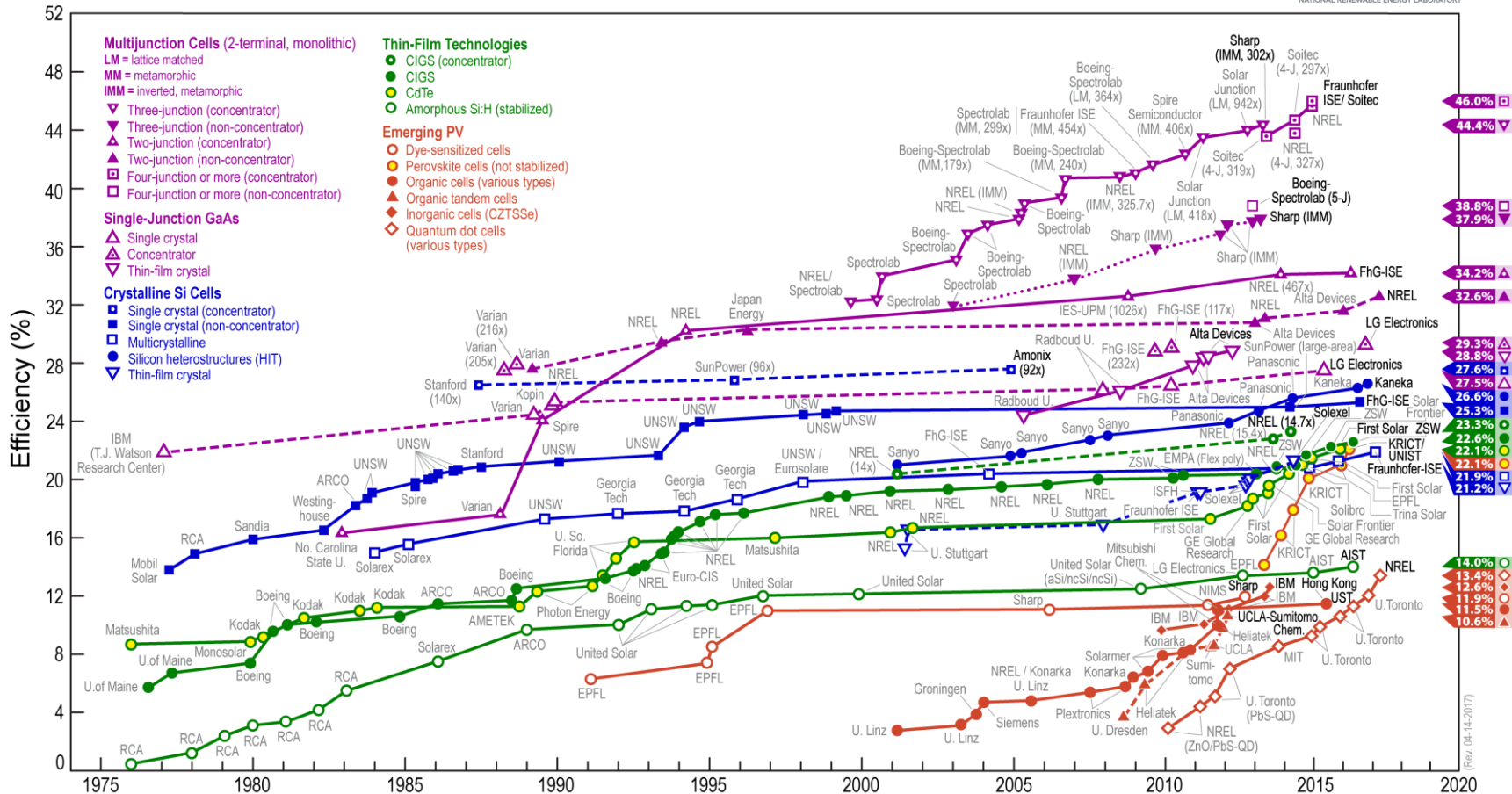


Fig. 2.10 – Evolution of solar cell technology. Borrowed from NREL website (www.nrel.gov/pv)

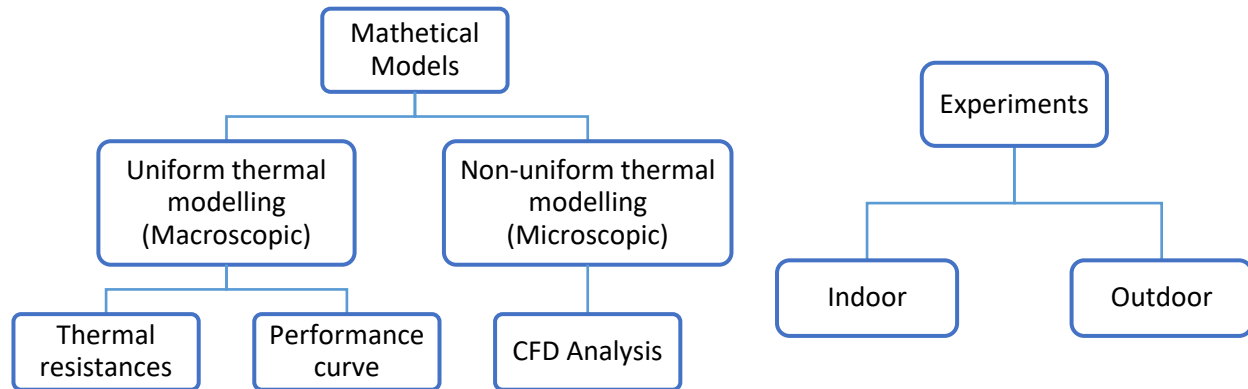


Fig. 2.11 – Classification of thermal performance analysis.

Thermal performance analysis with thermal resistance modeling, thermal parameter characterization (performance curve), and Computational Fluid Dynamics (CFD) modeling are the most frequently used methods in thermal energy balance. Many studies in the literature use these methodologies with experimental validation of mathematical modeling. One-dimensional and steady-state heat transfer are the most common assumptions used throughout the literature to model the thermal behavior of PTCs. Thermal resistance modeling uses a thermal circuit (analogous to electrical) to realize heat transfer and energy balance. The surfaces are the nodes, heat transfer are the currents, and temperatures are voltage in the model. The present study is based on this kind of models (See Chapter three for more information).

Thermal parameter characterization uses mathematical models of thermal performances usually based on experiments. The experimental data is adjusted to a mathematical model that express the thermal behavior of a PTC. Common mathematical models can be based on steady or quasi-dynamic state thermal behavior. Table 2.7 describes some studies found in the literature about thermal behavior.

CFD analysis uses a discretization of the control volume to approximate the solution of the governing equations of heat transfer and fluid mechanics. There are three basic techniques used: Finite Difference Analysis (FDA), Finite Volume Analysis (FVA), and Finite Element Analysis (FEA). FDA uses truncated series expansions for partial derivatives (usually a Taylor series) and a regular discretization of the domain. This method is easy to apply in simple geometric shapes, but it is not suitable for cases when many elements or a higher order in an expansion series are required to increase accuracy. FVA and FEA are useful for irregular shapes of control volume domain or when elements of different sizes or shapes (mesh) need to be used.

Indoor analysis is used for heat losses testing of receivers, whereas outdoor testing for thermal performance of collectors. Atmospheric factors, such as wind or ambient temperature, are totally or partially controlled in indoor testing. However, these factors are not controlled for outdoor experiments. Many studies in the literature describe experimentation using indoor and outdoor testing related with PTC technology. Standards are recommended to provide guidelines about instrument quality and how to proceed with

Table 2.7 - Experimental studies of collectors

Authors	Ref.	Element (Size)	Model	Test	Procedure	Characteristic equation
Burkholder and Kutscher	76	Receiver	UVAC3	Thermal losses	Indoor	$\dot{q}_l = 0.26\Delta T_{ab} + 1.05 \times 10^{-8} \Delta T_{ab}^4$
Pempeintner et. al	77	Receiver	PTR70	Thermal losses	Indoor	$\dot{q}_l = 0.176\Delta T_{ab} + 8.14 \times 10^{-9} \Delta T_{ab}^4$ ^{a)}
Burkholder and Kutscher	78	Receiver	PTR70	Thermal losses	Indoor	$\dot{q}_l = 0.141\Delta T_{ab} + 6.48 \times 10^{-9} \Delta T_{ab}^4$
Janotte et. al	79, 80	Collector (Large)	HelioTrough	Thermal performance	Outdoor	$\frac{Q}{A} = 0.816I_b K(\theta) - 0.0622\Delta T_f - 0.00023\Delta T_f^2 - 2653 \frac{dT_{1ave}}{dt}$
European Commission	81	Collector (Large)	EuroTrough	Thermal performance	Outdoor	$\eta = 0.7408 - 4.7851 \times 10^{-5} \Delta T_f - 5.58399 \times 10^{-7} \Delta T_f^2$
Fernández-García et. al	82	Collector (Small)	CAPSOL 01	Thermal / Optical performance	Outdoor	$\eta = 0.63 + 4 \times 10^{-4} \Delta T_f - 1.4 \times 10^{-5} \Delta T_f^2$
Moss and Brosseau	83	Collector (Large)	LS-2	Thermal performance	Outdoor	$\eta = 0.7859 - 3.57 \times 10^{-4} \Delta T_f - 4.33 \times 10^{-8} \Delta T_f^2$
Dudley et. al	84	Collector (Large)	LS-2	Thermal performance	Outdoor	$\eta = [0.733 - 7.276 \times 10^{-5} \Delta T_f] K(\theta) - 4.96 \times 10^{-3} T_r - 6.91 \times 10^{-4} T_r^2$ ^{b)}
Dudley et. al	85	Collector (Small)	IST	Thermal performance	Outdoor	$\eta = [0.7625 - 6.8366 \times 10^{-5} \Delta T_f] K(\theta) - 0.1468 T_r - 1.672 \times 10^{-3} T_r^2$ ^{c)}
Brooks	86	Collector (Small)	-	Thermal performance	Outdoor	$\eta = 0.5381 - 1.0595 T_r$ ^{d)}

Table 2.7 (Continuation)

Authors	Ref.	Element (Size)	Model	Test	Procedure	Characteristic equation
Valenzuela et. al	87	Collector (Large)	URSSA	Thermal / Optical performance	Outdoor	$\eta = 0.768K(\theta) - 6.343 \times 10^{-2} T_r - 2.074 \times 10^{-9} T_r^4$
Sallaberry et. al	88	Collector (Large)	URSSA	Thermal performance	Outdoor	$\frac{Q}{A} = 0.681 I_b K(\theta) - 2.96 \times 10^{-9} \Delta T_f^4 - 1671 \frac{dT_{1ave}}{dt}$ e)
McMahan et. al	89	Collector (Large) / Receiver	SkyTrough / PTR80	Optical efficiency / Thermal losses	Outdoor	$\dot{q}_l = 6.41 + 0.308 \Delta T_f - 1.95 \times 10^{-3} T_{1ave}^2 + 7.29 \times 10^{-6} T_{1ave}^3 + 1.08 \times 10^{-7} I_b K(\theta) \cos(\theta) T_{1ave}^2 + [0.205 \Delta T_f - 2.89] \sqrt{v_w}$
Hoste and Schuknecht	90	Collector (Large)	SkyTrough	Thermal performance	Outdoor	N.R.
Balghouthi	91	Collector (Small)	-	Thermal / Optical performance	Outdoor	$\eta = 0.5816 - 1.1777 T_r$
Janotte et. al	92	Collector (Small)	PTC 1800	Thermal performance	Outdoor	$\frac{Q}{A} = 0.683 I_b K(\theta) + 0.012 I_d - 0.0046 \Delta T_f^2 - 2100 \frac{dT_{1ave}}{dt}$ f)
Alfellag	93	Collector (Small)	-	Thermal performance	Outdoor	N.R.

a) Obtained based on data given in the report

c) Non-evacuated receiver, with black-nickel SC and Solgel glass

e) Without soiling factor

b) Evacuated receiver with Cermet SC

d) Glazed receiver

f) Quasi-dynamic model

N.R. Not reported

the measurements to obtain accurate results. ASHRAE 93, ISO 9806 and SRCC 600 are the most commonly used standards for thermal performance analysis with PTCs.

2.3.2 Optical performance

The optical efficiency of a collector (η_{op}) principally depends on the interception factor (γ), the transmittance of the cover glass (τ_{cg}), the absorptivity of the selective coating (α_{sc}), the reflectance of the mirrors (ρ_m), the incident angle modifier ($K(\theta)$), and soiling factor (F_c), as expressed in Equation 2.1. It is known that mirrors shape and receiver alignment are not perfect in practice, so it also involves a random error. This error is measured by the interception factor (γ), which combines the effects of misalignments and slope random error in mirrors.

$$\eta_{op} = \eta_{op,0} K(\theta) F_c = [\gamma \tau_{cg} \alpha_{sc} \rho_m] K(\theta) F_c \quad (2.1)$$

Ray-tracing techniques are used to obtain an estimation of interception factor of a PTC. These methods simulate the propagation of light through a media and surfaces with specific optical properties such as reflection, refraction, diffraction, and scattering. Monte Carlo ray tracing is the most commonly used method, which is based on probability distribution functions for predicting light ray paths. Photogrammetry is widely used for experimental measurement of interception factor. This and other experimental methods were described by Arancibia-Bulnes et al. [94].

It is known that during normal operation, PTCs are not always at 0° incidence, so optical efficiency is affected. The Incidence Angle Modifier $K(\theta)$ (IAM) takes into account the optical losses due to no-normal incidence during operation (such as end-effect losses). This factor is usually measured by experiments. Another important factor is the soiling factor F_c , which represents the ratio between the real-operation and nominal-clear mirror reflectance. During normal operation, cleaning the mirrors (washing) is a requirement for good performance, and this affects reflectance. For PTCs, common values of soiling factor are between 0.95 and 1 [18].

2.4 Basic concepts on performance of Parabolic-Trough collectors

2.4.1 Geometric factors

To understand performance of PTCs is important to know about geometry of concentrators. Equations 2.2 to 2.8 and Figures 2.11 to 2.13 express the basic geometric parameters involved in PTCs. The acceptance angle ($2\theta_m$) denotes the coverage of the angular area in which the solar radiation is captured by the receiver after passing through the opening of the collector with no-needed orientation. This angle depends on the location of the concentrator respect to the Sun as shown in Figure 2.11.

$$W_a = 4 \sqrt{h_p f} = 4f \tan\left(\frac{\varphi_r}{2}\right) = 2r_r \text{sen}(\varphi_r) \quad (2.2)$$

$$r = \frac{2f}{1 + \cos(\varphi)} \Rightarrow r_r = \frac{2f}{1 + \cos(\varphi_r)} \quad (2.3)$$

$$D = 2r_r \sin(\theta_s) = \frac{W_a \sin(\theta_s)}{\sin(\varphi_r)} \quad (2.4)$$

$$S = \frac{H_p}{2} \left\{ \sec\left(\frac{\varphi_r}{2}\right) \tan\left(\frac{\varphi_r}{2}\right) + \ln \left[\sec\left(\frac{\varphi_r}{2}\right) + \tan\left(\frac{\varphi_r}{2}\right) \right] \right\} ; H_p = 4f \quad (2.5)$$

$$C_r = \frac{W_a}{\pi D} = \frac{\sin(\varphi_r)}{\pi \sin(\theta_m)} \quad (2.6)$$

$$A_f \tan(\theta) = \frac{A_e}{A_a} ; A_a = W_a L \quad (2.7)$$

$$A_e = f W_a \tan(\theta) \left[1 + \frac{W_a^2}{48 f^2} \right] \quad (2.8)$$

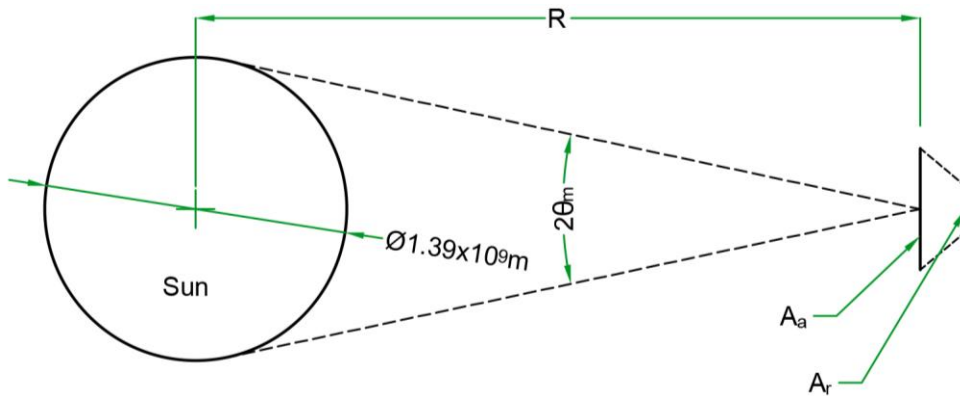


Fig. 2.11 – Definition of acceptance angle

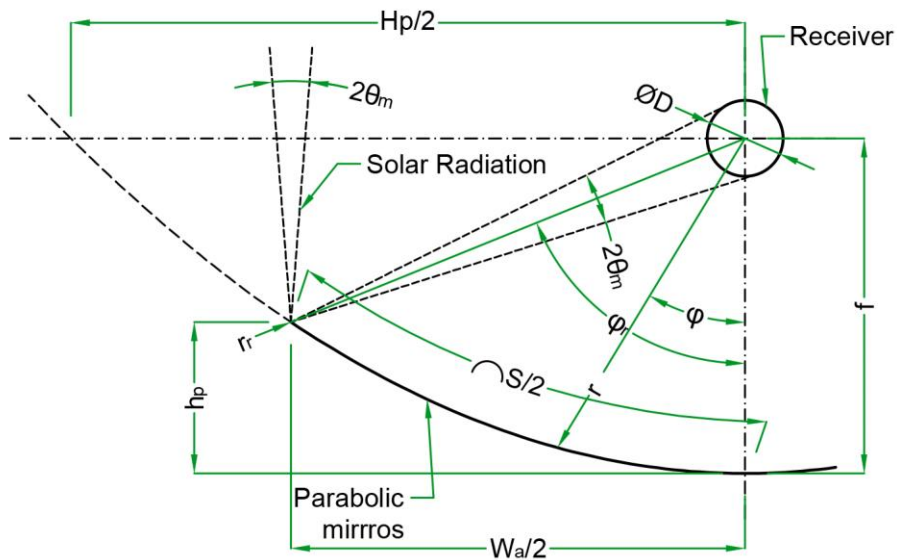


Fig. 2.12 – Geometry of a PTC

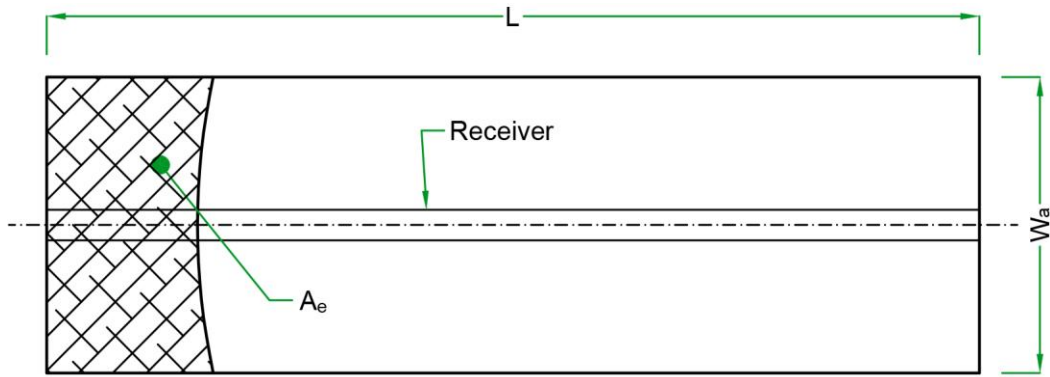


Fig. 2.13 – Description of end-effect losses

The incidence angle (θ) is defined as the angle between incident sunrays and the normal direction of the aperture plane of the collector. This angle is a function of the location and orientation of the collector, and time (day and hour). The slope angle (β) is defined as the angle between the aperture plane of the collector and a horizontal plane. Table 2.8 shows the correlations used to compute incidence and slope of surface angles of a PTC under ideal operation conditions according to its tracking mode [95].

Table 2.8 – Correlations for incidence angle and slope angle of surface for PTC

Tracking mode	Correlation of angles	Eq.
E-W	$\cos(\theta) = \sqrt{\sin^2(\alpha) + \cos^2(\delta)\sin^2(h)}$	(2.9)
	$= \cos(\Phi)\cos(h) + \cos(\delta)\sin^2(h)$	
N-S	$\tan(\beta) = \tan(\Phi) \cos(Z_s - z) $	(2.10)
	$\cos(\theta) = \sqrt{1 - \cos^2(\delta)\sin^2(h)}$	(2.11)
	$= \sqrt{\sin^2(\delta) + \cos^2(\delta)\cos^2(h)}$	
	$\tan(\beta) = \tan(\Phi) \cos(z) $	(2.12)

2.4.2 Thermal efficiency curve

The thermal efficiency curve (also known as the characteristic curve) describes thermal behavior of a collector. It relates thermal efficiency vs. temperature difference between the fluid and the ambient (or reduced temperature, which is the ratio of temperature difference and solar irradiance). Figure 2.14 shows the characteristic efficiency curve for solar collectors. It is noticed that with higher temperature difference or low solar irradiance, thermal efficiency decreases. These thermal losses are due to convective and radiative heat transfer from the receiver to the ambient. Conductive losses through brackets are practically insignificant.

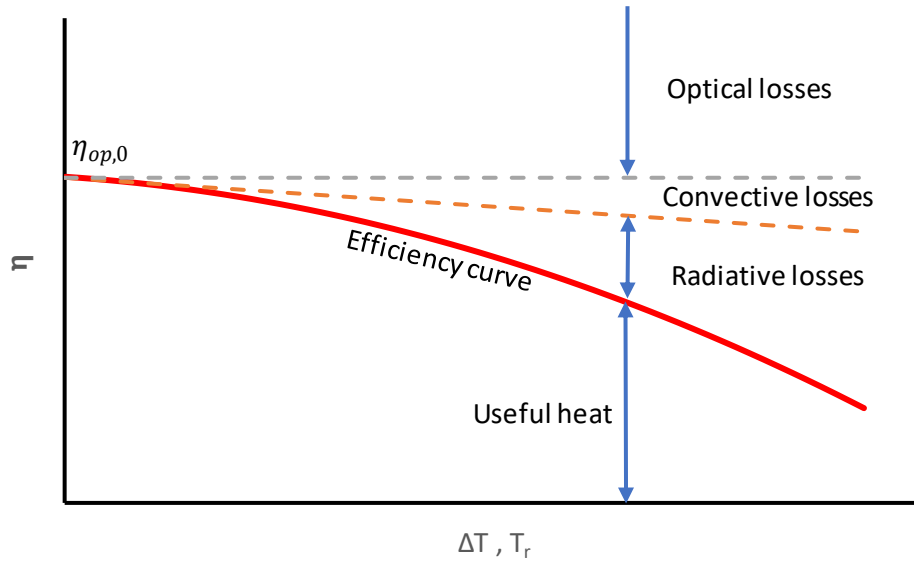


Fig. 2.14 – Thermal efficiency curve and components of heat losses

The efficiency curve is obtained based on experiments. Basic measurements are inlet, outlet and ambient temperature, direct beam solar irradiance, flow mass of the fluid, IAM, and aperture area. Coordinates (T_r, η) are obtained using Equations 2.13 and 2.14 and represented into a graph similar to Figure 2.14. The specific heat (C_p) is obtained depending on the fluid used to characterize the collector.

$$\eta = \frac{\dot{m}C_p(T_{out} - T_{in})}{K(\theta)I_b A_a} = \frac{Q_u}{Q_{in}} \quad (2.13)$$

$$T_r = \frac{T_m - T_\infty}{I_b} ; T_m = \frac{T_{out} + T_{in}}{2} \quad (2.14)$$

The experiments are carried out using standards. Most used standard to characterize PTCs are ASTM E-905, ISO 9806, FSEC 102, and SRCC 600. Each standard describes the procedures to realize the tests, basic instrumentation and quality to get reliable data, the mathematical model, and the conditions to carry out the tests. Some of these standards also describes tests for reliability during normal operation. Table 2.9 shows the tests and differences among all the standards used for thermal characterization of PTCs. Standard ASHRAE 93 is now withdrawn, and EN12975 has been replaced by ISO 9806. Multiple linear regression is the most used statistical technique to obtain the mathematical model of a collector, such as some showed in Table 2.7. Sometimes, higher-order terms (quadratic or others) are statistically insignificant, so they should not be taken into account in the mathematical model, making it a simplified equation.

Table 2.9 – Reliability and performance tests included in each standard [96 - 101]

Standard	ASHRAE 93	ASTM E-905	EN 12975	ISO 9806	FSEC 102	SRCC 600
Scope						
SLHC	√	√	√	√	√	√
SAHC	√	NS	X	√	√	√
T/PV	X	X	X	√	X	√
Durability / Reliability Tests						
Internal pressure	X	X	√	√	√	√
Pre-exposure	X	X	X	√	X	√
Leakage / Pressure drop ^{a)}	√	X	X	√	√	√
Rupture / Collapse ^{a)}	X	X	X	√	X	X
Max. Temp. Resistance	X	X	√	√	X	X
Stagnation Temp. Exposure	X	X	X	√	X	X
External thermal shock	X	X	√	√	√	√
Internal thermal shock	X	X	√	√	√	√
Rain penetration	X	X	√	√	X	X
Freeze resistance	X	X	√	√	X	X
Mechanical load	X	X	√	√	X	X
Impact resistance	X	X	√	√	X	√
Protection system	X	X	X	X	X	√
Final inspection	X	X	√	√	√	√

Table 2.9 (Continuation)

Thermal performance						
Time constant (τ)	√	√	X	√	√	√
Thermal efficiency for SLHC	√	√	√	√	√	√
Thermal efficiency for SAHC	√	NS	X	√	√	√
Thermal capacity IAM	X √	X √	√ √	√ √	X √	√ √
Mathematical model	Linear	NS	Quadratic Polinomial	/ Polinomial	Depends on the fluid used	Polinomial
State	Steady	Steady	Steady Quasi-dynamic	/ Quasi-dynamic		Quasi-dynamic
Test conditions	Clear sky	Clear sky	Depends on method used	Clear partly-cloudy sky /		Clear partly-cloudy sky
Minimum solar Irradiance of tests (W/m ²)	800	630	700	800	800	800
Minimum data points	4	4	*	4	4	4
Test duration	Max. of 5 min / τ	Max. of 5 min / 0.5τ	*	Max. of 15min / 4τ	*	Max. of 15min / 4τ
SLHC: Solar Liquid Heating Collector SAHC: Solar Air Heating Collector T/PV: Thermal / Photovoltaic a) Only for SAHCs			$\sqrt{}$: Included X: Not included NS: Not specified			

2.5 Nomenclature

2.5.1 Acronyms

AOP	Advanced Oxidation Process
ARC	Anti-Reflective Coating
CFD	Computational Fluid Dynamics
COP	Coefficient of Performance
CPC	Compound Parabolic Collector
CPV	Concentrating Photovoltaics
CSP	Concentrating Solar Power
FDA	Finite Difference Analysis
FEA	Finite Element Analysis
FO	Forward Osmosis
FVA	Finite Volume Analysis
GHG	Greenhouse Gasses
HPC	Heterogenous Photocatalysis
HTF	Heat Transfer Fluid
IEA	International Energy Agency
LFC	Linear Fresnel Collector
MED	Multi Effect Distillation
MSF	Multi Stage Flash
NCC	Non-Concentrating Collectors
O&M	Operational and Maintenance
PD	Parabolic Dish
PFP	Phot Fenton Process
PTC	Parabolic Trough Collector
PVC	Photovoltaic Concentrator
RO	Reverse Osmosis
SC	Selective Coating
SHIP	Solar Heating Industrial Process
SG	Steam Generation
ST	Solar Tower
TES	Thermal Energy Storage
T-PVC	Thermal-Photovoltaic Concentrator

2.5.2 Symbols

A_a	Aperture area (m ²)
A_e	End-effect area loss (m ²)
A_f	Area loss ratio (dimensionless)
C_p	Specific heat (J/kgK)
C_r	Concentration ratio (dimensionless)
D	Diameter of receiver (m)
F_c	Soiling factor (dimensionless)
f	Focal length (m)

H_p	Latus rectum (m)
h_p	Rim height (m)
h	Hour angle (rad)
I_b	Beam direct solar radiation (W/m ²)
$K(\theta)$	Incident angle modifier K as function of incidence angle θ
L	Length of collector (m)
\dot{m}	Mass flow (kg/s)
Q_{in}	Inlet heat (W)
Q_u	Heat received (W)
r	Polar radius of the parabola (m)
r_r	Rim radius (m)
S	Parabolic arc (m)
T_∞	Ambient temperature (°C)
T_{in}	Inlet fluid temperature (°C)
T_m	Average fluid temperature (°C)
T_{out}	Outlet fluid temperature (°C)
T_r	Reduced temperature (m ² K/W)
W_a	Aperture width (m)
Z_s	Surface azimuth angle (rad)
z	Solar azimuth angle (rad)

2.5.3 Greek letters

α	Altitude angle (rad)
α_{sc}	Absorptivity of the selective coating
β	Slope angle (rad)
γ	Interception factor
δ	Declination angle (rad)
η	Overall efficiency
η_{op}	Optical efficiency
$\eta_{op,0}$	Peak optical efficiency (at normal incidence)
θ	Incidence angle (rad)
θ_s	Half acceptance angle (rad)
ρ_m	Reflectance of the mirrors
τ_{cg}	Transmittance of the cover glass
Φ	Zenit angle (rad)
φ	Polar angle (rad)
φ_r	Rim angle (rad)

2.6 References

[1] International Renewable Energy Agency. Renewable power generation costs in 2014. IRENA Publications; 2015. 54 p.

- [2] International Renewable Energy Agency. Renewable energy technologies: cost analysis series (concentrating solar power). IRENA Publications; 2012. 48 p.
- [3] Kalogirou S. Solar thermal collectors and applications. Prog Energ Combust. 2004;30(3):231-95.
- [5] Burkhardt III J, Heath G, Turchi C. Life cycle assessment of a parabolic trough concentrating solar power plant and the impacts of key design alternatives. Environ Sci Technol. 2011;45(6):2457-64.
- [6] Klein S, Rubin E. Life cycle assessment of greenhouse gas emissions, water and land use for concentrated solar power plants with different energy backup systems. Energy Policy. 2013;63:935-50.
- [7] Granqvist CG. Preparation of thin films and nanostructured coatings for clean tech applications: a primer. Sol Energy Mater Sol Cells 2012;99:166–75
- [8] Kennedy C. Advances in concentrating solar power collectors: Mirrors and solar-selective coatings. Golden (CO, USA): NREL Publications;2007. 10p. Report No.: NREL/CP-52042260.
- [9] Czanderna A, Masterson K, Thomas T. Silver/glass mirrors for solar thermal systems. Springfield (VA, USA): NREL Publications; 1985. 72p. Report No.: SERI/SP-271-2293
- [10] Mescia L, Losito O, Prudeniano F. Innovative materials and systems for energy harvesting applications. Hershey (PA, USA): IGI Global; 2015. Chapter 10, Silver coating with protective transparent films for solar concentrators; p. 271-89.
- [11] Kennedy C, Terwilliger K, Milbourne M. Development and testing of solar reflectors. Denver (CO, USA): NREL Publications;2004. 5p. Report No.: NREL/CP-520-36582.
- [12] Silva P. Energia Solare termodinamica [pdf on internet]. Legnano (IT): Politecnico de Milano, Dipartimento d Energia; 2013 [cited 2017 Feb 10]. Available from: www.euroimpresa.it/sites/default/files/131113111951_Concentrating%20Solar%20Power_materiale.pdf.
- [13] García-Segura A, Fernández-García A, Ariza MJ, Sutter F, Valenzuela L. Durability studies of solar reflectors: A review. Renew Sust Energy Rev. 2016;62:453-67.
- [14] Green Rhino Energy. Solar glass & mirrors [internet]. 2016, [cited 2018 Feb 2]. Available from: http://www.greenrhinoenergy.com/solar/technologies/solar_glass.php.
- [15] Giannuzzi G, Majorana C, Miliozzi A, Salomoni V, Nicolini D. Structural design criteria for steel components of parabolic-trough concentrator. J Sol Energ-T ASME. 2007;129:382-90.

- [16] Atkinson C, Sansom C, Almond H, Shaw C. Coating for concentrating solar systems – A review. *Renew Sust Energ Rev.* 2015;45:113-22.
- [17] Deubener J, Hensch G, Moiseev A, Bornhoft H. Glasses for solar energy conversion systems. *J Eur Ceram Soc.* 2009;29(7):1203-10.
- [18] Zarza Moya E. Parabolic trough concentrating solar power (CSP) systems. In: Lovegrove K, Stein W, editors. *Concentrating solar power technology: principles, developments and applications.* Woodhead Publishing; 2012, pp. 197-239.
- [19] Amelio M, Ferraro V, Marinelli V, Summaria A. An evaluation of the performance of an integrated solar combined cycle plant provided with air-linear parabolic collectors. *Energy.* 2014;69:742–8.
- [20] Bellos E, Tzivanidis C, Antonopoulos KA. Parametric analysis and optimization of a solar assisted gas turbine. *Energy Conver Manag.* 2017;139:151–65.
- [21] Ferraro V, Imineo F, Marinelli V. An improved model to evaluate thermodynamic solar plants with cylindrical parabolic collectors and air turbine engines in open Joule–Brayton cycle. *Energy.* 2013;53:323–31.
- [22] Cipollone R, Cinocca A, Gualtieri A. Gases as working fluid in parabolic trough CSP plants. *Proced Comp Scien.* 2013;19:702-11.
- [23] Archimede Solar Energy. Receiver tube – Download [internet]. Italy [cited 2017 Mar 02]. Available from: www.archimedesolarenergy.it/download.htm.
- [24] Siemens. The unrivaled benchmark in solar receiver efficiency [pdf on internet]. Erlangen (GER): Siemens Press; 2010 [cited 2017 Mar 02]. Available from: www.energy.siemens.com/nl/pool/hq/power-generation/renewables/solar-power-solutions/concentrated-solar-power/downloads/Siemens-UVAC-2010.pdf.
- [25] Steitz C, Sheahan M. Rioglass Solar buys some solar assets from Siemens [internet]. Reuters. Thomson Reuters; 2013 [cited 2018 Feb 17]. Available from: www.reuters.com/article/rioglass-siemens/rioglass-solar-buys-some-solar-assets-from-siemens-idUSL5N0HE0JY20130918
- [26] Rioglass. Rioglass UVAC 70 7G. [internet]. Spain [cited 2017 Mar 02]. Available from: www.rioglass.com/?page_id=1925.
- [27] Rioglass. Rioglass UVAC 90 7G. [internet]. Spain [cited 2017 Mar 02]. Available from: www.rioglass.com/?page_id=1899.
- [28] Rioglass. Rioglass PTR 70 4G. [internet]. Spain [cited 2017 Mar 02]. Available from: www.rioglass.com/?page_id=2296.

- [29] Sunda Solar. Products [internet]. China [cited 2017 Mar 02]. Available from: www.sundasolar.com/product_index.html.
- [30] Price H, Lupfert E, Kearney D, Zara E, Cohen G, Gee R, et al. Advances in parabolic trough solar power technology. *J Sol Energ Eng*. 2002;124(2):109-25.
- [31] Vivar M, Everett V. A review of optical and thermal transfer fluids used for optical adaptation or beam-splitting in concentrating solar systems. *Prog Photovoltaics*. 2014;22(6):612-33.
- [32] Vignarooban K, Xu X, Arvay A, Hsu K, Kannan A. Heat transfer fluids for concentrating solar power systems- A review. *Appl Energ*. 2015;146:383-96.
- [33] Bellos E, Tzivanidis C, Antonopoulos K, Daniil I. The use of gas working fluid in parabolic trough collectors – An energetic and exergetic analysis. *App Therm Eng*. 2016;109:1-14.
- [34] He G, Fang X, Xu T, Zhang Z, Gao X. Forced convective heat transfer and flow characteristics of ionic liquid as a new heat transfer fluid inside smooth and microfin tubes. *Int J Heat Mass Tran*. 2015;91:170-7.
- [35] Wadekar V. Ionic liquids as heat transfer fluids – An assessment using industrial exchanger geometries. *App Therm Eng*. 2017;111:1581-7.
- [36] Van Valkenburg M, Vaughn R, Williams M, Wilkes J. Thermochemistry of ionic liquid heat-transfer fluids. *Thermochimica Acta*. 2005;425(1-2):181-8.
- [37] Chen H, He Y, Zhu j, Alias H, Ding Y, Nancarrow P, et. al. Rheological and heat transfer behavior of the ionic liquid, [C4min][NTf2]. *Int J Heat Fluid Flow*. 2008;29:149-55.
- [38] Hussein A. Applications of nanotechnology to improve the performance of solar collectors – Recent advances and overview. *Renew Sust Ener Rev*. 2016;62:767-92.
- [39] Weinrebe G, von Reeken F, Arbes S, Schweitzer A, Wöhrbach M, Finkbeiner J. Solar thermal heat & power- parabolic trough technology for Chile: Current state of the art of parabolic trough collector technology. GIZ GmbH; 2014. 116 p.
- [40] Enteria N, Akbarzadeh A. Solar energy sciences and engineering applications. London (UK): CRC Press; 2014. Chapter 14, Solar energy conversion with thermal cycles; p. 413-84.
- [41] Andrej L, Nam Y, Wang E. Heat transfer fluids. *Annual Rev Heat Transf*. 2012;15:93-129.

- [42] NREL. Concentrating Solar Power Projects [internet]. USA: NREL. [cited 2017 Ene 19]. Available from: <https://www.nrel.gov/csp/solarpaces/index.cfm>.
- [43] IEA. Process Heat Collectors: State of the Art and available medium temperature collectors [pdf on internet]. 2015 [cited 2018 Mar 07]. Available from: http://task49.iea-shc.org/data/sites/1/publications/Task%2049%20Deliverable%20A1.3_20160504.pdf.
- [44] Hess S. Solar thermal process heat (SPH) generation. In: Stryi-Hipp G, editor. Renewable heating and cooling: Technologies and applications. 2016. p. 41-66.
- [45] IRENA, ETSAP. Solar heat for industrial processes: Technology brief. 2015.
- [46] Marcriss R, Gutraj J, Zawacki T. Absorption fluid data survey: final report on worldwide data, ORLN/sub/8447989/3. Inst. Gas Tech 1988.
- [47] Kim D, Infante C. Solar refrigeration options – a state-of-the-art review. Int J Refrig. 2008;31(1):3-15.
- [48] Sumathy K, Yeung K, Yong L. Technology development in the solar adsorption refrigeration systems. Prog Energy Combust Sci. 2003;29(4):301–27.
- [49] Mahesh A. Solar collectors and adsorption materials aspects of cooling system. Renew and Sust Energy Rev. 2017;73:1300–12.
- [50] Fernandes M, Brites G, Costa J, Gaspar A, Costa V. Review and future trends of solar adsorption refrigeration systems. Renew Sust Energy Rev. 2014;39:102–23.
- [51] Sarbu I, Sebarchievici C. Review of solar refrigeration and cooling systems. Energy Build. 2013;67:286–97.
- [52] Allouhi A, Kousksou T, Jamil A, Bruel P, Mourad Y, Zeraouli Y. Solar driven cooling systems: An updated review. Renew Sust Energy Rev. 2015;44:159-81.
- [53] Ghafoor A, Munir A. Worldwide overview of solar thermal cooling technologies. Renew Sust Energy Rev. 2015;43:763-74.
- [54] IEA SHC. New generation solar cooling and heating systems: PV or solar thermally driven systems [pdf on internet]. 2013 [cited 2018 Mar 07]. Available from: http://task53.iea-shc.org/Data/Sites/53/media/documents/work-plan-task-53-solar-cooling_2016_05_15.pdf.
- [55] Ortega-Delgado BCA, García-Rodríguez L, Alarcón-Padilla D-C. Thermoeconomic comparison of integrating seawater desalination processes in a concentrating solar power plant of 5 MWe. Desalin. 2016;392:102–17.

- [56] García-Rodríguez L, Delgado-Torres A. Solar-powered Rankine cycles for fresh water production. *Desalin.* 2007;212(1):319–27.
- [57] Delgado-Torres A, García-Rodríguez L, Romero-Ternero V. Preliminary design of a solar thermal-powered seawater reverse osmosis system. *Desalin.* 2007;216(1):292–305.
- [58] Nafey A, Sharaf M. Combined solar organic Rankine cycle with reverse osmosis desalination process: Energy, exergy, and cost evaluations. *Renew Energy.* 2010;35(11):2571–80.
- [59] Patil V, Biradar V, Shreyas R, Garg P, Orosz M, Thirumalai N. Techno-economic comparison of solar organic Rankine cycle (ORC) and photovoltaic (PV) systems with energy storage. *Renew Energy.* 2017;113:1250–60.
- [60] Buenaventura A, García-Rodríguez L. Solar thermal-power desalination: A viable solution for a potential market. *Desalination.* 2018;435:60-9.
- [61] Tchobanoglous G, Burton F, Stensel H. *Wastewater engineering: treatment and reuse.* 4th ed. Boston: McGraw-Hill; 2003. 1197p.
- [62] Kabra K, Chaudhary R, Sawhney R. Treatment of hazardous organic and inorganic compounds through aqueous-phase photocatalysis: A review. *Ind Eng Chem Res.* 2004;43(24):7683-96.
- [63] Malato S, Fernández-Ibáñez P, Maldonado M, Blanco J, Gernjak W. Decontamination and disinfection of water by solar photocatalysis: Recent overview and trends. *Catal Today.* 2009;147(1):1–59.
- [64] Blanco J, Malato S, Fernández-Ibáñez P, Alarcón D, Gernjak W, Maldonado M. Review of feasible solar energy applications to water processes. *Renew Sust Energy Rev.* 2009;13(6-7):1437–45.
- [65] Malato S, Blanco J, Maldonado M, Fernández-Ibáñez P, Alarcón D, Collares M, et al. Engineering of solar photocatalysis collectors. *Sol Energ.* 2004;77(5):513-24.
- [66] Zhang Y, Sivakumar M, Yang S, Enever K, Ramezani-pour M. Application of solar energy in water treatment process: A review. *Desalination.* 2018;428:116-145.
- [67] Tallent RJ, Oman H. Solar-cell performance with concentrated sunlight. *Trans AIEE Part II.* 1962;81(1):30-3.
- [68] Green M, Emery K, Hishikawa Y, Warta W, Dunlop E. Solar cell efficiency tables (version 45). *Prog Photovoltaics.* 2015;23(1):1-9.

- [69] Karathanassis I, Papanicolaou E, Belessiotis V, Bergeles G. Design and experimental evaluation of a parabolic-trough concentrating photovoltaic/thermal (CPVT) system with high-efficiency cooling. *Renew Energy*. 2017;101:467–83.
- [70] Jiang S, Hu P, Mo S, Chen Z. Optical modeling for a two-stage parabolic trough concentrating photovoltaic/thermal system using spectral beam splitting technology. *Sol Energy Mater Sol Cells*. 2010;94(10):1686–96.
- [71] Li M, Ji X, Li G, Wei S, Li Y, Shi F. Performance study of solar cell arrays based on a trough concentrating photovoltaic/thermal system. *Appl Energy*. 2011;88(9):3218–27.
- [72] Li M, Li G, Ji X, Yin F, Xu L. The performance analysis of the trough concentrating solar photovoltaic/thermal system. *Energy Convers Manag*. 2011;52(6):2378–83.
- [73] Quaia S, Lughì V, Giacalone M, Vinzi G. Technical-economic evaluation of a combined heat and power solar (CHAPS) generator based on concentrated photovoltaics. *International Symposium on Power Electronics Power Electronics, Electrical Drives, Automation and Motion*. 2012.
- [74] Yazdanifard F, Ebrahimnia-Bajestan E, Ameri M. Performance of a parabolic trough concentrating photovoltaic/thermal system: Effects of flow regime, design parameters, and using nanofluids. *Energy Conver Manag*. 2017;148:1265–77.
- [75] Mendelsohn M, Lowder T, Canavan B. Utility-scale concentrating solar power and photovoltaics projects: A technology and market overview. Golden (CO): NREL; 2012.65p.Report No.: NREL/TP-6A20-51137.
- [76] Burkholder F, Kutscher C. Heat-loss testing of Solel’s UVAC3 parabolic trough receiver. Golden (CO, USA): NREL; 2008. 19 p. Report No.: NREL/TP-550-42394.
- [77] Pempeintner J, Anger M, Lichtenthäler N, Ant P, Happich C, Thoss J. Measurement of parabolic trough receiver thermal loss power and relative optical efficiency under solar simulator light: Test report. Köln (GER): DLR Quarz; 2012. 30 p.
- [78] Burkholder F, Kutscher C. Heat loss testing of Schott’s 2008 PTR70 parabolic trough receiver. Golden (CO, USA): NREL; 2009. 58 p. Report No.: NREL/TP-550-45633.
- [79] Janotte N, Lüpfer E, Pottler K, Schmitz M. Full parabolic trough qualification from prototype to demonstration loop. *AIP Conference Proceedings*. 2017.
- [80] Janotte N, Feckler G, Kötter J, Decker S, Herrmann U, Schmitz M, et.al. Dynamic performance evaluation of the HelioTrough® collector demonstration loop towards a new benchmark in parabolic trough qualification. *Energ Proc*. 2014;49:109-17.
- [81] European Commission. EuroTrough II: Extension, test and qualification of EUROTRPUGH from 4 to 6 segments at Plataforma Solar de Almería [pdf on internet].

2004 [cited 2018 Mar 08]. Available from: https://cordis.europa.eu/docs/publications/6668/66682891-6_en.pdf.

[82] Fernández-García A, Zarza E, Pérez M, Valenzuela L, Rojas E, Valcárcel E. Experimental assessment of a small-sized parabolic trough collector: CAPSOL Project. Proceedings of EuroSun 2010; 2010.

[83] Moss T, Brosseau D. Final test results for the Schott HCE on a LS-2 collector. Albuquerque (NM, USA): SANDIA; 2005. 22p. Report No.: SAND2005-4034.

[84] Dudley V, Kolb G, Sloan M, Kearney D. SEGS LS2 solar collector: Test results. Springfield (VA, USA): SANDIA; 1994. 140p. Report No.: SAND94-1884.

[85] Dudley V, Evans L, Matthews C. Test results: Industrial solar technology parabolic trough solar collector. Albuquerque (NM, USA): SANDIA; 1995. 140p. Report No.:

[86] Brooks MJ. Performance of a parabolic trough solar collector [master's thesis]. Stellenbosch (ZA): University of Stellenbosch; 2005. 174 p.

[87] Valenzuela L, López-Martín R, Zarza E. Optical and thermal performance of large-size parabolic-trough solar collectors from outdoor experiments: A test method and a case study. *Energ*. 2014;70:456–64.

[88] Sallaberry F, Valenzuela L, Palacin Luis. On-site parabolic-trough collector testing in solar thermal power plants: Experimental validation of a new approach developed for the IEC 62862-3-2 standard. *Sol Energ*. 2017;155:398-409.

[89] McMahan A, White D, Gee R, Vijoer N. Field performance validation of an advanced utility-scale parabolic trough concentrator. Proceeding of SolarPACES Conference 2010. 2010.

[90] Hoste G, Schuknecht N. Thermal efficiency analysis of SkyFuel's advanced, large-aperture parabolic trough collector. *Energ Proc*. 2015;69:96-105.

[91] Balghouthi M, Bel Hadj Ali A Eddine Trabelsi S, Guizani A. Optical and thermal evaluations of a medium temperature parabolic trough solar collector used in a cooling installation. *Energ Conv Manag*. 2014;86:1134-46.

[92] Janotte N, Meiser S, Krüger D, Lüpfer E, Pitz-Paal R, Fischer S, et. al. Quasy-dynamic analysis of thermal performance of parabolic trough collectors. Proceedings of SolarPACES 2009. 2009.

[93] Alfellag M. Modeling and experimental investigation of parabolic trough solar collector [master's thesis]. Daytona Beach (FL, USA): Embry-Riddle Aeronautical University; 2014. 112 p.

- [94] Arancibia-Bulnes C, Peña-Cruz M, Mutuberría A, Díaz-Urbe R, Sánchez-González M. A survey of methods for the evaluation of reflective solar concentration optics. *Renew Sust Energ Rev.* 2017;69:673-84.
- [95] Kalogirou. *Solar Energy Engineering – Processes and Systems.* Elsevier; 2014, pp. 68-69.
- [96] ASHRAE. Standard 93: Methods of testing to determine the thermal performance of solar collectors. 2010.
- [97] ISO. Standard 9806: Solar energy - Solar thermal collector – Test methods. 2013.
- [98] ASTM. Standard E-905. Standard test method for determining thermal performance of tracking concentrating solar collectors. 2013.
- [99] QAISt. A guide to the standard EN 12975 [pdf on internet]. 2012 [cited 2018 Mar 11]. Available from: http://www.estif.org/fileadmin/estif/content/projects/QAISt/QAISt_results/QAISt%20D2.3%20Guide%20to%20EN%2012975.pdf.
- [100] FSEC. Standard 102: Test methods and minimum standards for certifying solar thermal collectors. 2010.
- [101] SRCC. Standard 600: Minimum standard for solar thermal concentrating collectors. 2013.

Chapter 3 Description of modeling

Abstract

This chapter describes the thermal-hydraulic modeling with the detail of all the heat transfer and fluid mechanics equations involved into the solar-energy-to-heat conversion. One-phase and two-phase internal forced convection are explained in detail, also other heat transfer phenomena (radiation and other types of convection). There is also an explanation of how to use the developed code (software and platform used). All the processes of entering data, processing, and obtaining results are described.

3.1 Thermo-hydraulic model

The mathematical model is based on a steady-state one-dimensional heat transfer analysis with single-phase and two-phase flow as internal flow convection. The boundaries of the analysis are the Heat Transfer Fluid (HTF) and the surrounding air of the receiver, as shown in Figures 3.1, so the pipe and the cover glass (if used) are considered into thermo-hydraulic analysis. A thermal resistance model describes the heat transfer phenomena considering conduction, convection and radiation among all the surfaces (internal and external, pipe and cover glass if used); where an energy balance is carried out to obtain thermal performance. This model is a modified version of the Forristal model [1], where there was added the two-phase flow phenomena and thermo-hydraulic analysis in interconnecting piping between adjacent solar collectors.

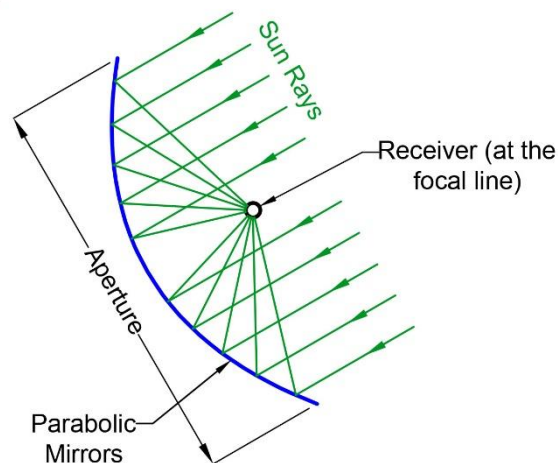


Fig. 3.1 - Boundary of the analysis of the collector

The model divides the system into equal-sized sections where the energy balance is carried out in each of them. The HTF outlet conditions of one section are the same as the inlet conditions of the next section, unless there is an interconnecting piping between both sections. Similar to sections, the hydraulic and heat transfer phenomena in interconnecting piping are estimated by a simplified thermal resistance model where it is considered that the heat is lost (see Section 3.1.2). Both thermal resistance models (receiver and interconnecting piping) estimates convective heat transfer coefficient based

on experimental correlations depending on the type of convection and flow. Engineering Equation Solver [2] was selected as simulation tool due to its large data base of thermo-physical material properties and its simplicity in programming and solving complex non-linear equation systems. The limitation in number of sections and interconnections considered into the analysis depends on the maximum number of equations that the software can solve (see Section 3.3).

3.1.1 Energy Balance Equations for Receiver

Thermal resistance model of the receiver is composed by 8 nodes (as described in Figure 3.2, if cover glass used) where the temperatures of 5 nodes are unknown: inlet and outlet surfaces of cover glass and pipe, and HTF. Equations (3.1) – (3.6) describe energy balance of radial heat flows, and (3.5) describes the energy balance of the fluid. Most of receivers used are glass covered, but in case it is not, there is an option that can analyze a not-glass-covered receiver. In this case, thermal model is similar, but it would have 6 nodes where there are 3 unknown temperatures.

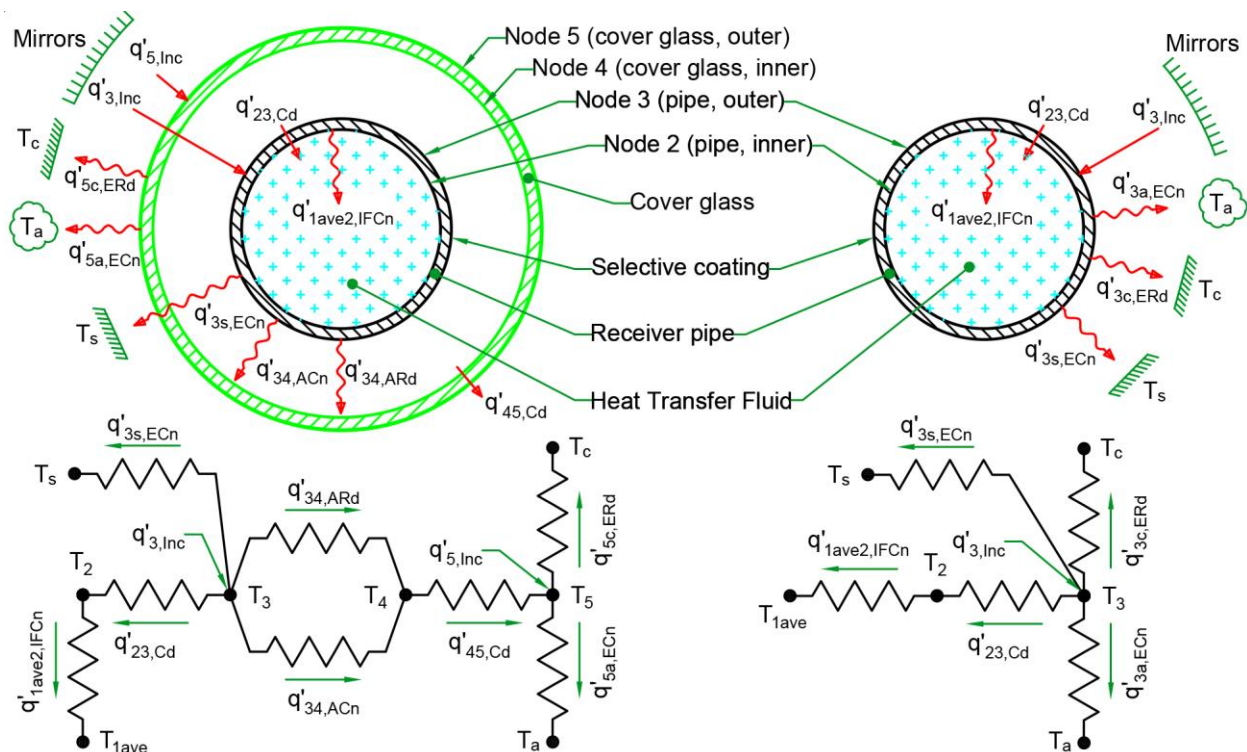


Fig. 3.2 - Thermal resistance model for the receiver

Heat transfer flows through nodes of thermal resistance model can be described with a specific type of heat transfer phenomena. Table 3.1 shows all modes considered in the model and notation used in Figure 3.2. Table 3.1 also describes a classification of sub-modes for each heat transfer flow, and a reference of section where it is discussed in detail. Assumptions, correlations, and conditions of validity are also described in their respective sections. Incident radiation (reflected from mirrors) are considered as source of energy in thermal resistance model.

Table 3.1 – Heat transfer modes in thermal resistance model

Heat transfer mode	Notation	Sub-mode (See Section)
Incident radiation	Inc	N.A.
Conduction	Cd	N.A.
Internal Forced Convection	IFCn	- Single-phase (3.1.3) - Two-phase (3.1.4) - Nanofluids (3.1.6)
Annular Convection	ACn	- Non-evacuated (3.1.7.1) - Evacuated (3.1.7.1)
Annular Radiation	ARd	N.A. (3.1.7.5)
External Convection	ECn	- Natural (3.1.7.2) - Cross-flow forced (3.1.7.3) - Extended surfaces (3.1.7.4)
External Radiation	ERd	N.A. (3.1.7.6)

N.A. : Not applicable

As shown in Figure 3.3, the income heat flow is the internal convective heat flow inside the pipe, which is the heat gain of the section. Outlet conditions are obtained based on inlet conditions (input data), mean bulk HTF conditions, and energy balance. Heat gain and pressure drop are function of the mean bulk HTF conditions (temperature, pressure and quality) and flow regime. Equation (3.6) describes the thermal efficiency of the section analyzed, which is the ratio between heat gain and incoming energy that reaches the receiver.

In Equation (3.5), $\Delta\left(\frac{\beta V^2}{2}\right)$ represents the change in mechanical energy of the flow. This change is based on a correction factor β , which is a function of the properties at both inlet and outlet conditions. The impact of this change in sub-cooled liquids is insignificant, but it becomes more important in two-phase and dry-steam flows. Equations (3.7) – (3.9) describe the calculation of change in mechanical energy. Correction factor and mean velocity in two-phase flow where obtained by modeling the flow as non-mixed uniform flow of dry-steam and liquid-water (uniform-velocity two-layers flow).

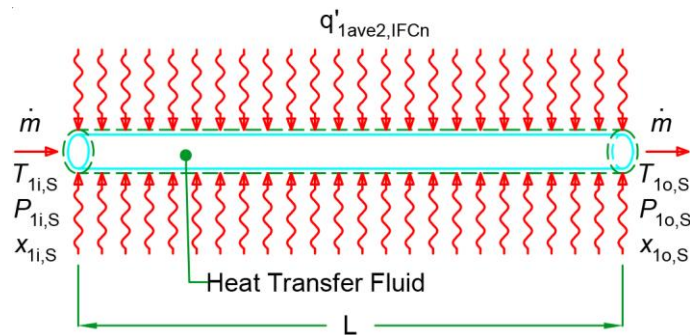


Fig. 3.3 - Energy balance around the fluid

$$\text{Node 2 (inner side of pipe)} : q'_{1ave2,IFCn} = q'_{23,Cd} \quad (3.1)$$

$$\text{Node 3 (outer side of pipe)} : q'_{3,Inc} = q'_{23,Cd} + q'_{34,ACn} + q'_{34,ARd} + q'_{3s,ECn} \quad (3.2)$$

$$\text{Node 4 (inner side of cover glass)} : q'_{34,ACn} + q'_{34,ARd} = q'_{45,Cd} \quad (3.3)$$

$$\text{Node 5 (outer side of cover glass)} : q'_{45,Cd} + q'_{5,Inc} = q'_{5a,ECn} + q'_{5c,ERd} \quad (3.4)$$

$$\Delta h_s = \frac{q'_{1ave2,IFCn} L_s}{\dot{m}} - \Delta \left(\frac{\beta V^2}{2} \right) - g \Delta z \quad (3.5)$$

$$\eta = \frac{q'_{1ave2,IFCn}}{IWK} \quad (3.6)$$

$$\Delta \left(\frac{\beta V^2}{2} \right) = \frac{\beta_{out} V_{out}^2}{2} - \frac{\beta_{in} V_{in}^2}{2} \quad (3.7)$$

$$\beta = \begin{cases} 1 ; \text{ single - phase flow} \\ \frac{V_l^3 + (V_v^3 - V_l^3)\varepsilon}{[V_l + (V_v - V_l)\varepsilon]^3} ; \text{ two - phase flow} \end{cases} \quad (3.8)$$

$$V = \begin{cases} \frac{4\dot{m}}{\rho_{1ave}\pi D_2^2} ; \text{ single - phase flow} \\ V_l + (V_v - V_l)\varepsilon ; \text{ two - phase flow} \end{cases} \quad (3.9)$$

Equations (3.10) – (3.19) describe the radial heat flows of the thermal resistance model. It is noticed that the heat gain, described by (3.10), depends on Nusselt number for internal forced convection, which also depends on the type of flow (single-phase or two-phase). Heat transfer and pressure drop calculation for both single-phase and two-phase flow are described in Sections 3.1.3 and 3.1.4 respectively. Formulation of other heat transfer mechanisms are described in detail in Section 3.1.7.

$$q'_{1ave2,IFCn} = \left(Nu \frac{k_{1ave2}}{D_2} \right) \pi D_2 \Delta T_{1ave2} ; Nu = \text{Internal forced convection} \quad (3.10)$$

$$q'_{23,Cd} = 2\pi k_{23} \frac{\Delta T_{23}}{\ln \frac{D_3}{D_2}} \quad (3.11)$$

$$q'_{34,ACn} = q' \text{ by natural annular convection} \quad (3.12)$$

$$q'_{34,ARd} = q' \text{ by radiation in annular region} \quad (3.13)$$

$$q'_{3s,ECn} = q' \text{ by external convection in extended surfaces} \quad (3.14)$$

$$q'_{45,Cd} = 2\pi k_{45} \frac{\Delta T_{45}}{\ln \frac{D_5}{D_4}} \quad (3.15)$$

$$q'_{5a,ECn} = \left(Nu \frac{k_{5a}}{D_5} \right) \pi D_5 \Delta T_{5a} \quad (3.16)$$

$$Nu = \begin{cases} Nu \text{ by natural external convection if } v < 0.1\text{m/s} \\ Nu \text{ by cross flow external forced convection if } v > 0.1\text{m/s} \end{cases}$$

$$q'_{5c,ERd} = q' \text{ by external radiation} \quad (3.17)$$

$$q'_{3,Inc} = \tau_{45}\eta_{op}\alpha_3IW \quad (3.18)$$

$$q'_{5,Inc} = \eta_{op}\alpha_5IW \quad (3.19)$$

3.1.2 Energy Balance Equations for Interconnecting Piping

Thermal analysis for interconnecting piping is similar than for receivers. Figure 3.4 shows a six-node thermal resistance model for interconnections, where four temperatures are unknown. Equations (3.20) – (3.24) describe the energy balance in thermal resistance circuit and (3.23) is the energy balance of the HTF. Figure 3.7 shows the energy balance in the interconnection. It is noticed that the temperature of the HTF is higher than ambient temperature, so heat flows from the fluid to the ambience as a loss ($q'_{1ave2,conv}$). This heat loss is obtained using single-phase or two-phase internal forced convection approach, as described in detail in Sections 3.1.3 and 3.1.4. The principal characteristic of this analysis is that geometric length of interconnections does not match with hydraulic length, so pressure drop is function of hydraulic length of interconnections. Equation (3.5) is quite different to (3.23) principally because of the consideration in change of enthalpy and the geometry of the sections. The enthalpy increases in receivers (heat gain), while is decreases in interconnecting piping (heat losses). Change in mechanical energy ($\Delta(\beta V^2/2)$) is obtained by the same method explained in Section 3.1.1.

$$\text{Node 2 (inner side of pipe)} : q'_{1ave2,IFCn} = q'_{23,Cd} \quad (3.20)$$

$$\text{Node 3 (outer side of pipe)} : q'_{23,Cd} = q'_{34,Cd} \quad (3.21)$$

$$\text{Node 4 (outer side of insulation)} : q'_{34,Cd} + I_b\pi D_4 = q'_{4a,ECn} + q'_{4c,ERd} \quad (3.22)$$

$$\Delta h_l = \frac{q'_{1ave2,IFCn}L_{G,I}}{\dot{m}} + \Delta\left(\frac{\beta V^2}{2}\right) + g\Delta z ; \Delta P_l = f(L_{H,I}) \quad (3.23)$$

$$L_{G,I} = L_{pipe} ; L_{H,I} = L_{pipe} + L_{eq,acc} \quad (3.24)$$

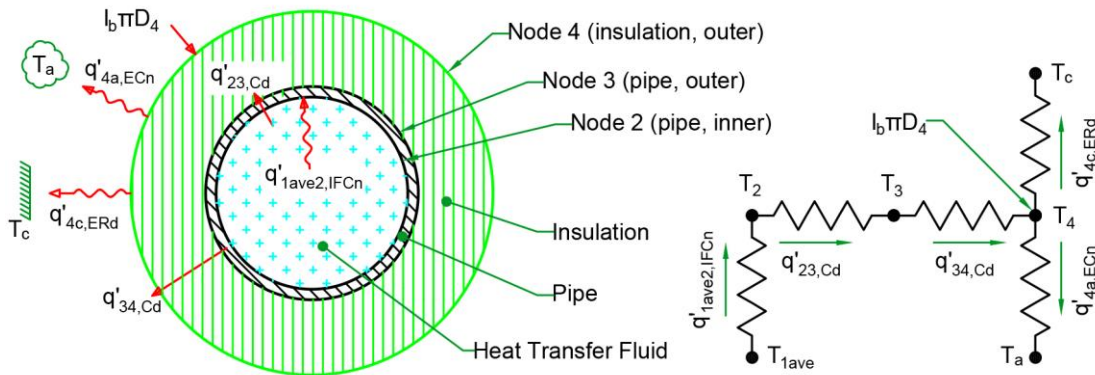


Fig. 3.4 - Thermal resistance model for interconnecting piping

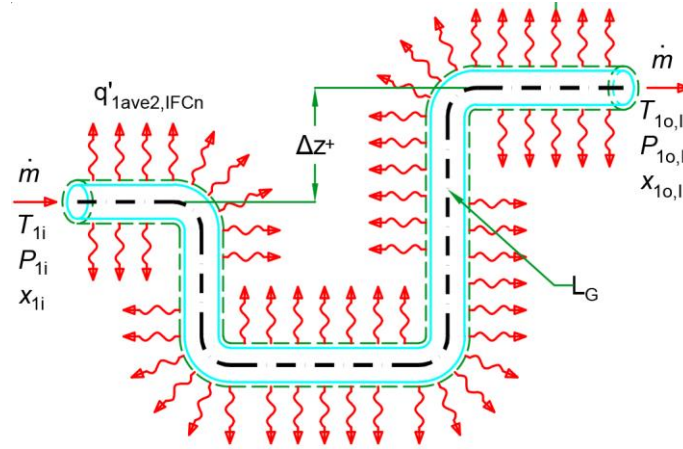


Fig. 3.5 - Energy balance around the interconnecting piping

3.1.3 Single-phase Internal Forced Convection

Sub-cooled liquid and dry steam are considered as single-phase fluids. Heat transfer and hydraulic analysis are considered as fully-developed flows with constant heat flux boundary conditions, and they are functions of the Reynolds number. Three regimes are considered: laminar, transitional and turbulent flow. Equations (3.25) – (3.27) describes the heat transfer analysis. All thermophysical properties are calculated at mean bulk temperature of the fluid, except Pr_w which is obtained at the internal wall temperature of the pipe. The Prandtl ratio corrects for the temperature dependency of fluid properties [3].

$$Nu = 4.36 \left(\frac{Pr}{Pr_w} \right)^{0.11} ; Re < 1800 \quad (3.25)$$

$$Nu = \sqrt[10]{4.364^{10} + \left(\frac{e^{\left(\frac{2200-Re}{365}\right)} + \left(6.3 + \frac{0.079RePr\sqrt{f/2}}{(1+Pr^{4/5})^{5/6}} \right)^{-2} \right)^{-5}} \left(\frac{Pr}{Pr_w} \right)^{0.11} \quad (3.26)$$

$$1800 < Re < 4000$$

$$Nu = \frac{fRePr}{2 \left(1.07 + \frac{900}{Re} - \frac{0.63}{1+10Pr} + 12.7(Pr^{2/3} - 1)\sqrt{\frac{f}{2}} \right)} \left(\frac{Pr}{Pr_w} \right)^{0.11} \quad (3.27)$$

$$4000 < Re < 10^7$$

For laminar flow, Nusselt number is constant and considered as constant heat flux in the surface. For transitional flow, Churchill's correlation was selected. Finally, Petukov-Kirilov-Popov correlation was selected for turbulent flow, which is quite similar to Gnielinsky's correlation. These correlations were selected because they have a good

agreement with experimental data [3] and a quasi-continuity in regime changes all over the range of Reynolds number, as shown in Figure 3.6.

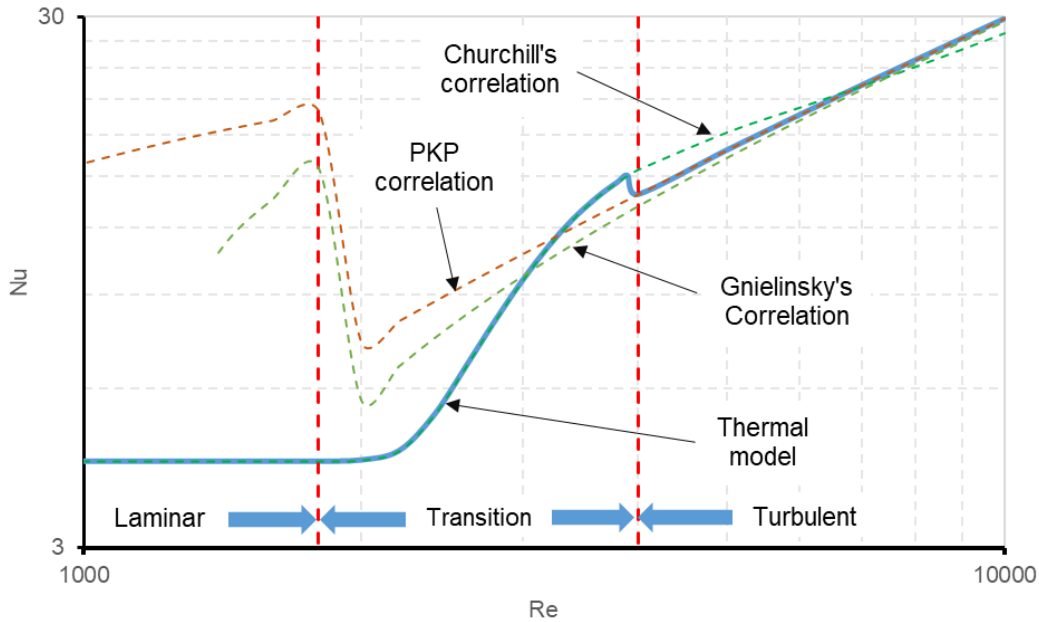


Fig. 3.6 - Nu vs. Re for single-phase internal forced convection ($Pr=0.7$, $Pr/Pr_w=1$).

Equation (3.28) represents the pressure drop in single-phase flow. Applying the same approach used before, (3.29) to (3.31) describes the mathematical model for Fanning friction factor. Explicit correlations for smooth pipes are used in order to minimize computational time and cost. A correlation developed by Churchill was selected for transitional flow, and a Colebrook's correlation for turbulent flow. Figure 3.7 shows the mathematical model for friction factor. Notice that the friction factor is continuous all over the range of Reynolds numbers, and also present a low error compared to implicit Colebrook-White correlation used in the literature.

$$\Delta P = 2f \frac{L}{D} \rho V^2 \quad (3.28)$$

$$f = 16/Re ; Re < 1800 \quad (3.29)$$

$$f = 2 \left[\left(\frac{8}{Re} \right)^{12} + \left[\left(-2.457 \ln \left(\frac{7}{Re} \right)^{0.9} \right)^{16} + \left(\frac{37530}{Re} \right)^{16} \right]^{3/2} \right]^{1/12} \quad (3.30)$$

$$1800 < Re < 4000$$

$$f = \left(1.5635 \ln \frac{Re}{7} \right)^{-2} ; 4000 < Re < 10^7 \quad (3.31)$$

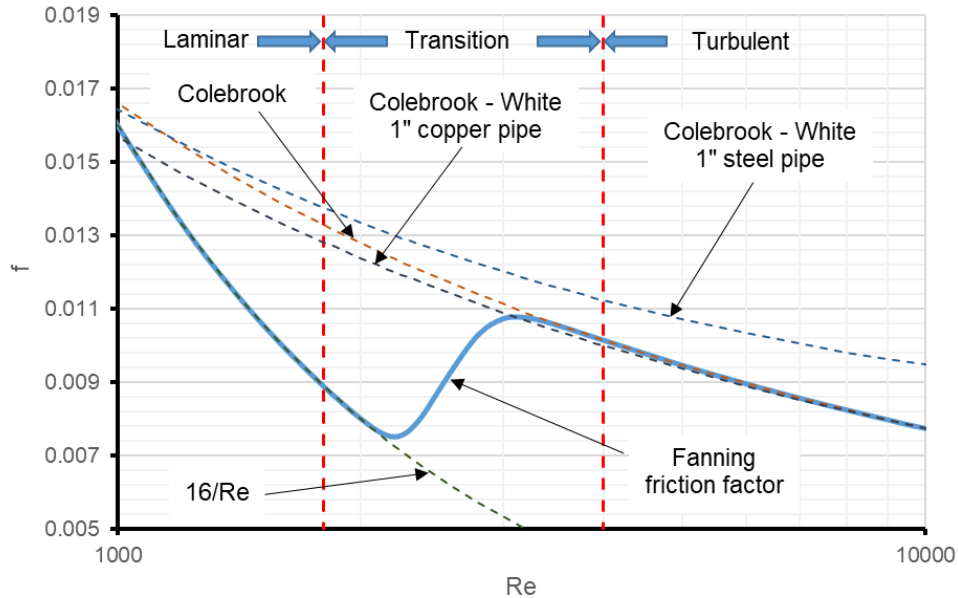


Fig. 3.7 - f vs. Re for single-phase flow

3.1.4 Two-phase Internal Forced Convection

Two-phase flow occurs at the boiling section of the system, where there is wet steam. Wojtan et al. [4,5] developed a heat transfer model for two-phase flow based on flow boiling data of refrigerants. This model considers horizontal tubes with evaporating diabatic flow, and it uses a flow pattern map (Figure 3.8) to locate the flow regime as a function of mass flux velocity G and vapor quality x . The methodology to solve two-phase flow consists on two steps: locating flow pattern with a given G and x , and calculating heat transfer/pressure drop using equations for resulting flow pattern.

Flow patterns can be classified as “separated flows”, dryout flow, and mist flow. A separated flow is when liquid and gas phases are separated by an interface. Figure 3.9 shows a graphical description of some flow patterns in axial and cross section of the pipe. The behavior of each flow pattern considered in the model as described as follow:

- **Stratified:** It occurs at low G . Gas and liquid phases are completely separated by an undisturbed horizontal interface. The gas phase goes up due to its buoyancy.
- **Stratified-wavy:** It occurs when there are notable waves on the interface of a stratified flow traveling in the flow direction. The crests of the waves do not reach the top of the pipe.
- **Slug:** When G increases, waves at the interface becomes larger until the crest of waves are similar to the height of gas phase. The gas phase can be described as bubbles with large amplitude.
- **Slug + stratified-wavy:** It is a combination of the slug and stratified-wavy flow patterns (both short and large waves at interface appear).
- **Intermittent:** When the amplitude of waves in the interface becomes larger compared to slug flow, the liquid phase is capable to “wash” the top of the pipe. The gas phase becomes “small-amplitude bubbles”.

- **Annular:** The liquid phase forms film all around the surface of the pipe, and gas flows in its core. The interface may be disturbed with small waves and the gas phase may have dispersed droplets. Bubbles may appear in the interface.
- **Dryout:** When liquid phase starts evaporating or converting into small dispersed droplets.
- **Mist:** All the liquid phase is converted into quasi-continuous dispersed droplets in gas phase.

Void fraction ε is the fraction of cross-area that is occupied by the vapor phase. Equation (3.33) determines angle of stratified flow (angle covered by liquid phase). Equations (3.34) – (3.37) describe transitional limits of flow patterns (G_s : stratified flow, G_w : wavy flow, G_d : dryout flow, G_m : mist flow). x_{IA} is the steam quality where occurs transition of intermittent and annular flows. x_{di} and x_{de} are the steam qualities where occurs inlet and exit (respectively) of dryout flow at a given G . Dryout effect does not occurs at very low mass flux velocities. This limit is determined by x_s . Solving these equations and using the algorithm described in Figure 3.10 simultaneously, flow pattern with a given G and x is determined. Equation (3.39) is solved iteratively using fixed-point method, taking x_{IA} as initial value.

$$\varepsilon(x) = \frac{x}{\rho_v \left[(1.12 - 0.12x) \left(\frac{x}{\rho_v} + \frac{1-x}{\rho_l} \right) + \frac{1.18(1-x)[g\Lambda(\rho_l - \rho_v)]^{0.25}}{G\rho_l^{0.5}} \right]} \quad (3.32)$$

$$\theta_s = 2\pi - 2 \left\{ \pi(1 - \varepsilon(x)) + \sqrt[3]{\frac{3\pi}{2} [2\varepsilon(x) - 1 + \sqrt[3]{1 - \varepsilon(x)} - \sqrt[3]{\varepsilon(x)}]} \right. \\ \left. - \frac{[3\varepsilon^2(x) - 2\varepsilon^3(x) - \varepsilon(x)][8\varepsilon^2(x) - 8\varepsilon(x) + 5]}{200} \right\} \quad (3.33)$$

$$G_s(x) = \sqrt[3]{\frac{226.3^2 g A_{LD} A_{VD}^2 \rho_v (\rho_l - \rho_v) \mu_l}{x^2 (1-x) \pi^3}}; A_{LD} = \frac{\pi}{4} (1 - \varepsilon(x)); A_{LD} = \frac{\pi}{4} \varepsilon(x) \quad (3.34)$$

$$G_w(x) = \sqrt{\frac{16gA_{VD}^3 D_2 \rho_l \rho_v}{(\pi x)^2 \sqrt{1 - (2h_{LD} - 1)^2}} \left(\frac{\pi^2 Fr_l}{25h_{LD}^2 We_l} + 1 \right)} + G_{w0}; h_{LD} \\ = 0.5 - 0.5 \cos \left(\pi - \frac{\theta_s}{2} \right) \quad (3.35)$$

$$G_d(x) = \sqrt{\frac{\rho_v \Lambda}{D_2}} \left[\frac{1}{0.235} \left(\ln \frac{0.9756}{x} \right) \left(\frac{g D_2^2 (\rho_l - \rho_v)}{\Lambda} \right)^{0.37} \left(\frac{\rho_l}{\rho_v} \right)^{0.25} \left(\frac{q_{crit}}{q} \right)^{0.7} \right]^{0.926} \quad (3.36)$$

$$G_m(x) = \sqrt{\frac{\rho_v \Lambda}{D_2}} \left[\frac{1}{0.0058} \left(\ln \frac{1.0786}{x} \right) \left(\frac{g D_2^2 (\rho_l - \rho_v)}{\Lambda} \right)^{0.15} \left(\frac{\rho_v}{\rho_l} \right)^{0.09} \left(\frac{q_{crit}}{q} \right)^{0.27} \right]^{0.943} \quad (3.37)$$

$$x_{IA} = \left[0.34^{1/0.875} \left(\frac{\rho_l}{\rho_v} \right)^{1/1.75} \left(\frac{\mu_v}{\mu_l} \right)^{1/7} + 1 \right]^{-1} \quad (3.38)$$

$$G_s(x_s) = G_d(x_s) \quad (3.39)$$

$$x_{di} = 0.58 \exp \left(0.52 - 0.235 W e_v^{0.17} F r_v^{0.37} \left(\frac{\rho_v}{\rho_l} \right)^{0.25} \left(\frac{q}{q_{crit}} \right)^{0.70} \right) \quad (3.40)$$

$$x_{de} = 0.61 \exp \left(0.57 - 0.0058 W e_v^{0.38} F r_v^{0.15} \left(\frac{\rho_v}{\rho_l} \right)^{-0.09} \left(\frac{q}{q_{crit}} \right)^{0.27} \right) \quad (3.41)$$

Equations (3.42) – (3.46) represents the heat transfer coefficient. Equation (3.42) is used for all flow patterns except for dryout and mist flows, and it is function of vapor convection (h_v) and wet convection (h_w) heat transfer coefficients. Equations (3.43) and (3.44) are used for dryout and mist flows respectively. The angle θ_d is the dry angle of tube perimeter, and it is obtained according to (3.47) and Table 3.2.

$$h_{TPH}(x) = \frac{\theta_d(x)h_v + (2\pi - \theta_d(x))h_w}{2\pi} \quad (3.42)$$

$$h_d = h_{TPH}(x_{di}) - \frac{x - x_{di}}{x_{de} - x_{di}} [h_{TPH}(x_{di}) - h_m(x_{de})] \quad (3.43)$$

$$h_m(x) = 0.0117 [Re_H(x)]^{0.79} Pr_V^{1.06} \left[1 - 0.1 \left((\rho_l - \rho_v) \frac{(1-x)}{\rho_v} \right)^{0.4} \right]^{-1.83} \frac{k_V}{D_2} \quad (3.44)$$

$$h_v = 0.023 Re_v^{0.8} Pr_v^{0.4} \frac{k_v}{D_2} \quad (3.45)$$

$$h_w = \sqrt[3]{ \left(0.0133 Re_\delta^{0.69} Pr_l^{0.4} \frac{k_l}{\delta} \right)^3 + \left(C_w p_r^{0.12} \frac{q^{0.67}}{(-\log(p_r))^{0.55} M^{0.5}} \right)^3 } \quad (3.46)$$

$$\theta_d(x) = \begin{cases} 0 ; \text{ Slug, intermittent and annular regimes} \\ \left(\frac{x}{x_{IA}} \right)^a \left(\frac{G_w(x) - G}{G_w(x) - G_s(x)} \right)^b \theta_s ; \text{ for other regimes} \end{cases} \quad (3.47)$$

Table 3.2 - Constants for (3.47)

Regime	a	b
Stratified	0	0
Slug + Stratified wavy	1	0.61
Stratified wavy	0	0.61

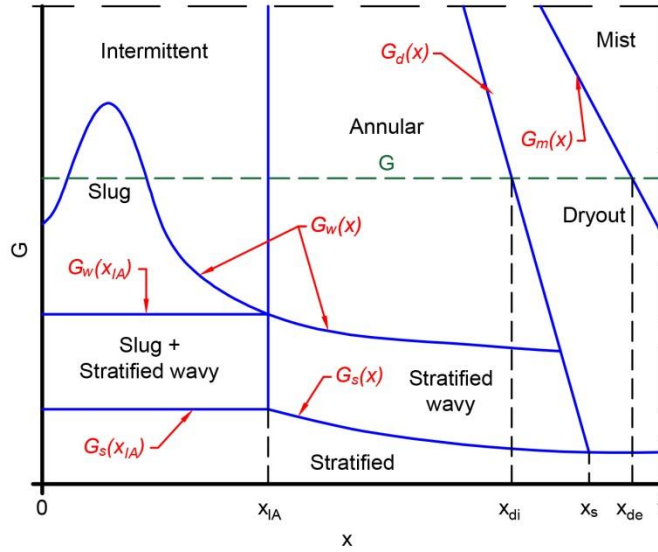


Fig. 3.8 - Typical flow pattern map for two-phase flow

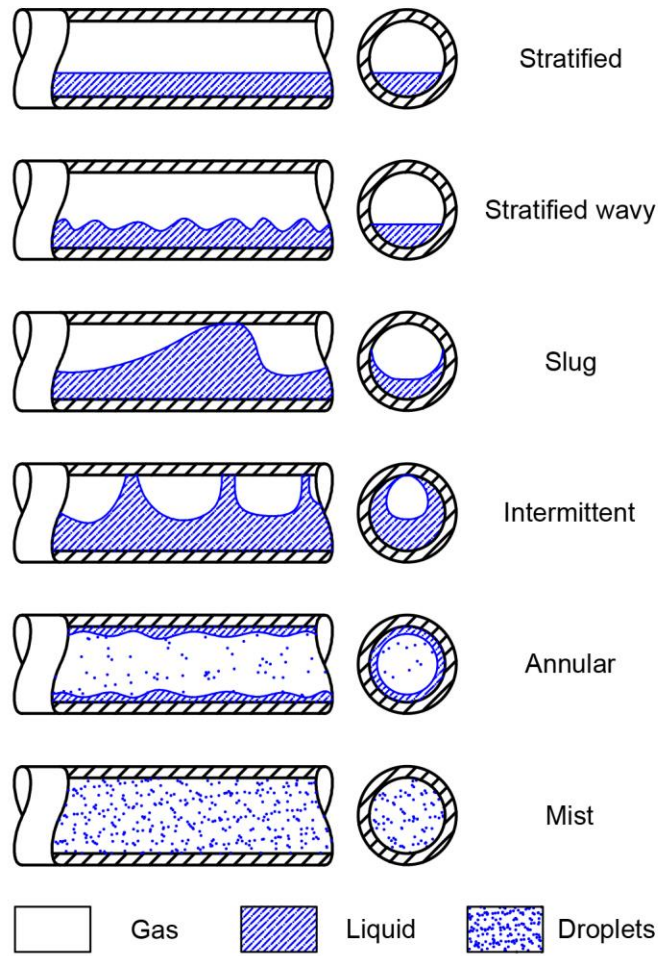


Fig. 3.9 – Behavior of flow patterns

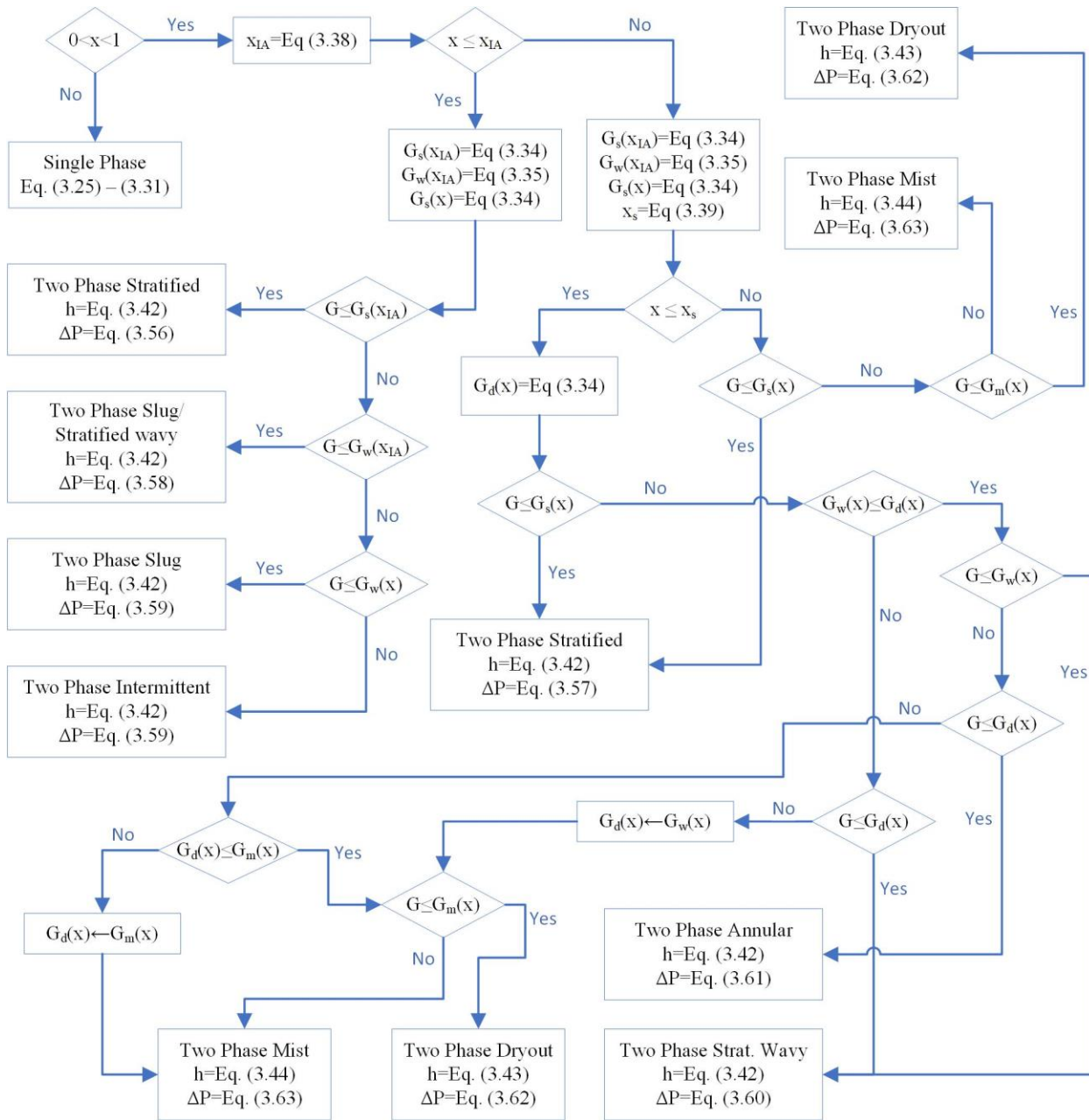


Fig. 3.10 - Flowchart algorithm

For hydraulic behavior in two-phase flow, the model developed by Quibén and Thome [6] is used. This model uses the same flow pattern maps as Wojtan et al. The accuracy of this model is within $\pm 30\%$ of precision of around 83% of the validating experimental data, taking into account that the validation of the model was made with a wide range of conditions (fluids, pipe diameters, mass flows, heat fluxes) [6]. Equations (3.48) – (3.55) and Table 3.3 describes the mathematical model for pressure drop depending on flow pattern regime. Pressure drop ΔP_{LO} is the pressure drop as saturated liquid, and it is calculated using (3.28).

$$V_l = \frac{G(1-x)}{\rho_l(1-\varepsilon)} ; V_v = \frac{Gx}{\rho_v\varepsilon} \quad (3.48)$$

$$f_{TPH,S} = \frac{\theta_s}{2\pi} f_G + \left(1 - \frac{\theta_s}{2\pi}\right) f_{TPH,A} \quad (3.49)$$

$$f_{TPH,SW} = \frac{\theta_d(x)}{2\pi} f_G + \left(1 - \frac{\theta_d(x)}{2\pi}\right) f_{TPH,A} \quad (3.50)$$

$$f_G = 0.079 \left(\frac{\mu_v \varepsilon(x)}{Gx D_2} \right)^{0.25} \quad (3.51)$$

$$f_{TPH,A} = 0.67 \left(\frac{\delta}{D_2} \right)^{1.2} \left(\frac{\Lambda}{(\rho_l - \rho_v) g \delta^2} \right)^{0.4} \left(\frac{\mu_v}{\mu_l} \right)^{0.08} We_l^{-0.034} \quad (3.52)$$

$$f_H = 0.079 \left(\frac{x\mu_v + (1-x)\mu_l}{GD_2} \right)^{0.25} \quad (3.53)$$

$$\rho_H = \rho_l \left(1 - \frac{x\rho_l}{x(\rho_l - \rho_v) + \rho_v} \right) + \frac{x\rho_l\rho_v}{x(\rho_l - \rho_v) + \rho_v} \quad (3.54)$$

$$\delta = \begin{cases} \frac{D_2}{2} ; \theta_d(x) > 2\pi\varepsilon(x) \\ \frac{D_2}{2} - \sqrt{\left(\frac{D_2}{2}\right)^2 - \frac{\pi D_2^2(1-\varepsilon(x))}{4\pi - 2\theta_d(x)}} ; \theta_d \leq 2\pi\varepsilon(x) \end{cases} \quad (3.55)$$

Table 3.3 - Equations for pressure drop modeling

Flow pattern	Special condition	Model	Eq.
Stratified	$x < x_{IA}$	$\Delta P_{S,1} = \Delta P_{LO} \left(1 - \frac{\varepsilon(x)}{\varepsilon(x_{IA})} \right)^{0.25} + \Delta P_{S,2} \left(\frac{\varepsilon(x)}{\varepsilon(x_{IA})} \right)^{0.25}$	(3.56)
	$x \geq x_{IA}$	$\Delta P_{S,2} = 4f_{TPH,S} \frac{L\rho_v V_v^2}{2D_2}$	(3.57)
Slug stratified wavy	+	$\Delta P = \Delta P_{LO} \left(1 - \frac{\varepsilon(x)}{\varepsilon(x_{IA})} \right)^{0.25} + \Delta P_{SW} \left(\frac{\varepsilon(x)}{\varepsilon(x_{IA})} \right)^{0.25}$	(3.58)
Slug and Intermittent	-	$\Delta P = \Delta P_{LO} \left(1 - \frac{\varepsilon(x)}{\varepsilon(x_{IA})} \right)^{0.25} + \Delta P_A \left(\frac{\varepsilon(x)}{\varepsilon(x_{IA})} \right)^{0.25}$	(3.59)
Stratified wavy	-	$\Delta P_{SW} = 4f_{TPH,SW} \frac{L\rho_v V_v^2}{2D_2}$	(3.60)
Annular	-	$\Delta P_A = 4f_{TPH,A} \frac{L\rho_v V_v^2}{2D_2}$	(3.61)

Table 3.3 – Continuation

Flow pattern	Special condition	Model	Eq.
Dryout	-	$\Delta P = \Delta P_{TPH}(x_{di})$ $-\frac{x - x_{di}}{x_{de} - x_{di}} [\Delta P_{TPH}(x_{di}) - \Delta P_m(x_{de})]$	(3.62)
Mist	-	$\Delta P_m = 2f_H \frac{LG^2}{\rho_H D_2}$	(3.63)

Figure 3.11 shows heat transfer coefficient (a), pressure gradient (b), mechanical energy correction factor (c), and Reynolds number (d) versus steam quality based on [7]. Diamonds represents the same parameters at single-phase saturated state (liquid and vapor). It is noticed that variation of heat transfer coefficient, pressure gradient, and Reynolds number are very important at high steam quality. It is also noticed the quasy-continuity between two-phase and single-phase modeling. The impact of pressure gradient is very high at high steam quality, obtaining up to 25 times the pressure gradient at saturated liquid. Heat transfer coefficient decays fast at very high steam quality (dryout flow). Variation of mechanical energy is more imporant at low steam quality, which influences into mechanical energy change at this state.

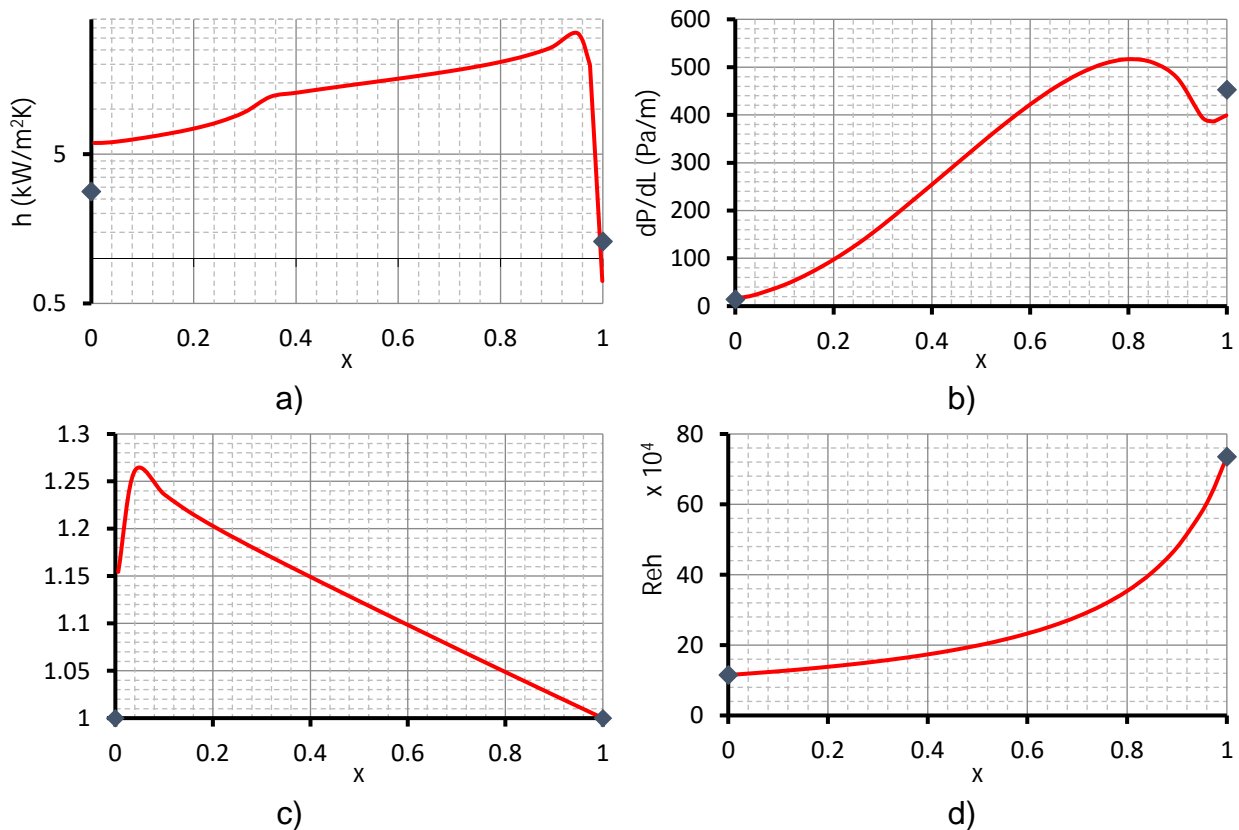


Fig. 3.11 – Thermo-hydraulic parameters vs. quality in two-phase phenomena

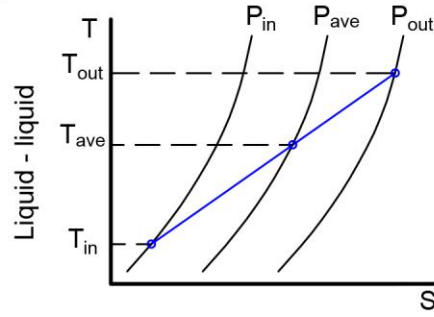
3.1.5 Modeling phase change phenomena

Phase change phenomena involves the computation of thermophysical and hydraulic properties of the fluid considering its inlet and outlet conditions. Temperature, pressure, enthalpy, and quality are base parameters for computing fluid properties and dimensionless numbers. There are five possible scenarios, which each are described below as inlet - outlet. Figure 3.12 shows the temperature vs. entropy diagrams of each scenario.

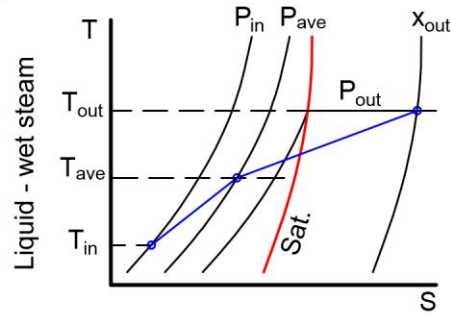
- a) **Liquid - liquid:** Inlet and outlet has a steam quality of -100 ^{a)}. Inlet enthalpy is obtained at inlet temperature and pressure, and then it is added differential enthalpy to obtain outlet enthalpy. Differential pressure is computed as single-phase flow. Outlet and average temperatures are estimated at outlet and average pressure and enthalpy respectively.
- b) **Liquid - wet steam:** Inlet properties are obtained at inlet temperature and pressure. Outlet enthalpy is the inlet enthalpy plus differential enthalpy. Average properties are obtained at average pressure and enthalpy. In this case, there are three possible cases of average conditions: liquid, saturated or wet-steam. Due to numerical errors of the phase change modeling, saturated liquid is considered at quality between 0 and 0.001. Differential pressure is calculated depending on average conditions (single-phase for liquid and saturated, two-phase for wet steam).
- c) **Wet steam - wet steam:** All properties (except enthalpy) depends on quality and pressure. Average temperature is estimated as saturated temperature at average pressure. Outlet quality is the quality as function of the outlet enthalpy and outlet pressure. Differential pressure is computed as two-phase flow based on average conditions.
- d) **Wet steam – dry steam:** This is similar to liquid – wet steam scenario. The difference are the cases of average conditions: wet steam, saturated steam, or dry steam. Due to numerical errors of the model, saturation is considered at qualities between 0.999 to 1. Single-phase differential pressure is obtained at dry and saturated steam average conditions, otherwise two-phase differential pressure is calculated.
- e) **Dry steam – dry steam:** Similar to liquid – liquid scenario, but with $x=100$ ^{a)}.

These five scenarios also apply to energy balance at interconnecting piping. The difference is that in those cases, differential enthalpy is negative due to it is a heat loss. Change in mechanical energy only depends on inlet and outlet conditions, so it is estimated by correction factor and fluid velocity depending on fluid state.

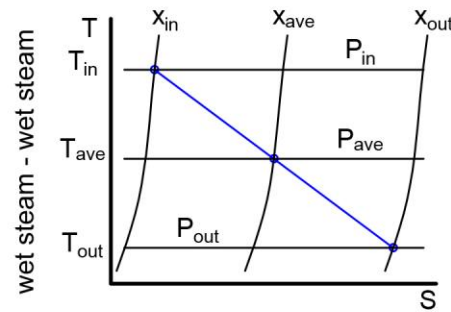
^{a)} The EES software uses flags for over-heated steam and sub-cooled liquid as 100 and -100 respectively.



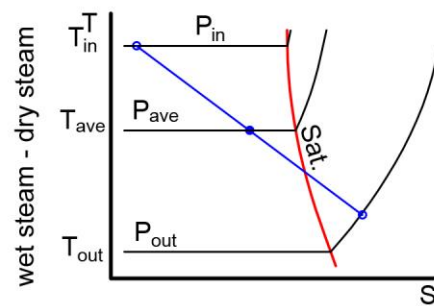
$$\begin{aligned}
 h_{out} &= h(T_{in}, P_{in}) + \Delta h_S \\
 h_{ave} &= h(T_{in}, P_{in}) + \Delta h_S/2 \\
 P_{out} &= P_{in} - \Delta P_S \\
 P_{ave} &= P_{in} - \Delta P_S/2 \\
 T_{ave} &= T(P_{ave}, h_{ave})
 \end{aligned}$$



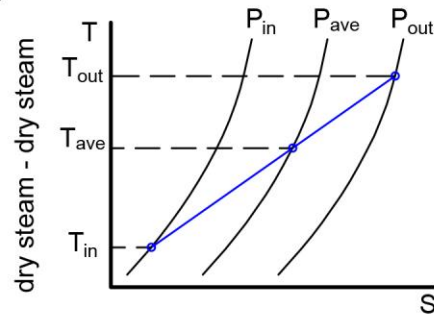
$$\begin{aligned}
 h_{out} &= h(T_{in}, P_{in}) + \Delta h_S \\
 h_{ave} &= h(T_{in}, P_{in}) + \Delta h_S/2 \\
 x_{ave} &= x(h_{ave}, P_{ave}) \\
 \Delta P_S &= f(x_{ave}) \\
 T_{out} &= T_{sat}(P_{out})
 \end{aligned}$$



$$\begin{aligned}
 h_{out} &= h(x_{in}, P_{in}) + \Delta h_S \\
 h_{ave} &= h(x_{in}, P_{in}) + \Delta h_S/2 \\
 P_{ave} &= P_{in} - \Delta P_S/2 \\
 x_{ave} &= x(h_{ave}, P_{ave})
 \end{aligned}$$



$$\begin{aligned}
 h_{out} &= h(x_{in}, P_{in}) + \Delta h_S \\
 h_{ave} &= h(x_{in}, P_{in}) + \Delta h_S/2 \\
 x_{ave} &= x(h_{ave}, P_{ave}) \\
 \Delta P_S &= f(x_{ave})
 \end{aligned}$$



$$\begin{aligned}
 h_{out} &= h(T_{in}, P_{in}) + \Delta h_S \\
 h_{ave} &= h(T_{in}, P_{in}) + \Delta h_S/2 \\
 P_{out} &= P_{in} - \Delta P_S \\
 P_{ave} &= P_{in} - \Delta P_S/2 \\
 T_{ave} &= T(P_{ave}, h_{ave})
 \end{aligned}$$

Fig. 3.12 – Temperature vs. entropy diagrams for phase change phenomena

3.1.6 Internal forced convection using Al₂O₃/water nanofluids

Two approaches were analyzed in internal forced convection modeling of solar-energy-to-heat conversion using nanofluids: single-phase and Nusselt-correlation. The single-phase approach obtains effective single-phase properties based on base-fluid and nanoparticle properties, then the heat transfer coefficient and pressure drop were obtained using (3.25) – (3.28) (see Section 3.1.3). Equations (3.64) – (3.67) describes the effective single-phase properties of the nanofluid. In this approach, the value of the convection coefficient depends whether the flow is laminar, in transition, or turbulent, dependent on the Reynolds number. Most properties of the fluid are obtained at the mean free-flow temperature, which is an average of the superficial and mean bulk temperatures of the fluid, except for Pr_w which is obtained at the inner pipe superficial temperature. Mixing theory was used to calculate the density and specific heat of the nanofluid. The viscosity was obtained by the Masoud-Moghadassi correlation [8], and the thermal conductivity was calculated with the Corcione correlation [9], for the Al₂O₃/water nanofluid.

$$\rho_{nf} = (1 - \varphi)\rho_{bf} + \varphi\rho_{np} \quad (3.64)$$

$$C_{p\,nf} = \frac{(1 - \varphi)(\rho C_p)_{bf} + \varphi(\rho C_p)_{np}}{(1 - \varphi)\rho_{bf} + \varphi\rho_{np}} \quad (3.65)$$

$$\frac{\mu_{nf}}{\mu_{bf}} = \exp\left(0.72 - 0.485\frac{T_a + 273}{T_{ref}} + 14.9\varphi\left(\frac{d_{np} + 2s}{d_{np}}\right)^3 + 0.0105\frac{d_{np}}{s_0 + s}\right) \quad (3.66)$$

$$\frac{k_{nf}}{k_{bf}} = 1 + 4.4\left(\frac{2\rho_{bf}k'_b(T_a + 273)}{\pi\mu_{bf}^2d_{np}}\right)^{0.4}\left(\varphi\left(\frac{C_p\mu}{k}\right)_{bf}\right)^{0.66}\left(\frac{T_a + 273}{T_{fr}}\right)^{10}\left(\frac{k_{np}}{k_{bf}}\right)^{0.03} \quad (3.67)$$

Nusselt-correlation approach consists of calculating the heat transfer coefficient using exclusive correlations for the Al₂O₃-water nanofluid, instead of using single-phase correlations. The friction factor and thermophysical properties of the nanofluid are obtained by (3.29) – (3.31) and (3.68) – (3.69) respectively, as described in an earlier section. Correlations developed by Maïga et al. [10,11] are used to calculate the Nusselt number in this approach. Due to a lack of correlations for convective heat transfer with nanofluids, the validity range of Reynolds number was modified to cover laminar and turbulent regimes. Figure 3.13 shows the thermal model using this approach.

$$Nu = \max\left(0.086Re^{0.55}Pr^{0.5}\left(\frac{Pr}{Pr_w}\right)^{0.11}, 4.364\left(\frac{Pr}{Pr_w}\right)^{0.11}\right) \text{ for laminar flow} \quad (3.68)$$

$$Nu = 0.085Re^{0.71}Pr^{0.35}\left(\frac{Pr}{Pr_w}\right)^{0.11} \text{ for turbulent flow} \quad (3.69)$$

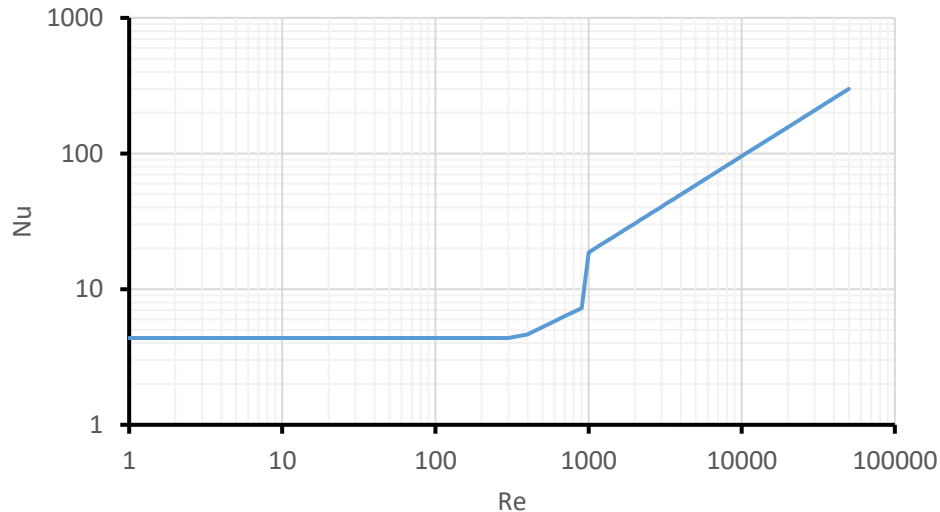


Fig. 3.13 – Nu vs. Re for internal forced convection using Al₂O₃/water nanofluid (Pr/Pr_w=1)

3.1.7 Other Heat Transfer Phenomena

Radiation and other convective heat transfer mechanisms involved into solar-energy-to heat conversion are explained below. Table 3.4 resumes the mathematical model used to calculate heat transfer flows. There is also an explanation about the validity of the correlations used, the assumptions of considering those correlations, and the considerations of some properties.

3.1.7.1 Natural annular convection

Describes the heat transfer by convection between the cover glass and the pipe ($q'_{34,rad}$). A correlation developed by Raithby and Hollands is used. This correlation obtains the heat transfer between two long, horizontal, concentric, cylindrical, isothermal surfaces; and assumes that the fluid in the annular region is not in an extreme vacuum. Its validity is for $Ra > (D/(D - d))^4$ and $k_{eff}/k_{34} > 1$.

A correlation developed by Ratzel et. al is used for extreme vacuum cases. This correlation assumes the same heat transfer conditions as Raithby and Hollands correlation, and it is valid for $Ra < (D/(D - d))^4$. It is worth nothing that this correlation can overestimate the heat transfer at very low (<0.013Pa) pressures [12]. For both correlations, properties are obtained using average temperature of the fluid.

3.1.7.2 Natural external convection

Under conditions of low wind velocity (<0.1 m/s), it is considered as natural convection in the outside surface of the glass cover (or pipe in case of non-covered receivers). Churchill and Chu developed a correlation for this heat transfer mechanism. It models the convection around a large, horizontal, isothermal, cylindrical surface, where the surrounding air develops laminar and turbulent boundary layers all around the surface.

Table 3.4 – Mathematical model for other heat transfer phenomena

Heat flow type	Special condition	Model	Eq.	Ref.
Natural annular convection	Non-evacuated	$q' = 2\pi\Delta T \frac{k_{eff}}{\ln(D/d)} = \frac{2.425k_{34}\Delta T}{\left(1 + \left(\frac{d}{D}\right)^{3/5}\right)^{5/4}} \sqrt[4]{\frac{PrRa_d}{0.861 + Pr}}$	(3.70)	[13]
	evacuated	$h = \frac{k}{\frac{D}{2} \ln\left(\frac{d}{D}\right) + \left(\frac{9\gamma - 5}{2(\gamma + 1)}\right) \left(C_a \frac{\bar{T}_{23} + 273}{P_a \delta^2}\right) \left(\frac{d}{D} + 1\right)}$	(3.71)	[14]
Natural external convection	-	$Nu = \left[0.6 + \frac{0.387Ra^{1/6}}{\left(1 + \left(\frac{0.559}{Pr}\right)^{9/16}\right)^{8/27}} \right]^2$	(3.72)	[15]
Cross-flow external forced convection	-	$Nu = CRe^m Pr^n \left(\frac{Pr}{Pr_w}\right)^{1/4}; C, m = f(Re); n = f(Pr)$	(3.73)	[16]
External convection in extended surfaces	Wind velocity	$q'_b = n_b \sqrt{hP_b k_b A_c} \frac{\Delta T}{L}; h = Nu \frac{k}{D_h}$ <p style="text-align: center;"><i>Nu depends on type of external convection</i></p>	(3.74)	[17]
Radiation in annular region	-	$q' = \frac{\sigma\pi D(T_D^4 - T_d^4)}{\frac{1}{\varepsilon_d} + \frac{D(1 - \varepsilon_D)}{d\varepsilon_D}}$	(3.75)	[17]
External radiation	-	$q' = \sigma\varepsilon\pi D(T_D^4 - T_{ci}^4)$ $T_{ci} = T_\infty \sqrt[4]{\varepsilon_{ci}}; \varepsilon_{ci} = 0.711 + 0.56 \frac{T_{dew}}{100} + 0.73 \left(\frac{T_{dew}}{100}\right)^2$	(3.76)	[17, 18]

Fluid properties are evaluated at the average boundary-layer temperature, which is the average between superficial and mean bulk temperature of the fluid. This correlation is valid up to $Ra > 10^{12}$, which covers a large range of natural convective phenomena.

3.1.7.3 Cross-flow external forced convection

This heat transfer mechanism occurs when the external surface of the receiver is under medium-to-high wind velocity. A cross-flow is used to simplify the mathematical model. A correlation developed by Zhukauskas is used, which assumes forced convection with fluids in a cross flow around a long smooth isothermal cylindrical surface. The advantages of this correlation are the large validity range of the Reynolds number and the ease of its computation. Similar to the natural external convection, the fluid properties are calculated at the mean boundary-layer temperature, except for Pr_w (at wall temperature). Table 3.5 shows the values of the constants used in (3.73).

Table 3.5 - Constants for Zhukauskas correlation

Re	C	m
1 – 40	0.75	0.4
40 – 1000	0.51	0.5
1000 – 2×10^5	0.26	0.6
$2 \times 10^5 – 10^7$	0.076	0.7

If $Pr < 10$, $n = 0.37$; if $Pr > 10$, $n = 0.36$

3.1.7.4 External convection in extended surfaces

This heat transfer phenomenon takes place at the surface of brackets ($q'_{3s,cond}$). It is modeled as convective losses occurring at constant-area, infinite extended surfaces. The Nusselt number is calculated according to the type of external convection in the surroundings, whether natural or forced cross-flow, and the formula is the same as described previously. The fluid properties also depend on the convection type. The properties along the brackets are considered constant.

3.1.7.5 Radiation in Annular region

Besides convection, radiative heat losses take place in the annular region in covered receivers. Key assumptions are that the surfaces are long, isothermal, gray, concentric cylinders; and that the fluid between the surfaces does not participate in the radiative heat transfer [17].

3.1.7.6 External radiation

External radiation occurs at the external surface of the receiver, exchanging heat with the atmosphere. It is modeled as radiative heat exchange between a gray body inside a large

hemispherical dome. The sky temperature depends on the ambient dew point temperature, where Martin and Berdahl correlation is used to calculate the sky temperature in humid ambient air.

3.2 A brief description of thermal analysis using Engineering Equation Solver

3.2.1 Background

Before explaining how to make thermal analysis using the developed code, it is important to understand how Engineering Equation Solver (EES) works. EES is a numerical equation-solver that can solve system with linear and non-linear algebraic equations and/or differential equations [19]. Solving equations automatically is one of the advantages of this software, so it is not needed to program an iterative numerical method to solve systems of equations. Another feature is that it has a database of thermo-physical properties of many substances, making this software a potential tool to solve engineering problems. This is useful in the case of modeling two-phase flow with water. These features are the key reason of selecting EES for this research. Other features used in this research are the input data by a graphic user interface, parametric tables, data input by tables, and the use of arrays to show results. The use of those features is explained below.

3.2.2 Input data window

The input data consists in three parts: the ambient conditions, collector design and system description. All three input sections are in the diagram window (graphical interface). Figure 3.14 shows the input data for the ambient conditions section. It is noticed that the input corresponds to instantaneous measurements (for steady-state analysis).

Parameter	Value	Unit
Direct Beam Radiation	890.1	[W/m ²]
Wind Velocity	3.86	[m/s]
Ambient Temperature	24.18	[C]
Ambient Pressure	1	[atm]
Incidence Angle	27.86	[degrees]
Relative Humidity	70	[%]

Fig. 3.14 – Inputs for ambient conditions of collector system

The second section corresponds to the collector design. The data needed are the geometry, materials, and properties (thermo-physical or optical) of the collector. Figure 3.15 shows the window of the collector design. A user can define its own collector as “User-Defined”, but there are other three models in database (LS-2, LS-3 or IST). Glass envelope, absorber, brackets, mirrors, and collector dimensions sub-section define

geometrical, thermo-physical and/or optical properties of each part of the collector related with energy conversion. Users can change optical properties of selective coating in sub-section “Absorber” by selecting “User-Defined” and changing data of “Selective Coating Properties” sub-section for non-programmed selective coatings. Gas in annular region and its pressure are defined in “Gas in Annulus” sub-section (in case of vacuum, specify the pressure). Optical efficiency can be defined by separated factors or combined in one in “Optical Efficiency Terms” sub-section. Finally, incident angle modifier is defined by standard equation used in the literature.

The screenshot displays the 'Collector Design' software interface with a central diagram of a collector tube. The interface is divided into several sections with input fields and dropdown menus:

- Collector Design:** A dropdown menu set to 'User-Defined'.
- Glass Envelope:**
 - Glazing?: Yes
 - Emittance: 0.86
 - Asorptance: 0.02
 - Thermal Conductivity: 1.04 [W/m-K]
 - Inner Diameter: 0.115 [m]
 - Outer Diameter: 0.108 [m]
 - Transmittance: 0.96
- Absorber:**
 - Material: 321H
 - Inner Diameter: 0.05 [m]
 - Outer Diameter: 0.07 [m]
 - Selective Coating: Solel UVAC Cermet (SNL test b)
 - HTF Flow Type: Pipe Flow
 - HTF inner diameter for annulus flow: 0.0508 [m]
- Brackets:**
 - Transversal Perimeter: 0.106 [m]
 - Hydraulic Diameter: 0.00566 [m]
 - Cross Section Area: 0.00015 [m²]
 - 3 brackets per collector
 - Thermal Conductivity: 48 [W/m-K]
- Mirrors:** Reflectivity: 0.94
- Gas in Annulus:**
 - Gas: Air
 - Absolute Pressure: 0.0001 [atm]
- Collector Dimensions:**
 - Total Aperture Length: 5.76 [m]
 - Total Collector Length: 25 [m]
 - Focal Distance: 1.49 [m]
- Selective Coating Properties:**
 - Absorptance: 0.96
 - Emittance @ 100C: 0.04
 - Emittance @ 400C: 0.2327
 - Weighted Reflectivity: 9
- Optical Efficiency Terms:**
 - Shading: 0.7281
 - Tracking Error: 1
 - Geometry: 1
 - Dirt on Mirror: 1
 - Dirt on HCE: 1
 - General: 1
- Incident Angle Modifier:**
 - Equation: $K = 1 + a_1 * \theta / \cos(\theta) + a_2 * \theta^2 / \cos(\theta)$
 - a_1 : -0.00275
 - a_2 : -0.0001408

Fig. 3.15 – Inputs for collector design used in thermal analysis

Finally, the system description window shows data related to instantaneous operation of the system. Figure 3.16 shows the input/output data of this section. Inlet flow conditions (pressure, temperature, quality in case of water), flow rate and HTF are defined in “Inlet Data” sub-section; while “Matrix Data” refers to the hydraulic configuration of the system. In case of a system with parallel configuration, the number of rows in matrix should be greater than one. This sub-section also shows some output data of the land area used. In case of parallel configuration, the analysis of each row will be realized by dividing the input flow rate to the number of rows (equal flow rate in all rows).

It is important to notify that for parametric analysis, the variables to assume as to be parametrized should be deactivated from diagram window. This will avoid errors during the analysis. For more information, see Appendix B.

Inlet Data

Temperature [C]

Manometric Pressure [bar]

Flow Rate [gpm]

HTF

Inlet quality

Matrix Data

Number of Rows in Matrix

Number of Collectors per Row

Space between Collector Lines (E) [m]

Max. Tilt Angle without Shadowing (β) 56.63 [degrees]

Reflective Land Area 0.0002684 [ha]

Total Land Area 0.0002684 [ha]

System Description

Fig. 3.16 – Inputs for system description section.

3.2.3 Convergence

Users can define upper and lower limits of each variable by clicking on or pressing F9. Selecting the correct limits can diminish computational time and avoid divergence errors. For example, Figure 3.17 shows atmospheric pressure and critical pressure as limits of pressure of water inside the pipe. If those limits are not defined, the algorithm can solve equations outside this range, making the solution practically impossible. If limits are wrong defined, the algorithm would show a warning message as shown in Figure 3.18 (the variable has a fixed limit). Default limits are “-infinity” and “infinity”.

Variable Information ? X

Show array variables MAIN program

Show string variables

Variable	Guess	Lower	Upper	Display	Units	Key	Comment
P_1ave[1]	101330	1.0133E+05	2.0000E+07	A 0 N			
P_1ave[2]	101330	1.0133E+05	2.0000E+07	A 0 N			
P_1ave[3]	101330	1.0133E+05	2.0000E+07	A 0 N			
P_1ave[4]	101330	1.0133E+05	2.0000E+07	A 0 N			
P_1ave[5]	101330	1.0133E+05	2.0000E+07	A 0 N			
P_1ave[6]	101330	1.0133E+05	2.0000E+07	A 0 N			
P_1ave[7]	101330	1.0133E+05	2.0000E+07	A 0 N			
P_1ave[8]	101330	1.0133E+05	2.0000E+07	A 0 N			
P_1ave[9]	101330	1.0133E+05	2.0000E+07	A 0 N			
P_1ave[10]	101330	1.0133E+05	2.0000E+07	A 0 N			
P_1ave[11]	101330	1.0133E+05	2.0000E+07	A 0 N			
P_1ave[12]	101330	1.0133E+05	2.0000E+07	A 0 N			
P_1ave[13]	101330	1.0133E+05	2.0000E+07	A 0 N			

Fig. 3.17 – Defining variable limits

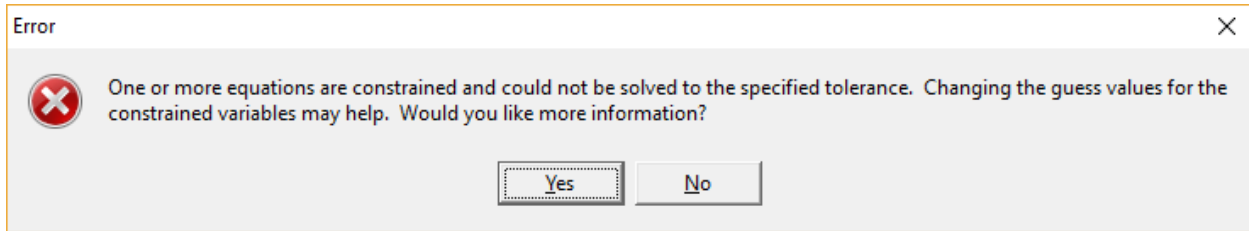





Fig. 3.18 – Warning message for convergence

3.2.4 Output data window

The problem will be solved by clicking on  or pressing F2. Solution window (click on  or press Ctrl + U) shows results for non-array variables (including input variables) and the last calculation of functions and procedures. Array table (click on  or press Ctrl + Y) shows data of array variables, and it shows a $n \times 56$ array, being n the number of collectors in each row. The variables shown in the array solution are the thermo-hydraulic parameter of each collector and interconnecting piping (pressure, temperature, heat transfer, pressure drop, etc). This data can be exported to Excel to process them, in case of needed. For example, Figure 3.19 shows profiles of temperature, pressure, and quality of steam of a simulated Direct Steam Generation system installed at Plataforma Solar de Almería (green line is the steam quality).

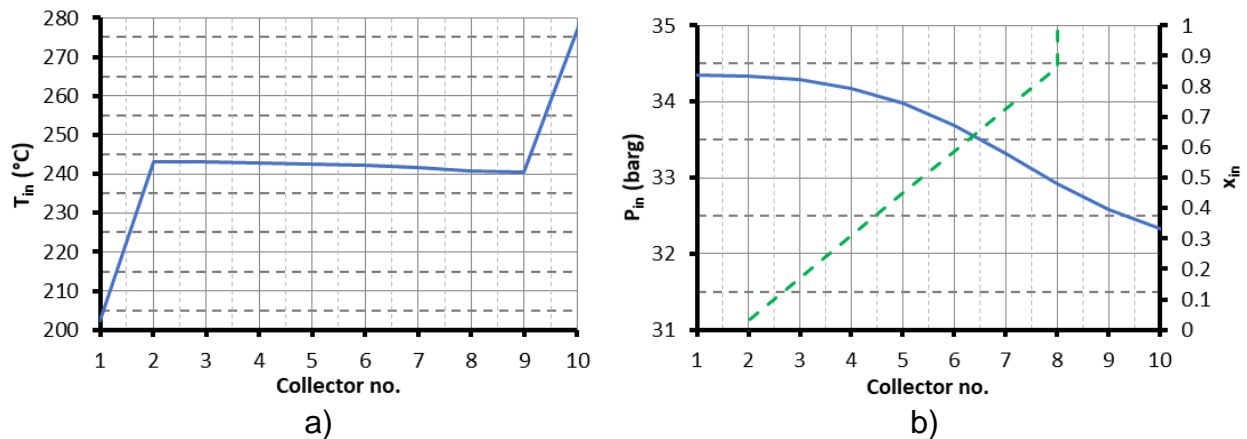


Fig. 3.19 – Temperature, pressure and quality of steam profiles.

3.3 Nomenclature

General symbols

A	Collector area (m^2)
A_b	Cross section of brackets (m^2)
A_{LD}	Cross sectional coefficient for liquid phase
A_{VD}	Cross sectional coefficient for vapor phase
C, m, n	Dimensionless constants

C_a	Constant for vacuum in annulus ($2.331 \times 10^{-20} \text{ mmHg cm}^3/\text{K}$)
C_p	Specific heat (J/kgK)
C_w	Constant for wavy two-phase heat transfer ($44 \text{ s}^{2.01}/\text{kg}^{0.17}$)
d_{np}	Diameter of the nanoparticles (m)
D	Outer diameter (m)
D_h	Hydraulic diameter (m)
D_i	Diameter at i boundary (m)
d	Inner diameter (m)
d_{np}	Nanoparticle diameter (nm)
Fr	Froude number ($G^2/(g\rho_v(\rho_l - \rho_v)D)$ for vapor phase)
f	Friction factor
$G(x)$	Mass velocity at a given quality x (kg/m ² s)
G_{w0}	Additive constant ($50 \text{ kg/m}^2\text{s}$) [20]
h	Convection heat transfer coefficient (W/m ² K)
h_{LD}	Liquid vertical height ratio
I	Direct solar irradiation (W/m ²)
k	Thermal conductivity (W/m*K)
K	Incident angle modifier
k_{ij}	Thermal conductivity of the material between i and j boundary (W/m*K)
k_b	Thermal conductivity of the brackets (W/m*K)
k'_b	Boltzmann's constant = $1.3807 \times 10^{-23} \text{ J/K}$ (for nanofluids)
k_{eff}	Effective thermal conductivity (W/m*K)
L	Collector length (m)
M	Molecular mass (kg)
\dot{m}	Mass flow (kg/s)
n_b	Number of brackets per collector
Nu	Nusselt number
P_a	Absolute pressure at annulus (mmHg)
P_b	Perimeter of cross section of brackets (m)
P_r	Reduced pressure
Pr	Prandtl number at evaluating temperature

Pr_w	Prandtl number at wall temperature
q	Heat flux (W/m^2)
q_{crit}	Critical heat flux (W/m^2)
$q'_{ij,type}$	Type heat transfer flow (See table 3.1) per length between boundaries i and j (W/m)
$q'_{i,inc}$	Incident heat transfer flow per length at i boundary (W/m)
Ra_d	Rayleigh number at evaluating temperature and d as characteristic length
Re	Reynolds number at evaluation temperature
s	Thickness of the capping layer of the nanoparticle (nm)
s_0	Adding constant of capping layer (1nm)
\bar{T}_{23}	Average temperature of annulus ($^{\circ}C$)
T_{dew}	Dew point ($^{\circ}C$)
T_{fr}	Freezing point of the base fluid (K)
T_i	Temperature at i boundary ($^{\circ}C$, K for radiation)
T_{ref}	Reference temperature (293 K)
\dot{V}	Flow volume (m^3/s)
v	Flow velocity (m/s)
W	Collector width (m)
We	Weber number
x	Vapor quality

Greek letters

α_i	Absorptance at i boundary
β	Kinetic energy correction factor
γ	Specific heat ratio
γ_c	Interception factor of the collector
δ	Molecular diameter of annulus gas (cm)
δ	Liquid film thickness for two-phase flow (m)
Δh_s	Collector enthalpy difference (W/kg)
ΔT_{ij}	Temperature difference between i and j boundaries ($^{\circ}C$)
θ	Incident angle

$\theta_d(x)$	Dry angle of tube perimeter (rad)
$\theta_s(x)$	Stratified flow angle of tube perimeter (rad)
ε_i	Emittance at i boundary
$\varepsilon(x)$	Void fraction
Λ	Superficial tension (N/m)
η	Collector thermal efficiency
η_{op}	Optical efficiency
μ	Viscosity (Pa s)
π	Pi constant
ρ	Density (kg/m ³)
σ	Stefan-Boltzmann constant
φ	Volume fraction of the nanoparticles (vol%)

Boundaries and subscripts

$1i$	Collector inlet
$1o$	Collector outlet
$1ave$	Fluid mean bulk
2	Inner pipe surface
3	Outer pipe surface
4	Inner cover glass surface (outer surface of insulation for interconnecting piping)
5	Outer cover glass surface
a	Atmosphere
c	Sky
bf	Base fluid
di	Dryout inlet
de	Dryout exit
G, I	Geometric property in interconnections
H, I	Hydraulic property in interconnections
H	Homogeneous property (two-phase flow)
I	Interconnecting piping
IA	Intermittent to annular transition

l	Saturated liquid
nf	Nanofluid
np	Nanoparticle
s	Outside of the brackets (extended surface)
S	Section
TPH	Two-phase
v	Saturated vapor

3.4 References

- [1] Forristall R. Heat transfer analysis and modelling of a parabolic trough solar receiver implemented in Engineering Equation Solver. Golden (CO): NREL; 2003. 164p. Report No.: NREL/TP-550-34269.
- [2] F-Chart Software. EES [internet]. F-Chart Software [cited 2018 May 2]. Available from: <http://www.fchart.com/ees/>
- [3] Kakaç S, Shah R, Aung W. Handbook of single-phase convective heat transfer. New York: Wiley; 1987.
- [4] Wojtan L, Ursenbacher T, Thome JR. Investigation of flow boiling in horizontal tubes: Part I – A new diabatic two-phase flow pattern map. Int J Heat Mass Transfer. 2005;48:2955-69.
- [5] Wojtan L, Ursenbacher T, Thome JR. Investigation of flow boiling in horizontal tubes: Part II – Development of a new heat transfer model for stratified-wavy, dryout and mist flow regimes. Int J Heat Mass Transfer. 2005;48:2970-85.
- [6] Quibén JM, Thome JR. Flow pattern based two-phase frictional pressure drop model for horizontal tubes, Part II: New phenomenological model. Heat Fluid Flow. 2007;28:1060-1072.
- [7] Elsafi A. On thermo-hydraulic modeling of direct steam generation. Sol Energ. 2015;120:636-650.
- [8] Hosseini S, Moghadassi A, Henneke D. A new dimensionless group model for determining the viscosity of nanofluids. J Therm Anal Calorim. 2010;100(3):873–7.
- [9] Corcione M. Empirical correlating equations for predicting the effective thermal conductivity and dynamic viscosity of nanofluids. Energy Convers Manag. 2011;52(1):789–93.

- [10] Maïga S, Palm S, Nguyen C, Roy G, Galanis N. Heat transfer enhancement by using nanofluids in forced convection flows. *Int J Heat Fluid Flow*. 2005;26(4):530-46.
- [11] Maïga S, Nguyen C, Galanis N, Roy G. Heat transfer enhancement in turbulent tube flow using Al₂O₃ nanoparticle suspension. *Int J Numer Method Heat Fluid Flow*. 2006;16(3):275-92
- [12] Churchill S, Chu H. Correlating equations for laminar and turbulent free convection from a horizontal cylinder. *Int J Heat Mass Transf*. 1975;18(9):1049–53.
- [13] Bejan A. *Convection heat transfer*. Hoboken (New Jersey): Wiley; 2013.
- [14] Ratzel A, Hickox C, Gartling D. Techniques for reducing thermal conduction and natural convection heat losses in annular receiver geometries. *J Heat Transf*. 1979;101(1):108.
- [15] Churchill S, Chu H. Correlating equations for laminar and turbulent free convection from a horizontal cylinder. *Int J Heat Mass Transf*. 1975;18(9):1049–53.
- [16] Žukauskas A. Heat transfer from tubes in crossflow. *Adv Heat Transf*. 1972;8:93-160.
- [17] Incropera F. *Fundamentals of heat and mass transfer*. Hoboken, NJ: Wiley; 2013.
- [18] Berdahl P, Martin M. Emissivity of clear skies. *Sol Energy*. 1984;32(5):663-4.
- [19] Klein SA, Nellis GF. *Mastering EES*. Madison, WI: F-Chart Software; 2014.
- [20] Kattan N, Thome JR, Favrat D. Flow boiling in horizontal tubes. Part I: Development of a diabatic two-phase flow pattern map. *J Heat Transf*. 1998;120(1):140-7.

Chapter 4 Results and discussion

This chapter shows a comparison between experimental data and simulated results in order to validate the thermo-hydraulic model presented in this work. Single-phase thermo-hydraulic modeling is presented in Cases 1 and 2, and two-phase modeling in Cases 3 and 4. Case 1 compares simulations and experiments of four different PTCs using a thermal oil as heat transfer fluid. Case 2 is similar to case 1 but using Al_2O_3 /water nanofluid as heat transfer fluid. Case 3 compares experimental and simulated temperature and pressure profiles of a direct steam generation. Case 4 presents a pre-design analysis for implementing PTC technology into an industrial process.

4.1 Case 1: Thermal efficiency curves

This section shows a comparison of experimental data and simulated results of 4 PTC test results presented in the literature. Simulations were carried out using geometrical data, operational/ambient conditions, and thermophysical/optical properties of materials given in the corresponding reports. Design data used in simulations are presented in Table 4.1. All tests were realized in steady-state conditions varying ambient and operational parameters (such as solar radiation, wind velocity, flow rate or inlet temperature) as stated in test reports. Simulated outlet temperature (T_{out}), difference temperature in collector (ΔT), average fluid temperature above ambient (ΔT_{amb}), and thermal efficiency (η) are taken as “output parameters” to compare with reported data.

4.1.1 LS-2 with a PTR-70 receiver

Moss and Brosseau [1] reported test results of a PTR-70 receiver coupled to a LS-2 PTC. Outdoor tests were carried out at SANDIA Laboratories, in Albuquerque. All thermal efficiency tests were realized under zero-incidence using Syltherm 800 as HTF. Water was used only in test for peak thermal efficiency. Average measured ambient parameters in tests were around $934 - 1051 \text{ W/m}^2$ for direct-beam solar radiation, $1.3 - 6.2 \text{ m/s}$ for wind velocity, and $13.9 - 14.8 \text{ GPM}$ for flow rate (9.95 GPM for peak-efficiency test with water).

Figure 4.1 shows thermal efficiency curves using experimental data, simulated results, and characteristic equation given in test results. Figure 4.2 shows the comparison of simulations and experiments for the output parameters. It is noticed that difference temperature in collector and thermal efficiency have a notable variability (Figure 4.2 b and d). Others output parameters do not show variability with experimental data. This behavior is repeated in all cases presented.

Absolute errors between simulations and experiments are represented in boxplots shown in Figure 4.3. Table 4.2 shows statistical resume of output-parameters' absolute errors. Average absolute error for ΔT is around 0.39°C , which it represents around 6 times the accuracy of the RTDs used in experiments ($\pm 0.06^\circ\text{C}$). For thermal efficiency, average absolute error is around 1.5%, which shows good agreement with experiments since test results report uncertainties of around 1%-2% for thermal efficiency.

Table 4.1 – Resume of geometrical parameters of simulated collectors

Collector	LS-2 with a PTR-70	LS-2 with an UVAC receiver ^{a)}					Urssa Trough	CAPSOL
W (m)	4.8235	4.8235	4.8235	4.8235	4.8235	4.8235	5.76	1
L (m)	7.9	7.9	7.9	7.9	7.9	7.9	71.17	2
fp (m)	1.49	1.49	1.49	1.49	1.49	1.49	???	0.2
γ	0.8091	0.8091	0.8091	0.8091	0.8091	0.8091	0.79	0.95
errors	0.9063	0.9158	0.9158	0.9158	0.9158	0.9158	0.8944	0.903
Receiver	PTR70	Evacuated	Non-evacuated	No glass	Evacuated	Non-evacuated	PTR70	Non-evacuated
Pipe	321H	321H	321H	321H	321H	321H	321H	321H
D2 (m)	0.066	0.06258	0.06258	0.06258	0.06258	0.06258	0.066	0.015
D3 (m)	0.07	0.073	0.073	0.073	0.073	0.073	0.07	0.018
Glass	Pyrex	Pyrex	Pyrex	-	Pyrex	Pyrex	Pyrex	Borosilicate
D4 (m)	0.119	0.108	0.108	-	0.108	0.108	0.119	0.0324
D5 (m)	0.125	0.115	0.115	-	0.115	0.115	0.125	0.038
	0.96	0.95	0.95	-	0.95	0.95	0.96	0.91
ε	0.86	0.86	0.86	-	0.86	0.86	0.86	0.86
α	0.02	0.02	0.02	-	0.02	0.02	0.02	0.02
k (W/m K)	1.04	1.04	1.04	-	1.04	1.04	1.04	1.04
Coating	Cermet (avg)		Cermet (avg)			Black Chrome	Cermet (avg)	Black Chrome
α	0.96	0.96	0.96	0.96	0.95	0.95	0.96	0.96
ε @ 100	-	-	-	-	-	-	-	-
ε @ 400	-	-	-	-	-	-	-	-
Mirrors	???	Silvered	Silvered	Silvered	Silvered	Silvered	???	
ρ	0.93	0.93	0.93	0.93	0.93	0.93	0.93	0.89

^{a)} Considered using a standard stainless steel Sch 40 pipe

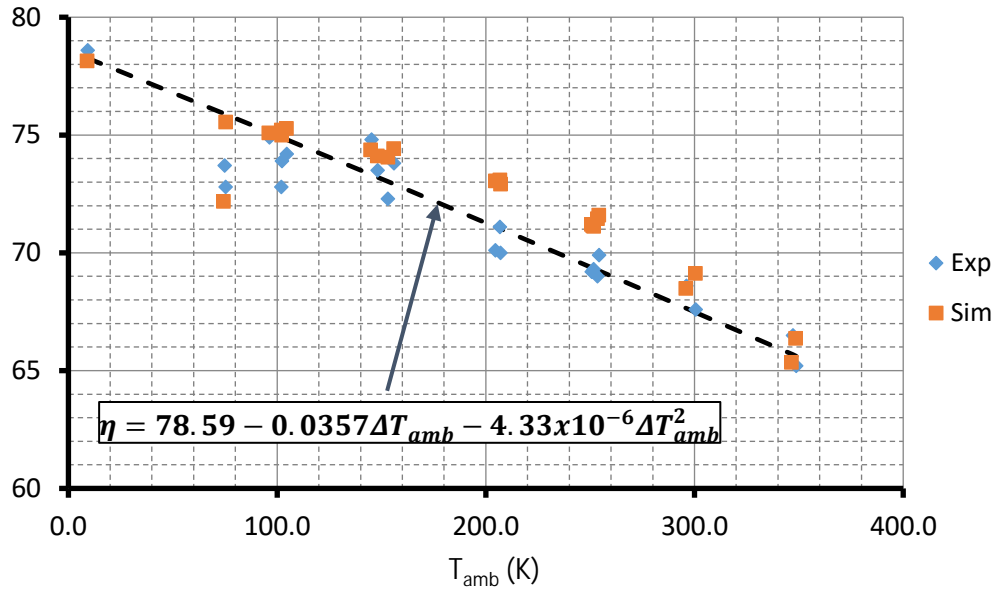


Fig. 4.1 – Efficiency curve for LS-2 with PTR-70 receiver

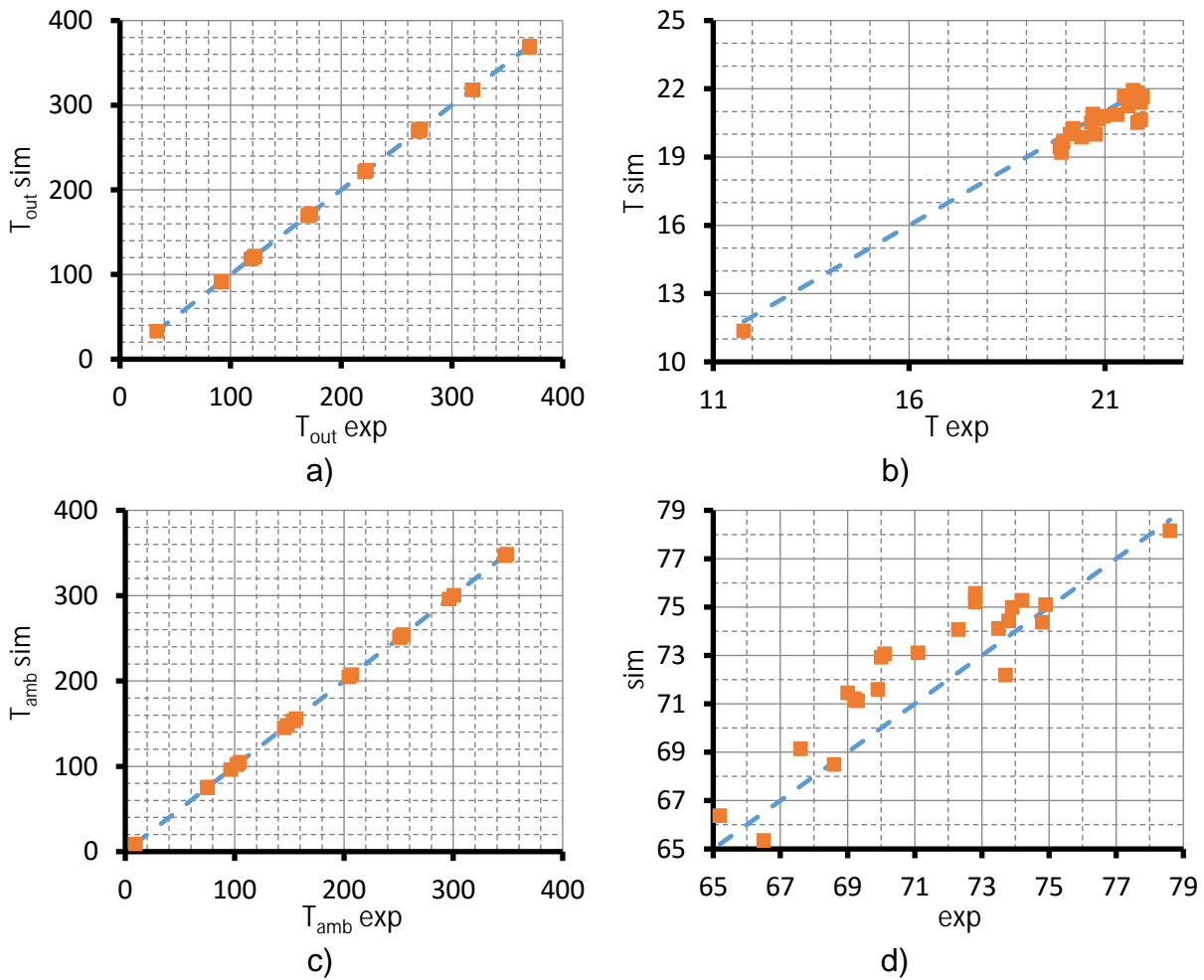


Fig. 4.2 – Comparison of output parameters for LS-2 with PTR-70 receiver

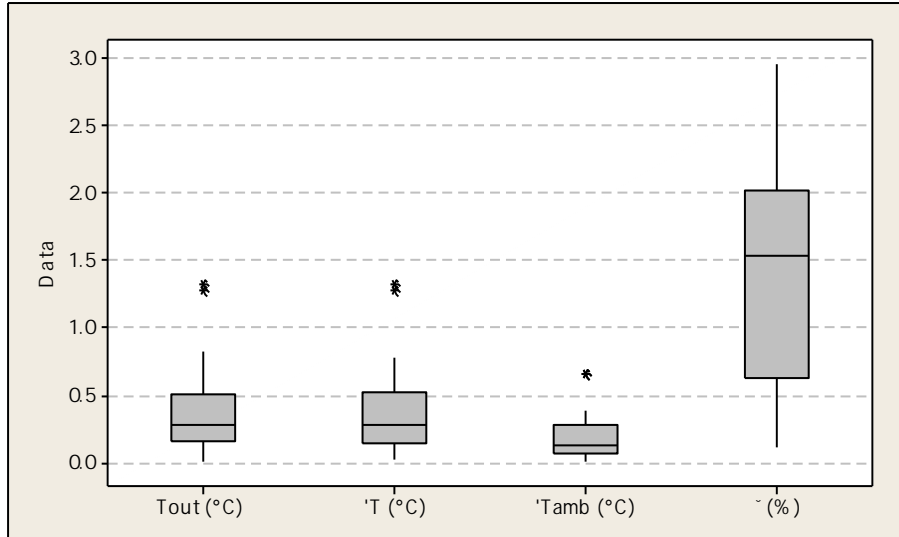


Fig. 4.3 – Absolute errors' boxplots of output parameters for LS-2 with PTR-70 receiver

Table 4.2 – Descriptive statistics for absolute errors (LS-2 + PTR-70)

	Tout (°C)	ΔT (°C)	ΔTamb (°C)	η (%)
Test range	33.13 – 370.3	11.78 – 21.96	9.26 – 348.71	65.2 – 78.6
Min	0	0.02	0.005	0.11
Max	1.32	1.32	0.655	2.96
Average	0.388	0.387	0.198	1.508
St Dev	0.354	0.347	0.179	0.864

4.1.2 LS-2 with an UVAC receiver

Dudley et al. [2] reported test results of a LS-2 PTC with an UVAC receiver using 5 different design conditions: evacuated receiver with Cermet coating, non-evacuated receiver with Cermet coating, no glass-covered receiver with Cermet coating, evacuated receiver with Black Chrome coating, and non-evacuated receiver with Black Chrome coating. Test facility and HTF used were the same as described in previous section. Average measured ambient parameters in tests using evacuated (vacuum in annulus) and non-evacuated (air in annulus) receivers were around 744.6 – 982.3 W/m² for direct-beam solar radiation, 0 – 5.9 m/s for wind velocity, and 12.6 – 15 GPM for flow rate (≈5 GPM for peak-efficiency test with water). No glass-covered receiver will be discussed separately. Due to a lack of information about pipe used in receiver, a standard stainless steel 2 ½” Sch 40 was simulated in order to determine the influence of pipe thickness into thermal behavior.

Figures 4.4 and 4.5 shows thermal efficiency curves comparing experiments, simulations, and equations reported for evacuated and non-evacuated receivers using Cermet and Black Chrome coatings respectively. The non-evacuated cases (air in annulus) shows a lower thermal efficiency than evacuated cases. This is caused by the presence of air in the annulus region, which increase thermal losses by convection compared with

evacuated receiver. In addition, simulated results tend to follow the experimental data all over the range of ΔT .

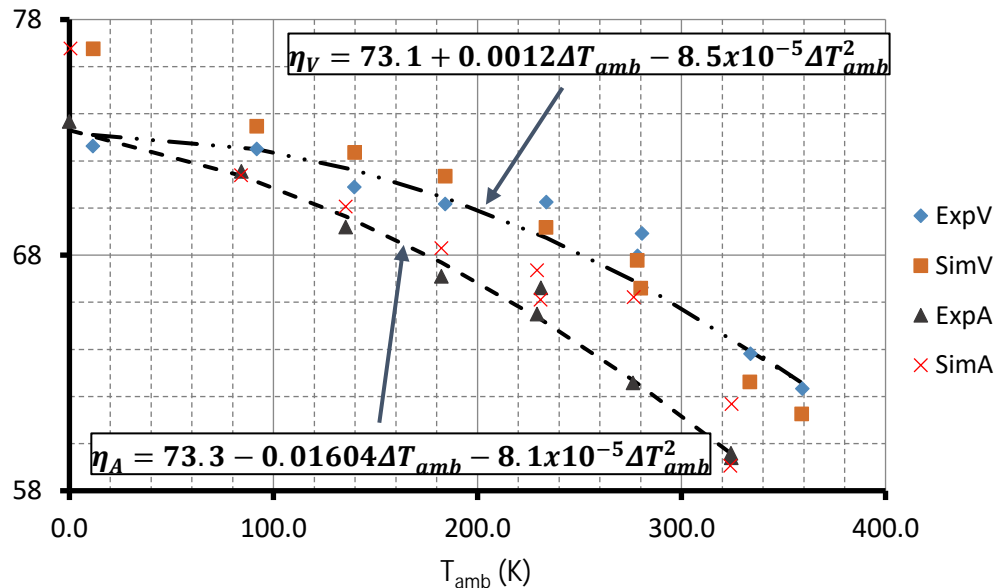


Fig. 4.4 – Efficiency curve for LS-2 using UVAC receiver and Cermet coating

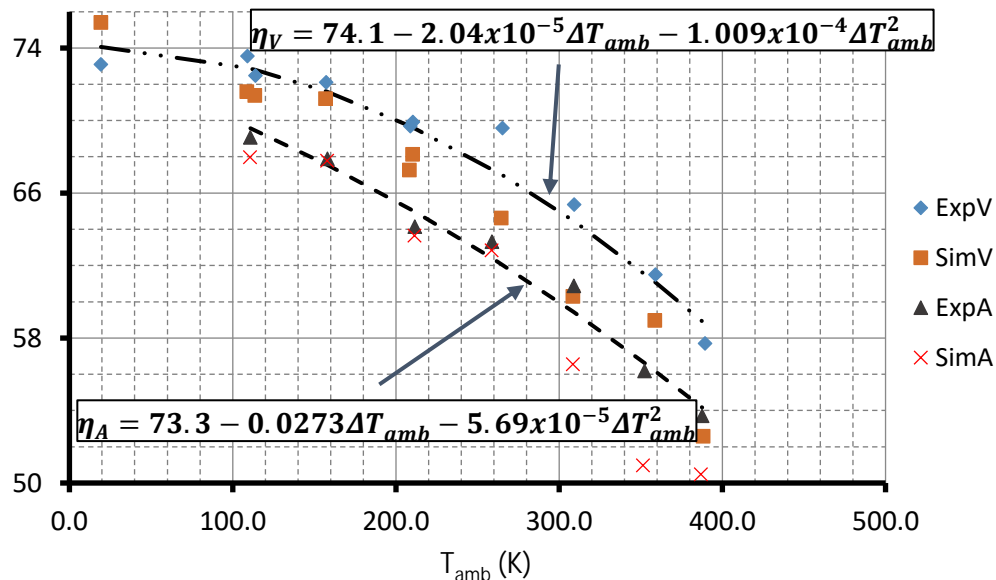


Fig. 4.5 – Efficiency curve for LS-2 using UVAC receiver and Black Chrome coating

Variability of ΔT and thermal efficiency are shown in Figures 4.6 and 4.7 for Cermet and Black Chrome coatings respectively. It is noticed that for Black Chrome coating, simulations tend to be conservative respect to experiments, while there are not high differences using Cermet coating. This behavior could be generated by over-estimation of simulated heat losses to the ambient due to the low ambient temperature of tests with this coating (lower than 6 °C) compared with tests with Cermet coating (higher than 15 °C).

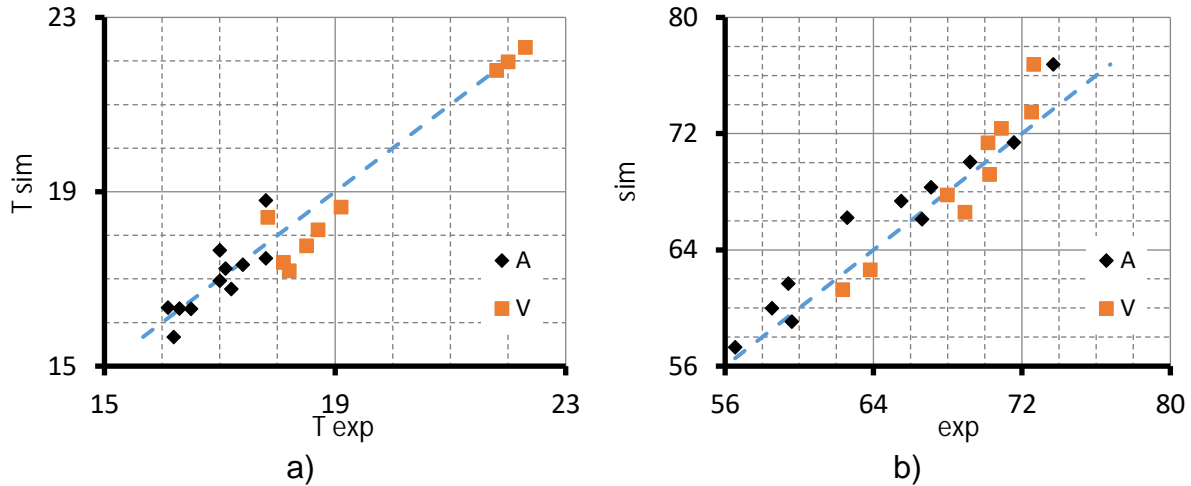


Fig. 4.6 – Comparison of output parameters for LS-2 using UVAC receiver and Cermet coating

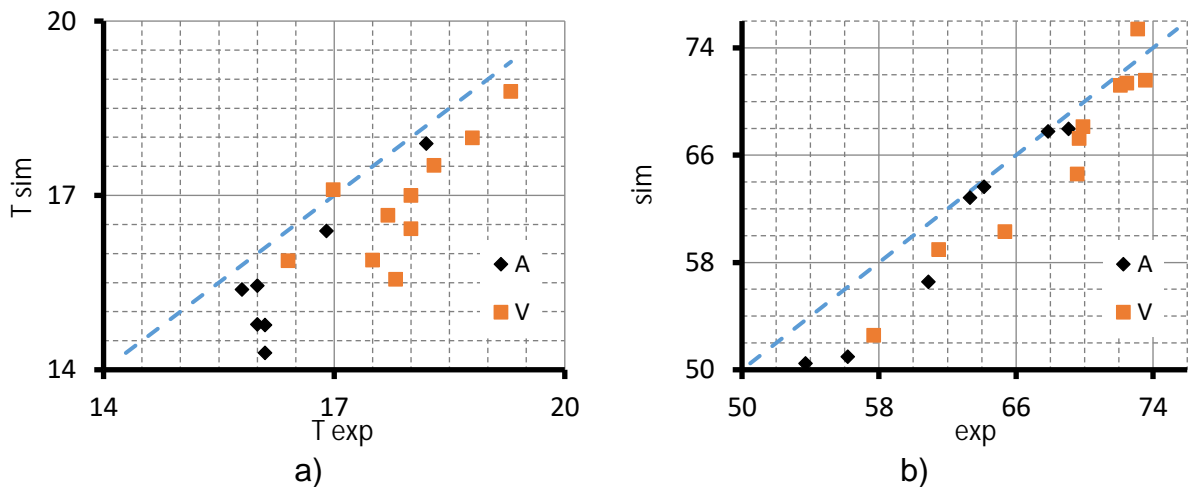


Fig. 4.7 – Comparison of output parameters for LS-2 using UVAC receiver and Black Chrome coating

Figures 4.8 and 4.9 show boxplots, and Tables 4.3 and 4.4 show descriptive statistics or output parameters for LS-2 PTC with UVAC receiver using Cermet and Black Chrome coating respectively. Thermal efficiency with non-evacuated receivers (air in annulus) show higher variability respect to evacuated receivers. It may be caused by the estimation of heat losses by convection in annulus region when it is filled with air. Outlet temperature and temperature differences show an average absolute error of less than 0.4 °C and 0.5 °C for evacuated and non-evacuated receivers respectively with Cermet coating, and these values double when Black Chrome coating is used. Average absolute errors of thermal efficiency are around 1.5% and 2.5% for Cermet and Black Chrome coatings respectively, which they can be comparable with average uncertainties found in experiments (2% for Cermet coating, and $\approx 2.4\%$ for Black Chrome coating). There is a no significant difference in thermal behavior even when there was considered a pipe with a different thickness than other analysis presented in this work.

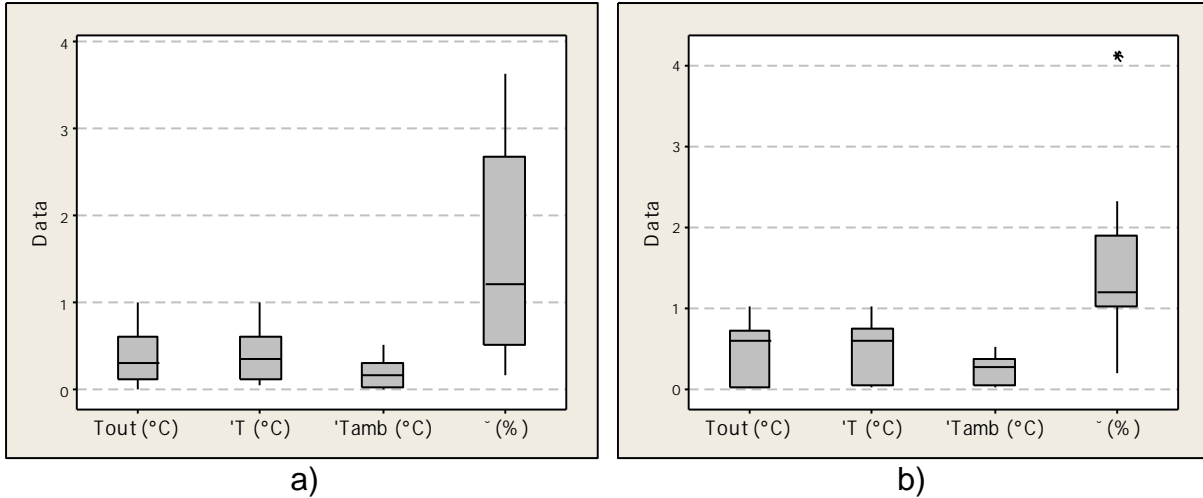


Fig. 4.8 – Absolute errors' boxplots of output parameters for LS-2 with UVAC receiver and Cermet coating. a) Air in annulus, b) Vacuum in annulus.

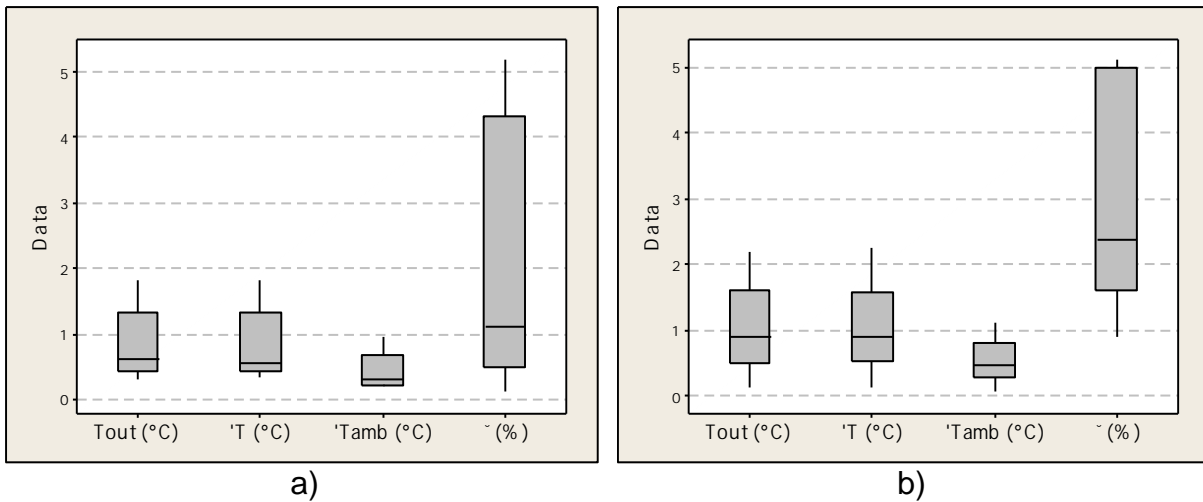


Fig. 4.9 – Absolute errors' boxplots of output parameters for LS-2 with UVAC receiver and Black Chrome coating. a) Air in annulus, b) Vacuum in annulus.

Table 4.3 – Descriptive statistics for absolute errors (LS-2 + UVAC and Cermet)

		T_{out} (°C)	ΔT (°C)	ΔT_{amb} (°C)	η (%)
Air in Annulus	Test range	47.3 – 393.1	16.1 – 17.8	0 – 355.15	56.5 – 73.7
	Min	0	0.04	0	0.16
	Max	1	1	0.4982	3.64
	Average	0.367	0.382	0.184	1.569
	St Dev	0.324	0.312	0.163	1.227
Vacuum in Annulus	Test range	36.17 - 398	17.83 – 22.3	11.5 – 359.3	62.3 – 72.6
	Min	0	0.01	0	0.19
	Max	1	1.01	0.5	4.13
	Average	0.442	0.458	0.228	1.511
	St Dev.	0.367	0.365	0.173	1.126

Table 4.4 – Descriptive statistics for absolute errors (LS-2 + UVAC and Black Chrome)

		T_{out} (°C)	ΔT (°C)	ΔT_{amb} (°C)	η (%)
Air in Annulus	Test range	117.9 – 395.8	15.8 – 18.2	110.9 – 387.7	53.7 – 69.1
	Min	0.3	0.31	0.2	0.1
	Max	1.8	1.81	0.95	5.2
	Average	0.871	0.879	0.450	2.134
	St Dev	0.565	0.572	0.289	2.083
Vacuum in Annulus	Test range	31.8 – 397.4	16.4 – 19.3	19.3 – 389.4	57.7 – 73.6
	Min	0.11	0.11	0.055	0.89
	Max	2.2	2.24	1.1	5.12
	Average	1.011	1.019	0.516	2.813
	St Dev.	0.626	0.631	0.317	1.632

No glass-covered case is different than others. The problem presented in this case is the high over-estimation of heat losses, maybe caused by a combination of high wind velocity (up to 9 m/s), low ambient temperature (below 21 °C), and high inlet temperature (up to 386 °C). In addition, the measured wind speed was taken at an altitude of 10m from the ground and 30m away from test equipment, so wind speed in the surrounding space of receiver should be lower than the measured value. This effect cannot be easily predicted in thermal model since it calculates thermal losses for a horizontal cylinder facing wind in cross-flow (see Section 3.1.7.3), so bare receivers under conditions similar to the found in experiments are not well modeled using the approach presented in this work.

4.1.3 URSSA Trough

Valenzuela et al. [3] reported about outdoor tests realized to an URSSA Trough PTC using a PTR-70 receiver. The collector’s dimensions were around 5.76m aperture x 70m length, and it was tested at Plataforma Solar de Almería. HTF used was Syltherm 800 in all tests. Average measured ambient parameters were 800 – 980 W/m² for direct-beam solar radiation and a quasi-steady flow rate of 15 m³/h. Two test campaigns were realized, one to determine peak thermal efficiency at near-zero incidence, and another with 9 – 30 ° for incidence angle. Simulations were carried out with wind speed of 0 m/s due to test results do not report measured wind speed. Soiling was simulated with a factor $F_c = 0.9$.

Figure 4.10 shows a comparison among experimental, simulated, and thermal efficiency modeled with equation reported in test results. Equation (4.1) is the modeled thermal efficiency of URSSA Trough PTC, which includes the effect of incidence angle, so it does not depend only on ΔT_{amb} as shown in previous sections. It is noticed that simulations tend to be at lower efficiencies than experiments, showing that the approach used in simulations is conservative with respect of the experiments.

$$\eta = 76.8K(\theta)F_c - \frac{2600\Delta T_{amb} + 8.5 \times 10^{-5} \Delta T_{amb}^4}{409.908I_b \cos(\theta)} \quad (4.1)$$

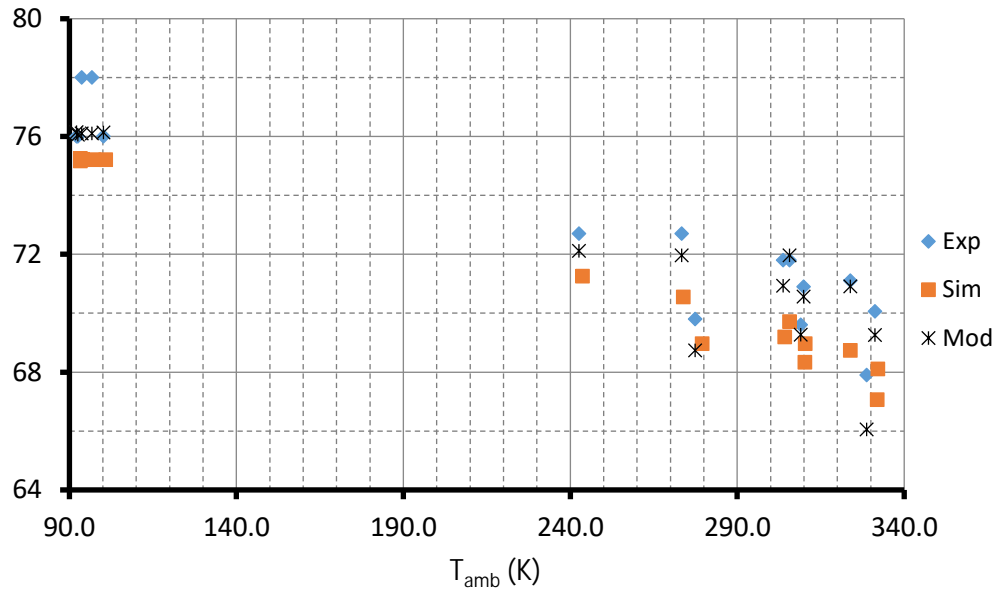


Fig. 4.10 – Efficiency curve for URSSA Trough PTC

Figures 4.11 shows comparison of simulated and experimental output parameters. Figure 4.11 a) shows that the simulations tend to over-estimate temperature difference in collector, while Figure 4.11 b) shows that simulated efficiencies tend to be underestimated. This behavior may be generated by the inclusion of effect of incidence angle on simulations, combined with the effect of simulated wind speed of 0 m/s and soiling.

Boxplots in Figure 4.12 and descriptive statistics in Table 4.5 show that temperature-related parameters have high variability compared with previous simulations. Nevertheless, simulated thermal efficiency has an average of around 1.7%, which is comparable with 1% of reported average difference between calculated and measured thermal efficiency. The outliers found in boxplots are due to high incidence angle of test (around 30°).

Table 4.5 – Descriptive statistics for absolute errors (URSSA Trough)

	T _{out} (°C)	ΔT (°C)	ΔT _{amb} (°C)	η (%)
Test range	143.1 – 379.1	34 – 46.6	92.2 – 331.3	67.9 – 78
Min	0	0.02	0	0.75
Max	6.2	6.21	3.1	2.79
Average	1.773	1.775	0.887	1.697
St Dev	1.616	1.622	0.810	0.771

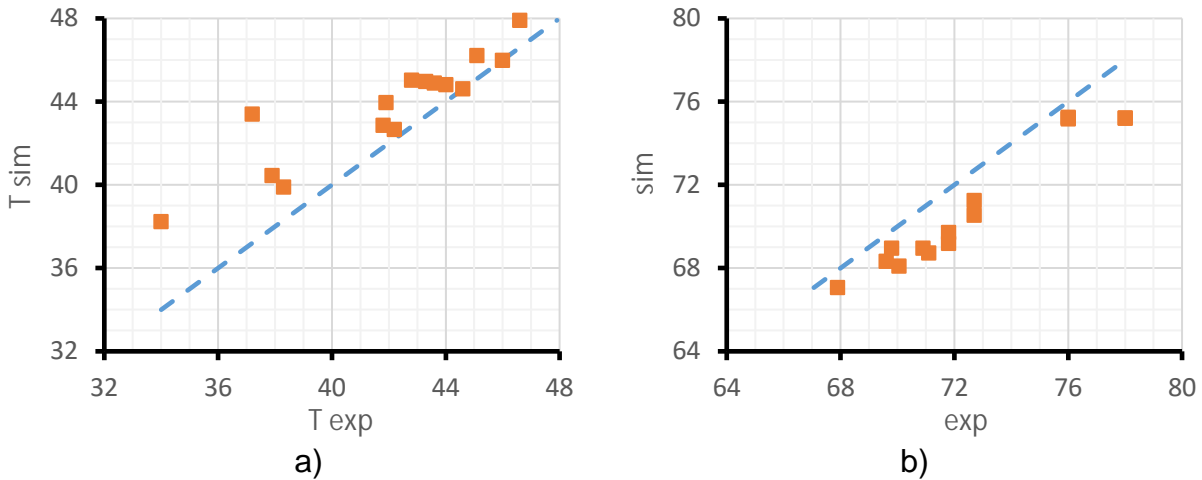


Fig. 4.11 – Comparison of output parameters for URSSA Trough

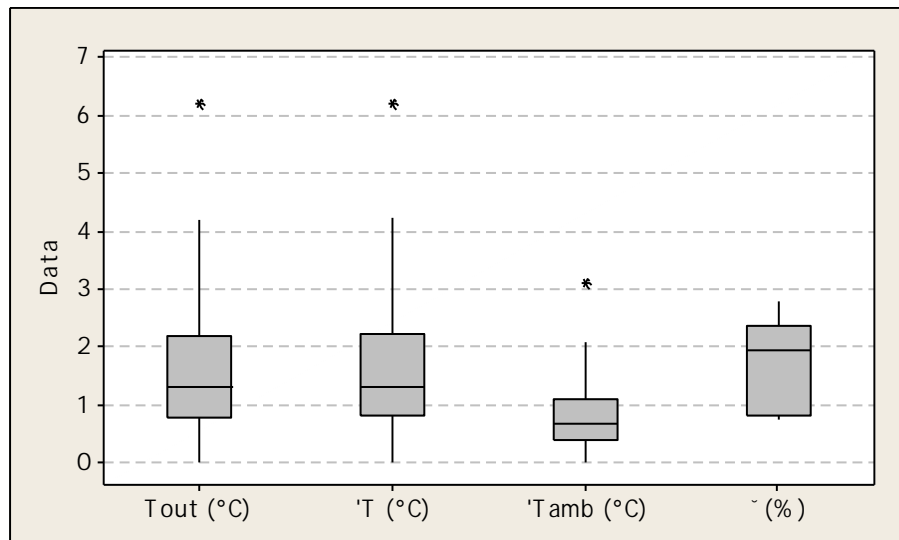


Fig. 4.12 – Absolute errors' boxplots of output parameters for URSSA Trough

4.1.4 CAPSOL

Fernández-García et al. [4] presented thermal efficiency results for a small-aperture PTC. The test facility was installed at Plataforma Solar de Almería, and the basic design of this collector consisted on double cover glass (on aperture area of collector and receiver pipe) with a non-evacuated receiver. The PTC design was 1 m aperture x 2 m length, with a receiver coated with Black Chrome. Tests were carried out at solar radiation of 684 – 975 W/m^2 solar radiation, wind speed of 0.7 – 9 m/s, 45 – 167 $^{\circ}C$ of inlet temperature, and a fixed flow rate of 300 l/h. Pressurized water was used as HTF, were measured pressure were between 1.9 to 20.1 barg.

Figure 4.13 shows a comparison among experiments, simulated data, and reported thermal efficiency equation according to [5]. Similar to previous section, thermal efficiency

equation does not depend only on ΔT_{amb} but also on direct beam radiation, according to (4.2). In this occasion, simulations tend to be quite higher than experiments.

$$\eta = 66.6 - 20 \frac{\Delta T_{amb}}{I_b} - 0.2 \frac{\Delta T_{amb}^2}{I_b} \quad (4.2)$$

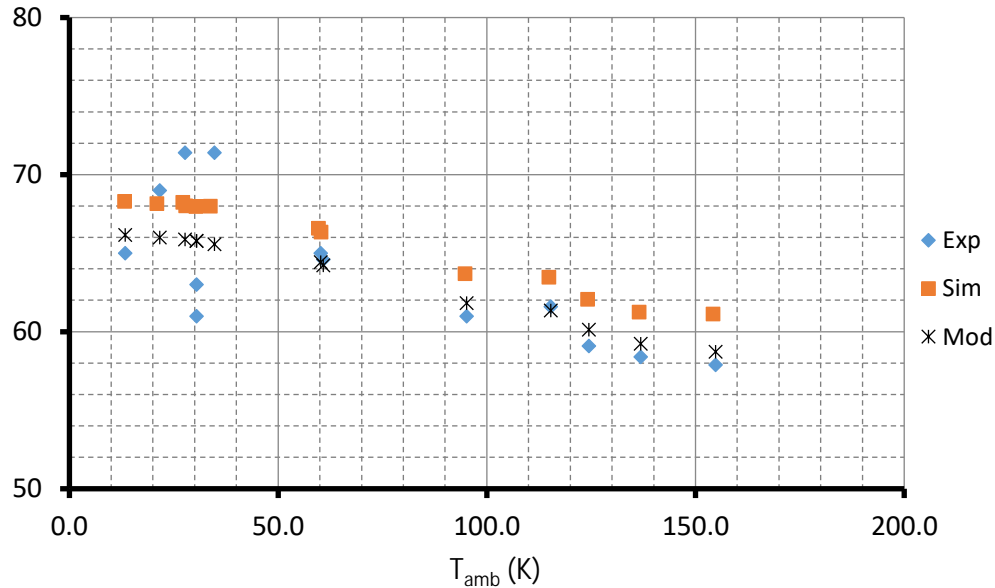


Figure 4.13 – Efficiency curve of CAPSOL PTC

Absolute error data shown in Table 4.5 and boxplots in Figure 4.15 denote a common average of around 1 °C for temperature-related output parameters, while it is obtained an average of 3% for thermal efficiency, which is quite higher than the average uncertainty of 1.9% reported in test results. Figure 4.14 shows that simulated temperature difference in collector are lower than experimental data, while thermal efficiency are commonly higher in simulations. This behavior may be caused by a sub-estimation of heat losses due to the presence of the primary glass cover (aperture area) and the effect of natural convection in the surroundings of the non-evacuated receiver under long-exposure tests.

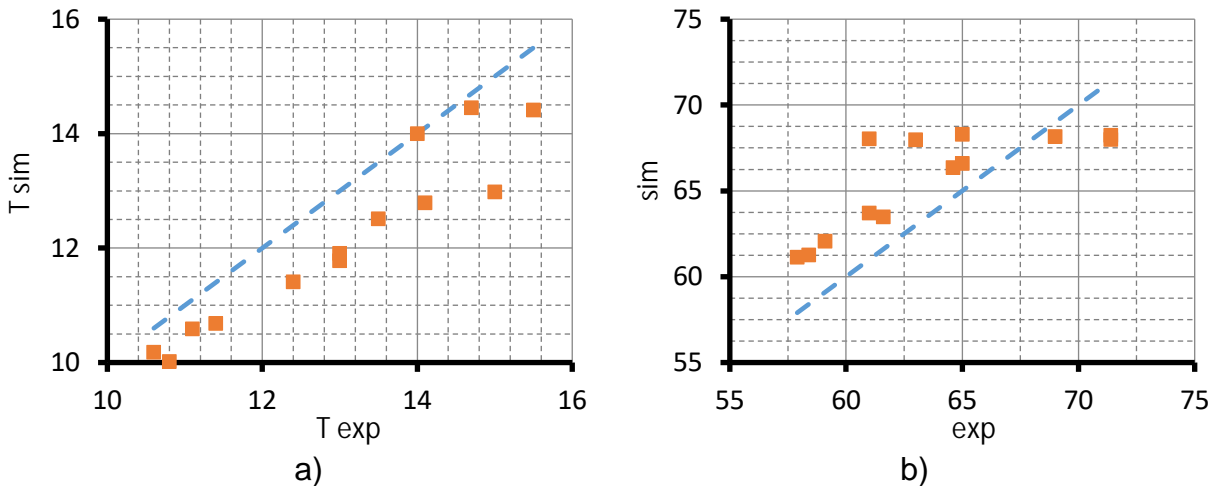


Fig. 4.14 – Comparison of output parameters for CAPSOL

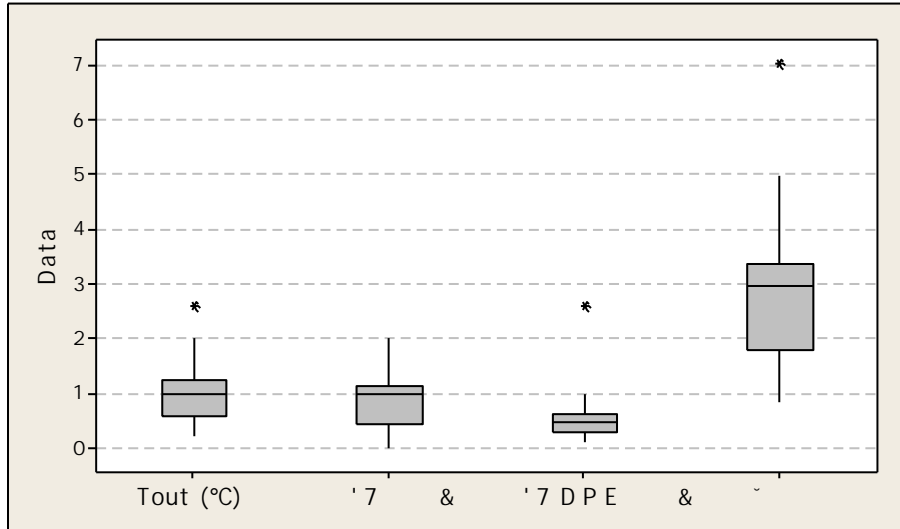


Fig. 4.15 – Absolute errors' boxplots of output parameters for CAPSOL

Table 4.5 – Descriptive statistics for absolute errors (CAPSOL)

	Tout (°C)	ΔT (°C)	ΔTamb (°C)	η (%)
Test range	57.1 – 180.9	10.6 – 15.5	13.4 – 154.8	57.9 – 71.4
Min	0.25	0	0.13	0.84
Max	2.6	2.02	2.6	7.03
Average	1.075	0.876	0.636	3.055
St Dev	0.643	0.522	0.631	1.581

4.2 Case 2: Parabolic trough using nanofluids

Tagle et al. [6] presented a thermal model to determine thermal performance of a PTC using water/Al₂O₃ nanofluid as HTF. The model was validated with experimental data, which were carried out on a small-aperture PTC by Bretado [7]. The collector was PT-110, a PTC designed by Inventive Power®, a mexican enterprise that is developing PTC technology for industrial and commercial processes (temperatures below 250 °C). Design characteristics of PTC used in tests are shown in Table 4.6.

The test facility consisted on a pump, the collector, a heat exchanger, and a storage tank as shown in Figure 4.16. Temperatures (inlet of collector, outlet of collector, and ambient), direct-beam solar radiation, and flow rate were measured in tests. Wind speed was not measured in tests, so a fixed value of 2 m/s was taken in simulations. All tests were performed under an average constant flow rate of 7.53 GPM, and near-normal incidence ($\theta < 10^\circ$). The water/Al₂O₃ nanofluid had a volume-concentration of 1% of suspended 10 nm sized nanoparticles. The output parameters used to compare with experimental data were the same as in previous sections. Simulations were realized using two approaches, as described in Section 3.1.6. These two approaches are denoted as SP (Single-Phase) and NC (Nusselt-Correlation).

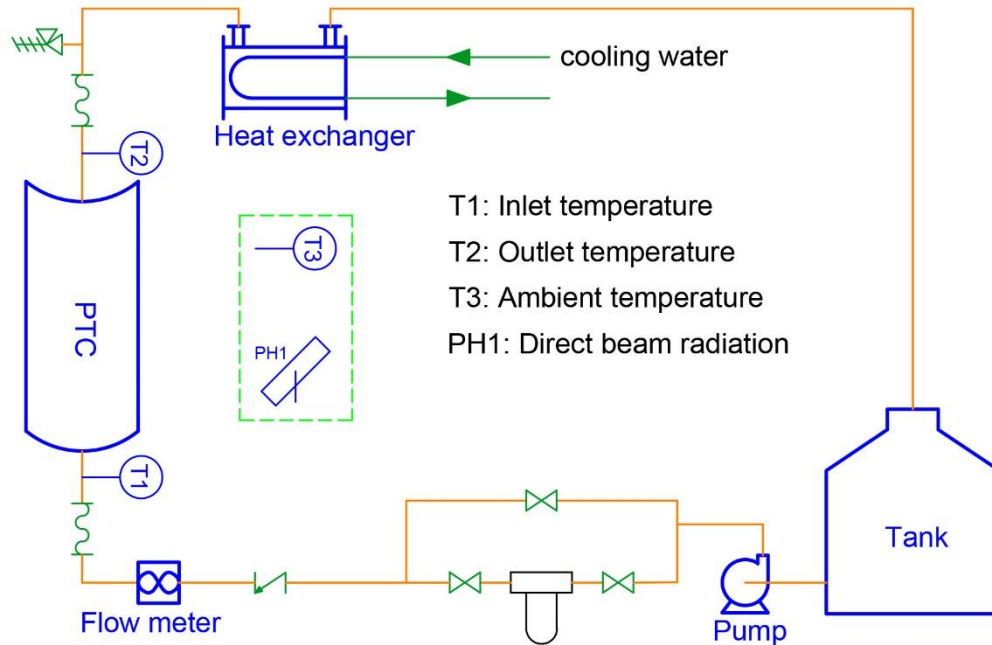


Fig 4.16 – Hydraulic diagram for experimental tests with nanofluids.

Table 4.6 – Characteristics of PT-110

General	Aperture (m)	1.1
	Length (m)	3
	Focal distance (m)	0.34
	γ	0.83
Mirrors	Material	Anodized aluminum sheets
	ρ	0.86
Receiver	Cover glass	Borosilicate, Ø44mm x 2mm thickness
	τ	0.97
	Anti-reflective coating	No
	Evacuated	No
	Tube	AISI 304 1" Sch 40.
	Selective coating	yes
	α	0.87

Table 4.7 shows the comparison of experimental data and simulation results of output parameters. Figure 4.17 shows the experimental data (dots), efficiency curve using lineal regression for experiments (labeled as ExpR), and efficiency curve using linear regression for simulations (labeled as SimR) in a thermal efficiency vs. reduced temperature plot. Average of SP and NC simulations are used to plot simulated thermal efficiency. Equation (4.3) was obtained as thermal efficiency equation due to the quadratic term in regression analysis was statistically neglected using a p-value of 5%. Table 4.8 shows the coefficients of thermal efficiency equation using experimental data, simulations using SP approach, simulations using NC approach, and their respective relative error with coefficients of thermal equation derived using experimental data.

Table 4.7 – Experimental and simulation data comparison for the Al₂O₃-water nanofluid with 1% of volume concentration

Experimental conditions			Experimental results				Simulations (Single-Phase)				Simulations (Nusselt-correlation)			
I (W/m ²)	T _a (°C)	T _{in} (°C)	T _{out} (°C)	Δt (°C)	ΔT _{amb} (°C)	η (%)	T _{out} (°C)	Δt (°C)	ΔT _{amb} (°C)	η (%)	T _{out} (°C)	Δt (°C)	ΔT _{amb} (°C)	η (%)
839.2	43.0	56.3	57.2	0.9	13.7	57.6	57.13	0.83	13.72	58.76	57.14	0.84	13.72	58.79
810.3	31.1	54.1	55.0	0.9	23.4	58.6	54.88	0.78	23.39	57.31	54.89	0.79	23.39	57.34
818.6	30.7	54.8	55.7	0.9	24.6	57.9	55.59	0.79	24.49	57.18	55.59	0.79	24.50	57.21
743.1	30.4	56.4	57.2	0.8	26.4	55.4	57.11	0.71	26.36	56.58	57.11	0.71	26.36	56.61
831.7	31.3	59.1	59.9	0.9	28.2	55.7	59.90	0.80	28.20	56.69	59.90	0.80	28.20	56.72
841.2	30.5	63.0	63.8	0.9	32.9	53.6	63.80	0.80	32.90	56.05	63.80	0.80	32.90	56.08
855.8	39.2	57.6	58.5	0.9	18.9	54.2	58.44	0.84	18.82	58.08	58.44	0.84	18.82	58.11
905.3	38.4	39.2	40.3	1.1	1.4	61.1	40.12	0.92	1.26	60.45	40.12	0.92	1.26	60.48

Table 4.8 – Coefficients thermal efficiency curve for the Al₂O₃-water nanofluid with 1% of volume concentration

Source	o	a
Experiments	60.596	147.77
Simulations (SP)	60.63	115.65
Simulations (NC)	60.66	115.65
Error with SP	0.06%	27.77%
Error with NC	0.11%	27.77%

$$\eta = \eta_0 - aT^* \quad (4.3)$$

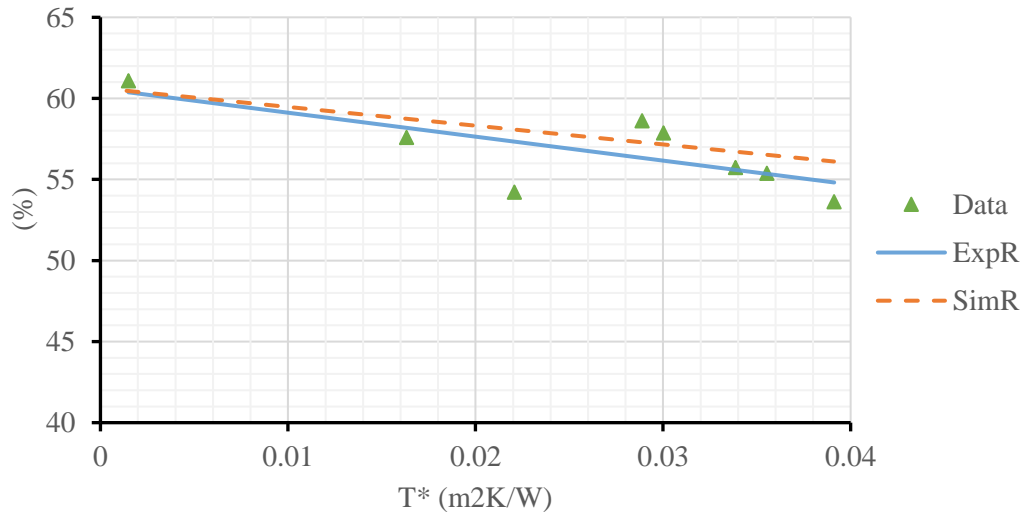


Fig. 4.17 – Efficiency curve of experiments and simulations for the Al₂O₃-water nanofluid with 1% of volume concentration

Data in Tables show that simulations and experiments results are quite similar. Also, simulations are very similar to each other even using different approaches to calculate convective heat transfer coefficient. According to Table 4.8, error of predicting peak thermal efficiency is minimum, while prediction of thermal loss coefficient α tends to show a higher error. This may be caused by the assumption a constant cross-flow wind in receiver compared to the unknown experimental values. Other source of error can be the uncertainty of instrumentation used to measured temperatures combined with small temperature differences obtained in experiments.

Descriptive statistics shown in Table 4.9 denote low level of errors between simulations and experiments. It is important to notice that the range of experimental outlet temperatures can be considered as “small”, which can generate higher error if it is scaled. Nevertheless, even with high uncertainties of measured temperatures due to thermocouples used, simulated thermal efficiency has an average error comparable with previous experiments presented in this work.

Table 4.9 – Descriptive statistics for absolute errors (PT-110 with nanofluid as HTF)

	T _{out} (°C)	ΔT (°C)	ΔT _{amb} (°C)	η (%)	
Test range	40 - 64	0.8 – 1.1	1.4 – 32.9	53.6 – 61.1	
SP	Min	0.04	0.04	0.01	0.63
	Max	0.16	0.14	0.09	3.86
	Average	0.08	0.09	0.05	1.53
	St Dev	0.04	0.03	0.03	1.10
NC	Min	0.04	0.04	0.01	0.60
	Max	0.16	0.13	0.09	3.89
	Average	0.08	0.09	0.05	1.54
	St Dev.	0.04	0.03	0.03	1.11

4.3 Case 3: Direct steam generation

Validation with experimental data of a Direct Steam Generation (DSG) plant was realized to test thermo-hydraulic prediction of the model under phase-change conditions. Simulated test facility was the Direct Solar Steam (DISS) plant located at Plataforma Solar de Almería (PSA), which is composed of a 500 m length solar steam generator. The pilot plant can generate steam up to 400 °C and 100 barg, with a maximum thermal power of around 2 MW_{th} [8]. Figure 4.18 shows a schematic diagram of the DISS plant. The thermal loop consisted on a solar boiler with eleven modified LS-3 collectors, nine are 50 m length and two 25 m length (#9 and #10), as shown in Figure 4.18. The solar field can operate at any of the three DSG modes (once-trough, recirculation, and injection), but simulations for validation were carried out only at once-trough mode.

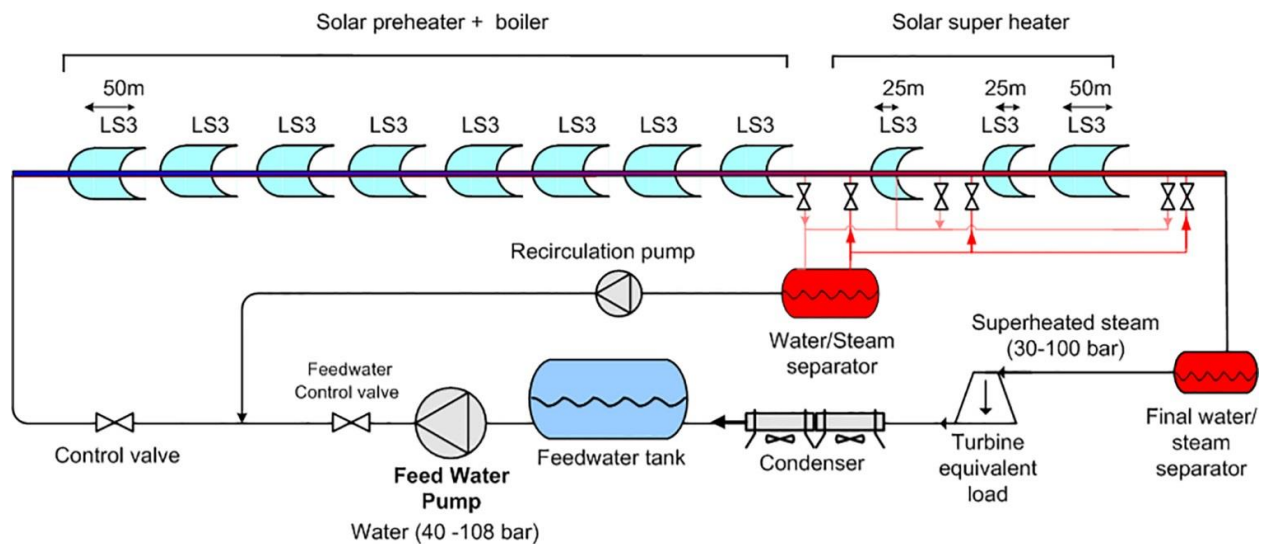


Fig. 4.18 – Schematic diagram of DISS facility loop (PSA).

Table 4.10 shows the principal design characteristics of LS-3 collectors used in simulations. The thermal model cannot simulate different interconnecting piping, so average sizes are considered in analysis. Geometry and accessories of interconnections are described in detail in [9,10], which gives average values of 11.64 m for geometrical length, 28.10 m for hydraulic length, and +0.423 m for height. A 50.8 mm thickness of insulation is considered in heat transfer analysis in interconnecting piping.

Thermocouples and differential pressure transmitters are located near the middle of the interconnecting piping. The results of the simulations at the end of each interconnection are considered in order to compare with experimental data. Coplanar absolute and differential pressure transmitters have an uncertainty of 0.6 barg and 0.04 barg respectively, and thermocouples have a nominal accuracy of ± 2 °C [10].

Table 4.10 – Characteristics of LS-3 collector

General	Aperture (m)	5.76
	Length (m)	50, 25 (#9, #10)
	Focal distance (m)	1.71
	Optical efficiency	0.657*
Mirrors	Material	Silvered glass mirror
	ρ	0.94
Receiver	Model	UVAC
	Cover glass	Borosilicate
	τ	0.96
	D ₅ (mm)	115
	D ₄ (mm)	108
	Pipe	ASTM A335 P22
	D ₃ (mm)	70
	D ₂ (mm)	50
	Selective coating	UVAC Cermet
	ε @ 400°C	0.15
	α	0.95

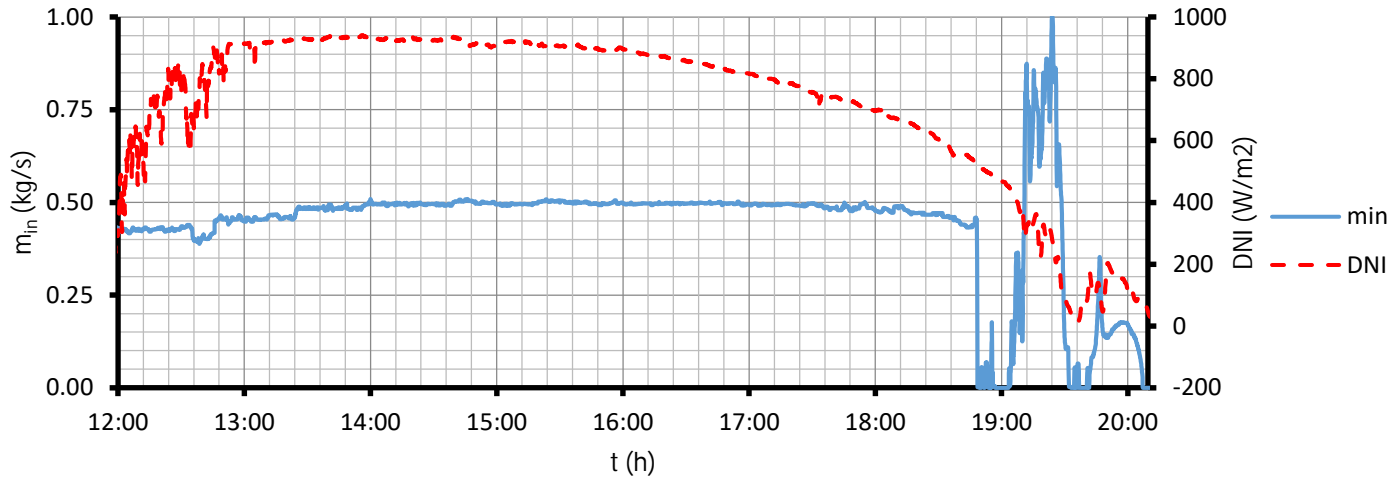
* Soiling and other factors included

Three days of tests were analyzed, where steady-state conditions of inlet mass flow, temperature, and pressure are under quasi-constant rate. Figures 4.19 to 4.21 show inlet temperature/pressure and inlet mass flow/direct beam radiation vs. time of the solar field of the days selected. Table 4.11 shows temporal intervals considered as steady state of inlet mass flow, pressure and temperature. Collector #11 operated in injection mode during the tests, so it is not considered in the analysis.

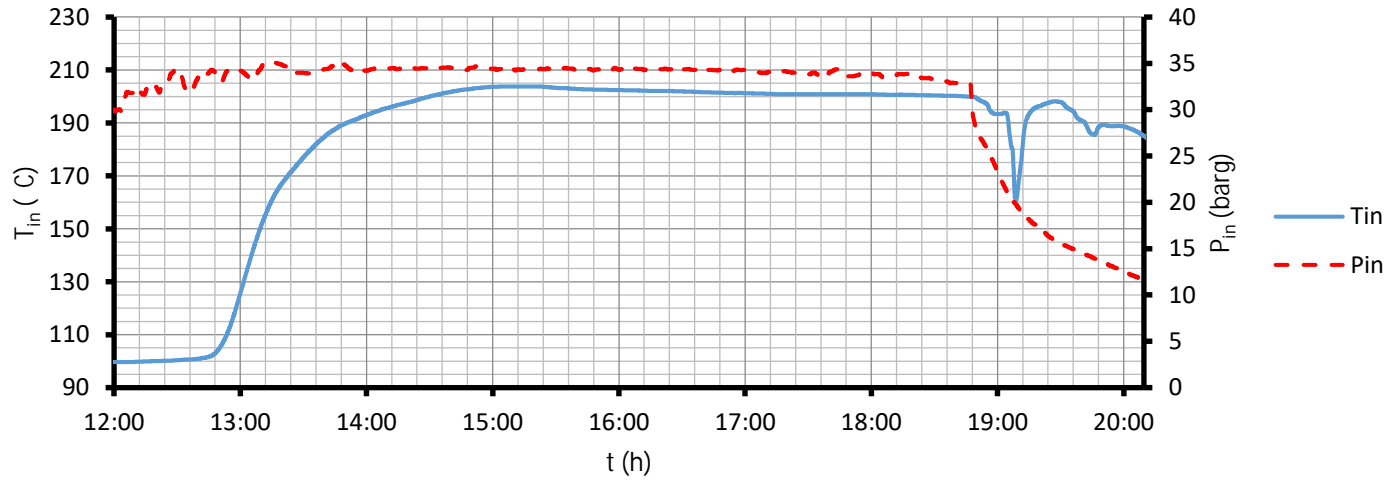
Table 4.11 – Steady-state temporal intervals

Date	Time
02/Apr/2001	From 15h30 to 18h30
13/May/2001	From 13h30 to 15h30
15/May/2001	From 14h00 to 17h00

Eight cases of an average 5-min time lapse of continuous operation are simulated. Table 4.12 shows operational and ambient data used in each simulation. The incidence angle was calculated for a PTC in E-W tracking according to time, date and location. Figures 4.22 to 4.24 show inlet temperature and inlet pressure profiles of each collector for each case. Simulations are solid lines, while experimental data are dots in all cases. Furthermore, simulated inlet vapor quality is shown in all cases (dotted line). It is noticed that experimental and simulations has good agreement in both temperature and pressure, except for pressure at high vapor quality (approximately higher than 0.7). This disagreement is not well noticed in cases 4 to 8 due to a failure in measuring pressure drop at collector #6. This disagreement can be caused by the combination of the quality of mathematical model used for predicting pressure drop and the uncertainty of the differential pressure transmitters.

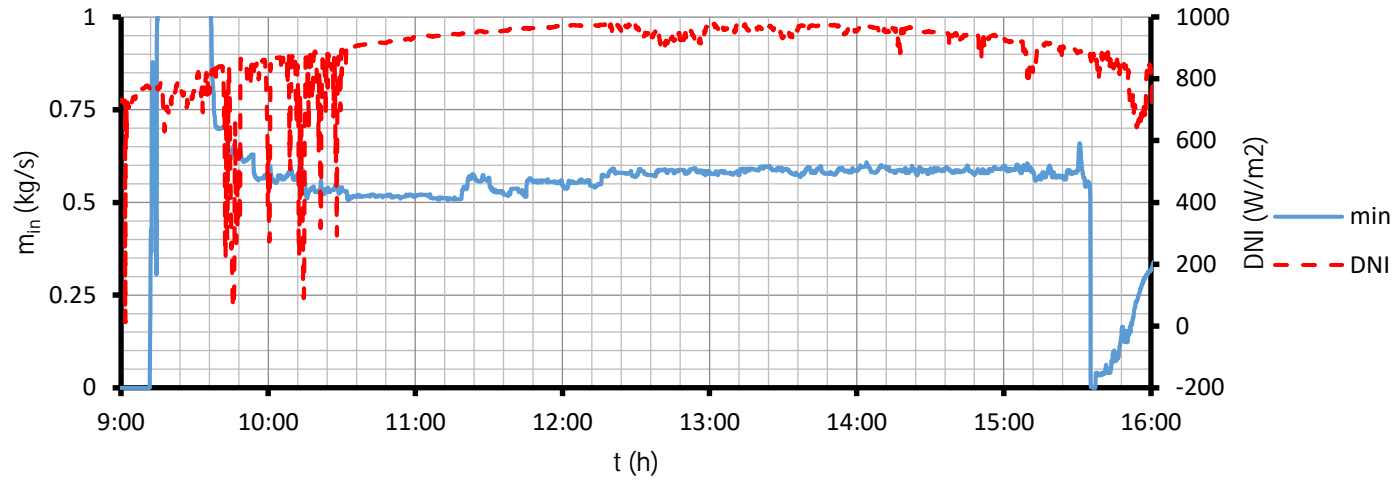


a)

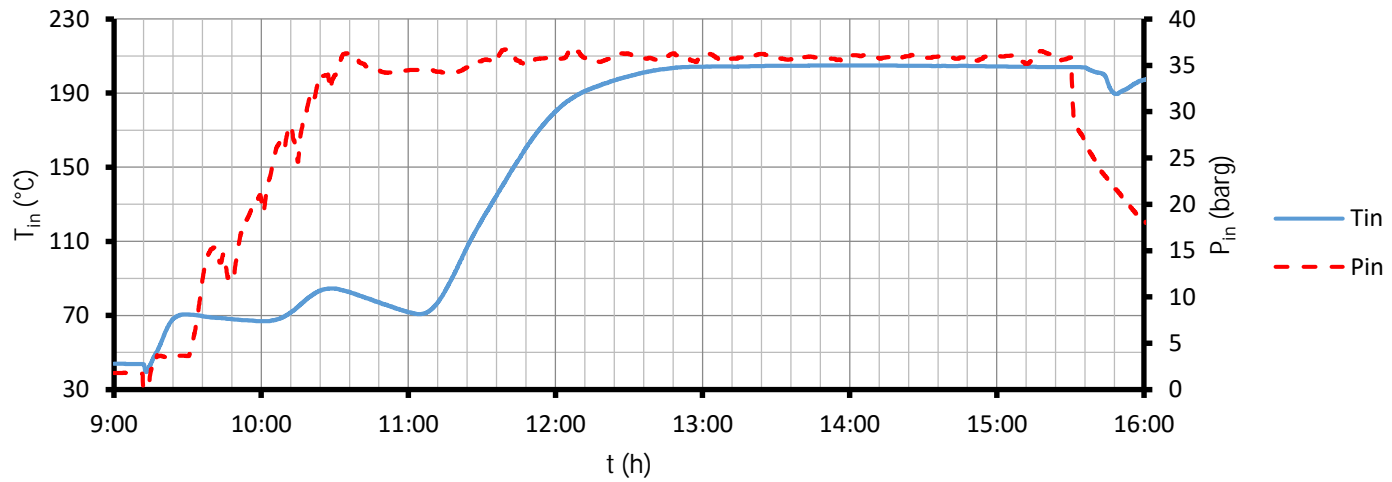


b)

Fig. 4.19 – Operational conditions of the DISS plant at 2/April/2001

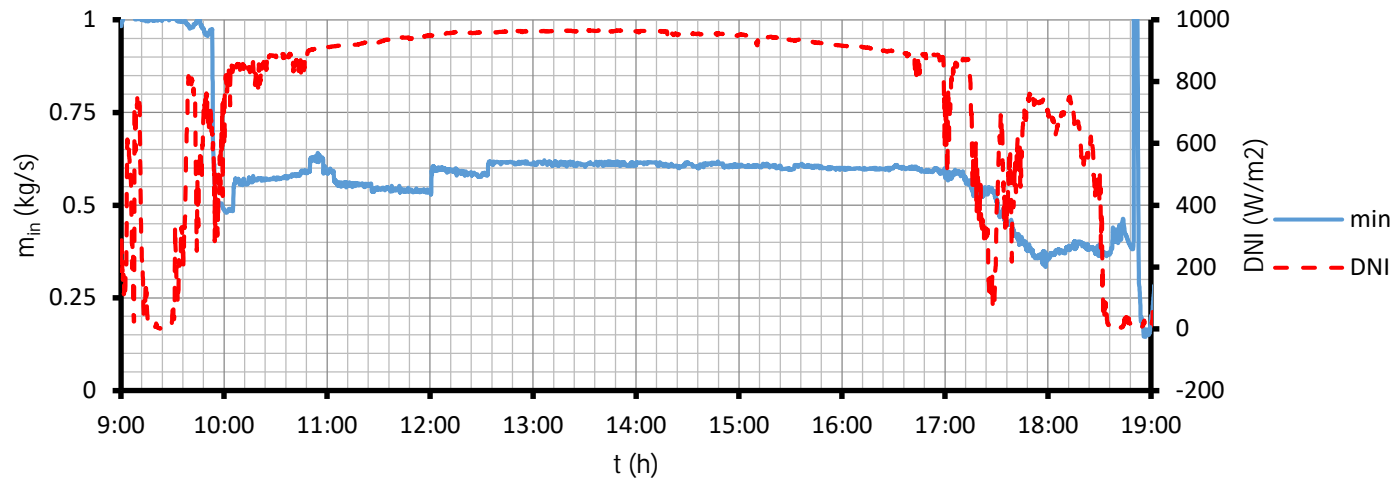


a)

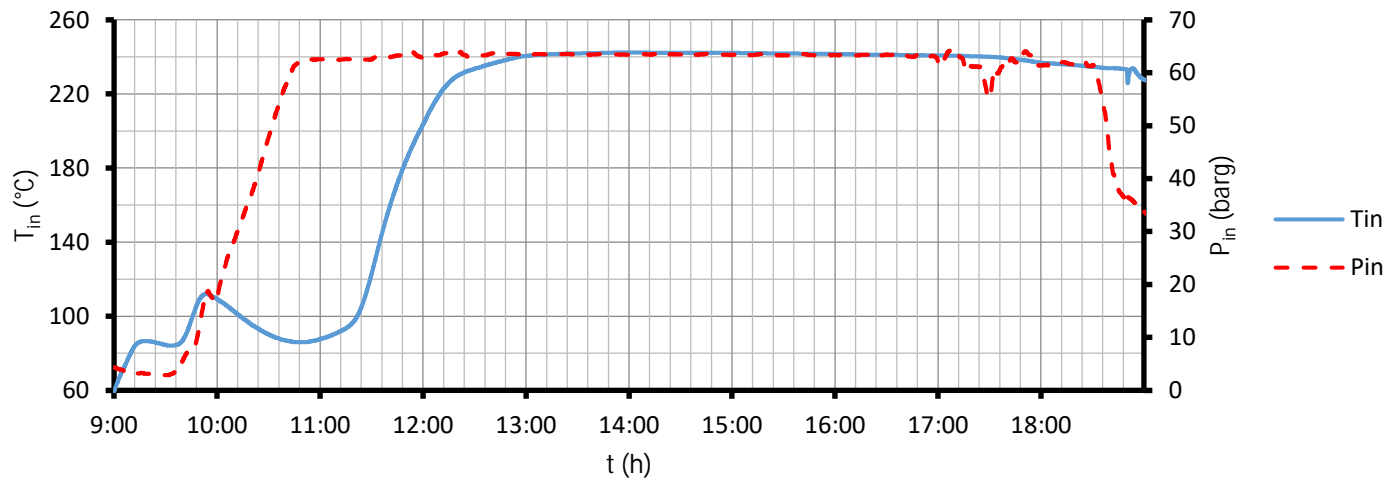


b)

Fig. 4.20 - Operational conditions of the DISS plant at 13/May/2001



a)



b)

Fig. 4.21 – Operational conditions of the DISS plant at 15/May/2001

Table 4.12 – Resume of operational conditions for simulations

subcase	Date	Time	θ (°)	I_b (W/m ²)	T_a (°C)	T_{in} (°C)	P_{in} (barg)	m (kg/s)
a	2/April	16h	27.86	890	24.2	202.33	34.35	0.496
b		17h	22.14	820	23.9	201.26	34.28	0.495
c		18h	14.85	696	22.7	200.73	33.83	0.478
d	13/May	13h45	18.52	970	27.8	204.83	35.89	0.587
e		14h30	18.68	955	27.7	204.70	35.96	0.586
f		15h	18.1	936	28.4	204.41	36.07	0.591
g	15/May	14h	18.24	963	31.5	242.30	63.45	0.614
h		15h	17.45	951	29.9	242.09	63.42	0.605

Tables 4.13 and 4.14 shows the absolute error between simulations results and experimental data for inlet and pressure drop respectively. The effect of interconnecting piping is included in pressure drop calculation. It is noticed that for temperature, the precision is high, and most of the simulations results are within the uncertainty of the thermocouples. However, the error in pressure drop becomes higher at the last collectors of the system (when the vapor quality is high), with a given error up to 7.5 times the uncertainty of the differential pressure transmitters.

Table 4.13 – Error in inlet temperature between experiments and simulations (°C)

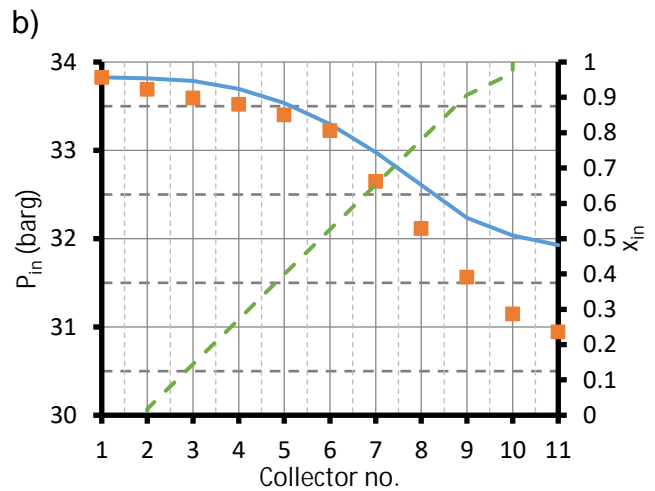
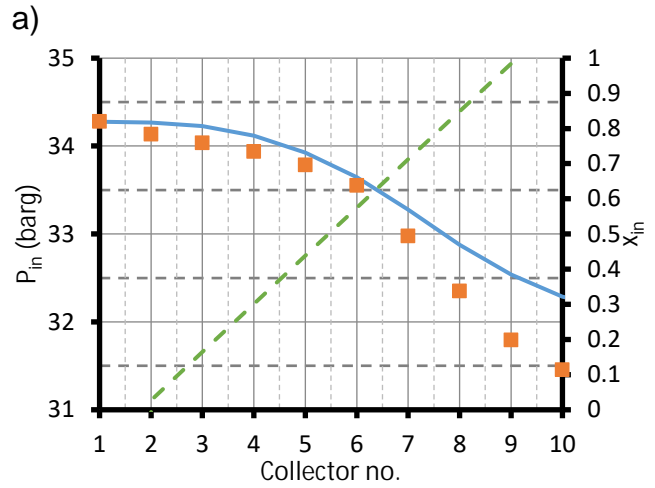
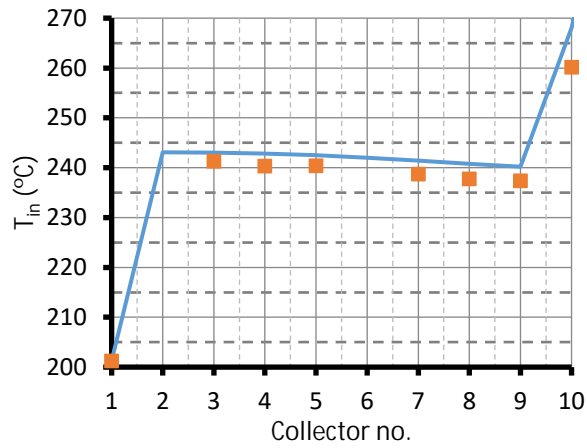
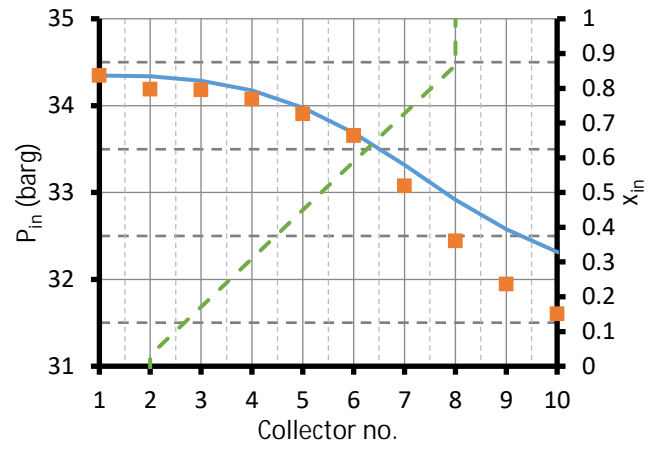
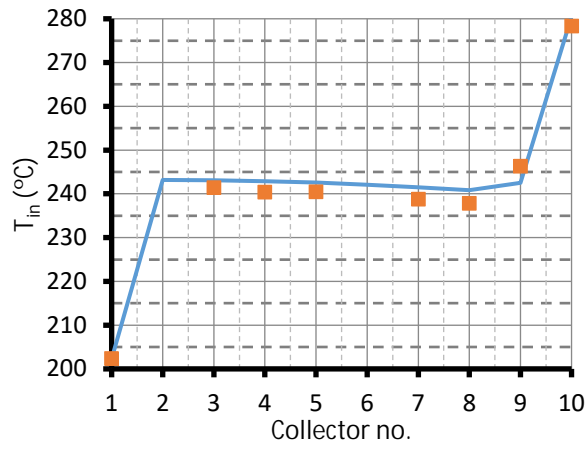
subcase	Collector #									
	1	2	3	4	5	6	7	8	9	10
a	0.03	*	1.70	2.48	2.14	*	2.71	2.96	3.80	2.23
b	0.04	*	1.69	2.46	2.12	*	2.65	3.01	2.85	7.91
c	0.03	*	1.21	2.16	1.88	*	2.27	2.34	2.33	1.89
d	0.03	*	1.92	2.62	2.16	*	2.94	3.06	0.01	6.60
e	0.10	*	1.81	2.54	2.10	*	2.87	2.97	2.84	6.20
f	0.01	*	2.16	2.94	2.44	*	3.18	3.33	4.44	8.85
g	0.00	1.89	1.60	2.48	1.74	*	2.15	2.10	3.31	0.43
h	0.01	2.00	1.60	2.50	1.80	*	2.30	2.20	1.78	6.17

* Failure in measurement

Table 4.14 – Error in pressure drop between experiments and simulations (barg)

subcase	Collector #									
	1	2	3	4	5	6	7	8	9	10
a	0.15	0.04	0.00	0.03	0.04	0.21	0.23	0.16	0.08	0.05
b	0.13	0.05	0.01	0.04	0.05	0.21	0.22	0.22	0.09	0.04
c	0.12	0.06	0.01	0.04	0.06	0.26	0.16	0.18	0.21	0.09
d	0.14	0.06	0.02	0.03	0.03	*	0.10	0.29	0.13	0.12
e	0.14	0.06	0.02	0.03	0.03	*	0.10	0.30	0.13	0.12
f	0.14	0.06	0.01	0.02	0.02	*	0.10	0.29	0.12	0.11
g	0.13	0.05	0.01	0.04	0.06	*	0.01	0.14	0.08	0.04
h	0.14	0.05	0.01	0.04	0.06	*	0.01	0.13	0.08	0.04

* Failure in measurement



c)
 Fig. 4.22 – Comparison of simulated and experimental temperature / pressure profiles (2/Apr). a) 16h, b) 17h, c) 18h

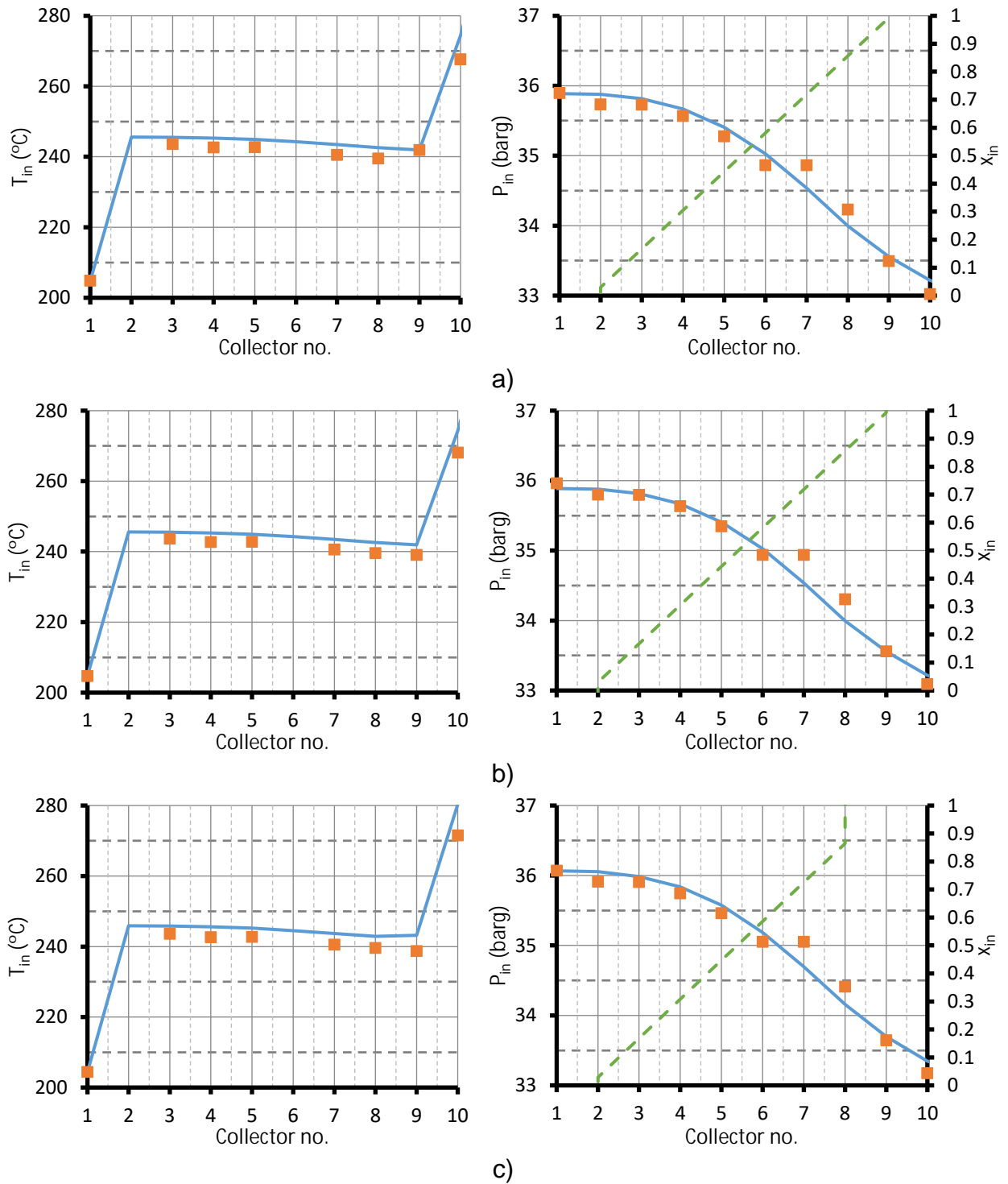


Fig. 4.23 – Comparison of simulated and experimental temperature / pressure profiles (13/May). a) 13:45h, b) 14:30h, c) 15h

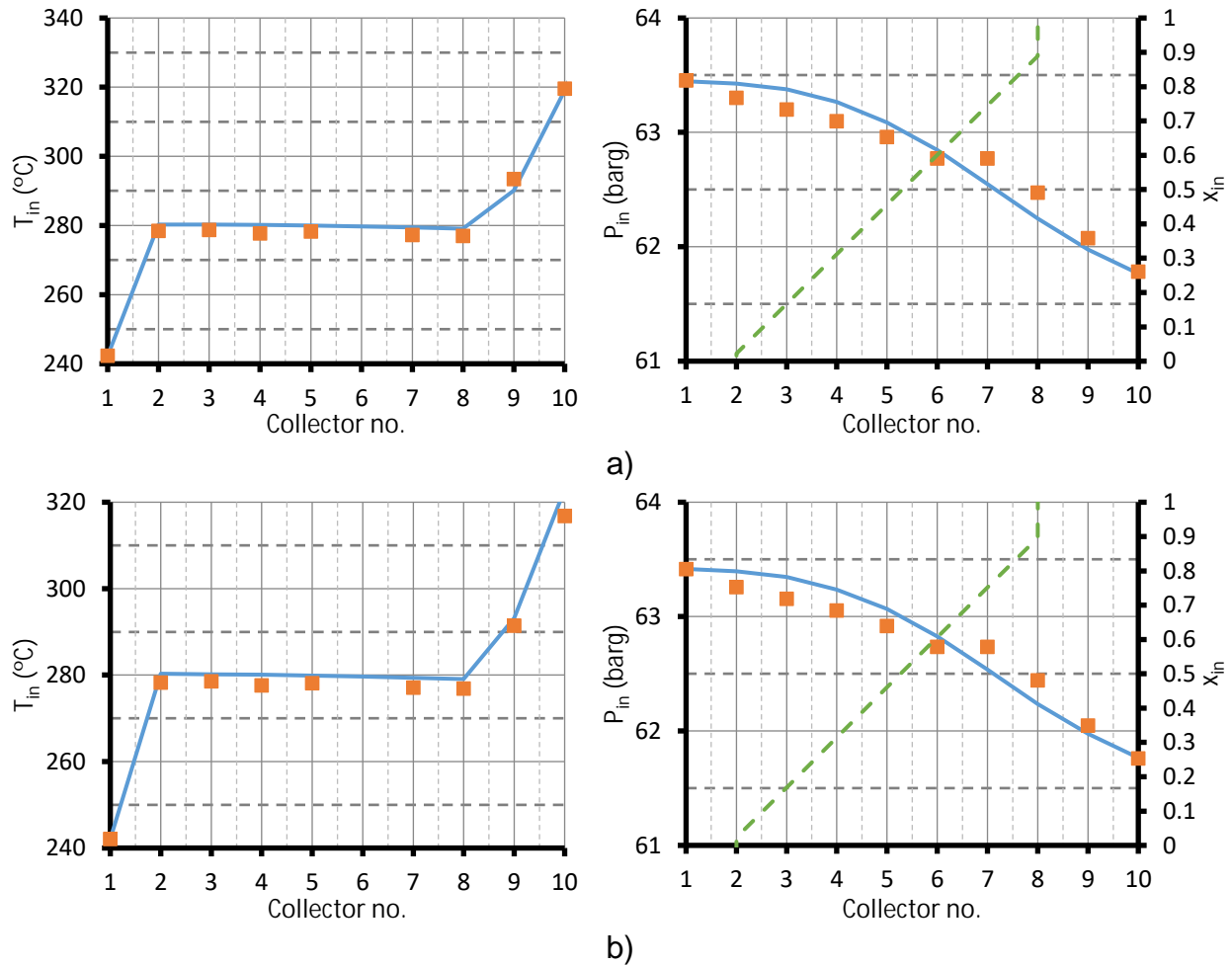


Fig. 4.24 – Comparison of simulated and experimental temperature / pressure profiles (15/May). a) 14h, b) 15h

Table 4.15 shows statistical results of absolute errors and 95% confidence interval error. It is noticed that the uncertainty of temperature is included into the CI for absolute error of simulated temperature, while for simulated pressure drop the uncertainty is lower than the inferior limit of the CI. In resume, mean absolute error for temperature is 2.1 ± 0.29 °C, and 0.1 ± 0.02 barg for pressure drop with a confidence of 95%.

Table 4.15 – Statistics of absolute errors

	Temperature (°C)	Pressure drop (barg)
No. Data	66	75
Minimum	0	0
Maximum	8.85	0.30
Average	2.41	0.09
Std. Deviation	1.71	0.08
95% CI error	0.42	0.02

4.4 Case 4: Estimation of thermal power for steam generation in a dairy plant

Tagle et al. [11] realized a pre-design analysis of a DSG system for steam supply to an industrial process in a dairy plant at Jalisco (Mexico). The factory uses steam for heating of fresh milk and other processes. The principal function of the solar field is to boil water and supply saturated steam to the factory. The requirement of the plant is a saturated-steam flow of 2 Ton/h (approximately 0.56 kg/s). The land area available to install the solar field is 4200 m².

Due to a lack of an in-situ weather station, weather data was taken from a station located in Guadalajara, which is geographically near of the location of the dairy plant [12]. Ulloa et al. [13] realized a study about weather data in big cities. Combining both sources, range of weather data used in simulations were: 800 – 1000 W/m² for solar radiation, 1 – 6 m/s for wind speed, and 11 – 32 °C for ambient temperature. Inlet temperature of water was simulated between 70 °C to 100 °C, which is the temperature of cold water in the process.

The collector used in simulations was the PT250 from Inventive Power ®. Table 4.16 shows the characteristics of the PTC used in simulations. Solar field consisted on nineteen lines, eight collectors each (152 collectors in total). Interconnecting piping are assumed as with the same pipe of the receiver, with four 90° elbows and a globe valve as fittings. Receivers are evacuated according to the datasheet.

Table 4.16 – Characteristics of PT250 collector.

General	Aperture (m)	2.5	Receiver	Model	Seido 6-1
	Length (m)	4		Cover glass	Borosilicate
	Focal dist. (m)	0.83		Transmittance	0.96
	Opt. Eff.	0.66*		D. pipe x e (mm)	40 x 2
Mirrors	Material	Anodized Al.	D. Cov. x e (mm)	102 x 2	
	Reflectance	0.86	Absorptance	0.96	

* estimated

Figure 4.25 shows a schematic diagram of the plant to be simulated. Operational conditions are: inlet condensates at 0 barg and 70 - 100 °C (previous to pressurization), outlet steam at 7 barg, and separator at outlet pressure of the solar field. The expansion valve is used in case the pressure at the tank is greater than the required pressure in the process. The minimum outlet pressure in simulations is 8 barg, which considers 1 barg as estimated pressure drop from the manifold to the process.

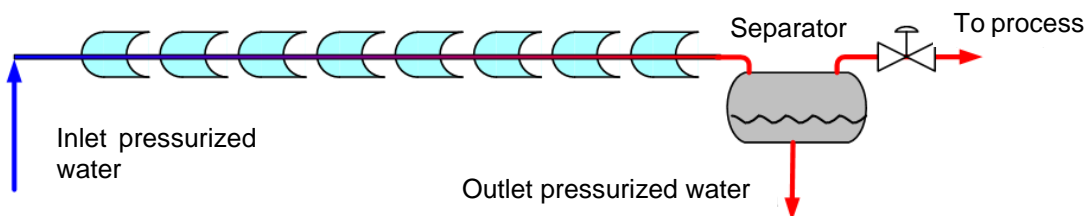


Fig. 4.25 – Schematic diagram of solar field

Sensitivity analysis of outlet conditions of the solar field under variation of the weather conditions shows that ambient temperature and wind velocity does not affect pressure drop nor outlet temperature, but solar radiation does affect outlet pressure. Figure 4.26 shows variation of the outlet pressure of the steam before it enters separation tank. It is noticed that the higher solar radiation, the lower outlet pressure. This affects directly to the outlet steam quality of the solar field. Due to the required steam conditions at the process, simulations were carried out with a solar radiation of 1000 W/m² to design the system under the lower possible outlet pressure conditions.

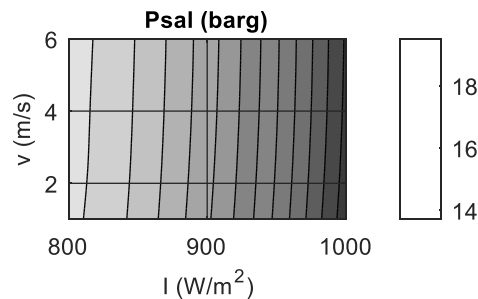


Fig. 4.26 – Outlet pressure for a flow rate of 9 GPM, inlet pressure of 25 barg, and ambient temperature of 18 °C.

Another sensitivity analysis, varying inlet conditions (pressure, temperature, and flow rate), is done in order to select operational conditions to assure the required minimum outlet pressure. The solar field was simulated under conditions of inlet pressure in the range of 20 – 30 barg, inlet temperature of 70 – 100 °C, and flow rate between 8 – 16 GPM. Figure 4.27 shows the limits where outlet pressure is 8 barg, and Table 4.17 shows the results of simulations for outlet conditions before the separation tank. All conditions over the continuous line in Figure 4.27 covers the required outlet pressure of the system. The selected condition is at a flow rate of 12 GPM and inlet pressure of 25 barg, where the results shows an acceptable outlet pressure in the range of inlet temperature.

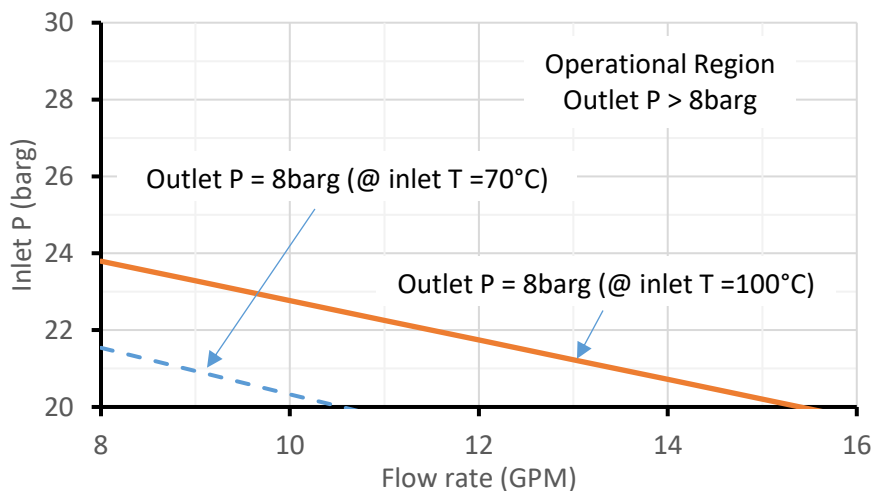


Fig. 4.27 – Selection of operational region of solar field.

Table 4.17 – Variation of outlet conditions.

T (°C)	Inlet conditions		Outlet conditions		
	P (barg)	G (GPM)	P _{out} (barg)	T _{out} (°C)	x
100	30	8	18.23	210.5	0.707
		12	21.64	218.8	0.386
		16	24.36	224.8	0.215
	25	12	12.76	194.3	0.415
		16	17.15	207.6	0.246
70	30	8	21.03	217.4	0.628
		12	24.79	225.7	0.303
		16	26.44	229	0.134
	25	8	12.46	193.3	0.64
		12	17.88	209.5	0.329
		16	20.63	216.4	0.161
	20	12	8.145	176.1	0.369
		16	13.707	197.4	0.197

Using regression analysis, there was obtained Equations (4.4) to (4.6), which determine maximum supplied mass flow rate of steam after separation tank (\dot{m}_x in kg/s), thermal power of solar field (Pot_{sal} in kW_{th}), and over-heating temperature difference (ΔT in °C) as function of the direct beam radiation and inlet temperature. Figure 4.28 shows level curves for these parameters over the range of solar radiation and inlet temperature used in simulations. Temperature difference ΔT is caused by the effect that the outlet steam of the solar field is slightly overheated respect to its saturation temperature. These equations are valid all over the range of 800 – 1000 W/m² for solar radiation and 70 – 100 °C for inlet temperature. Maximum supplied mass flow rate to the process is from 0.133 kg/s to 0.301 kg/s, which represents between 23.75% to 53.75% of the required steam.

$$\dot{m}_x = -0.4453 + 1.879 \cdot 10^{-3} \cdot T + 5.575 \cdot 10^{-4} \cdot I; R^2 = 0.999 \quad (4.3)$$

$$Pot_{sal} = 68.739 - 0.534 \cdot T + 0.874 \cdot I; R^2 = 0.998 \quad (4.4)$$

$$\Delta T = -0.063 \cdot T + 0.053 \cdot I - 3.732 \cdot 10^{-5} \cdot I^2; R^2 = 0.998 \quad (4.5)$$

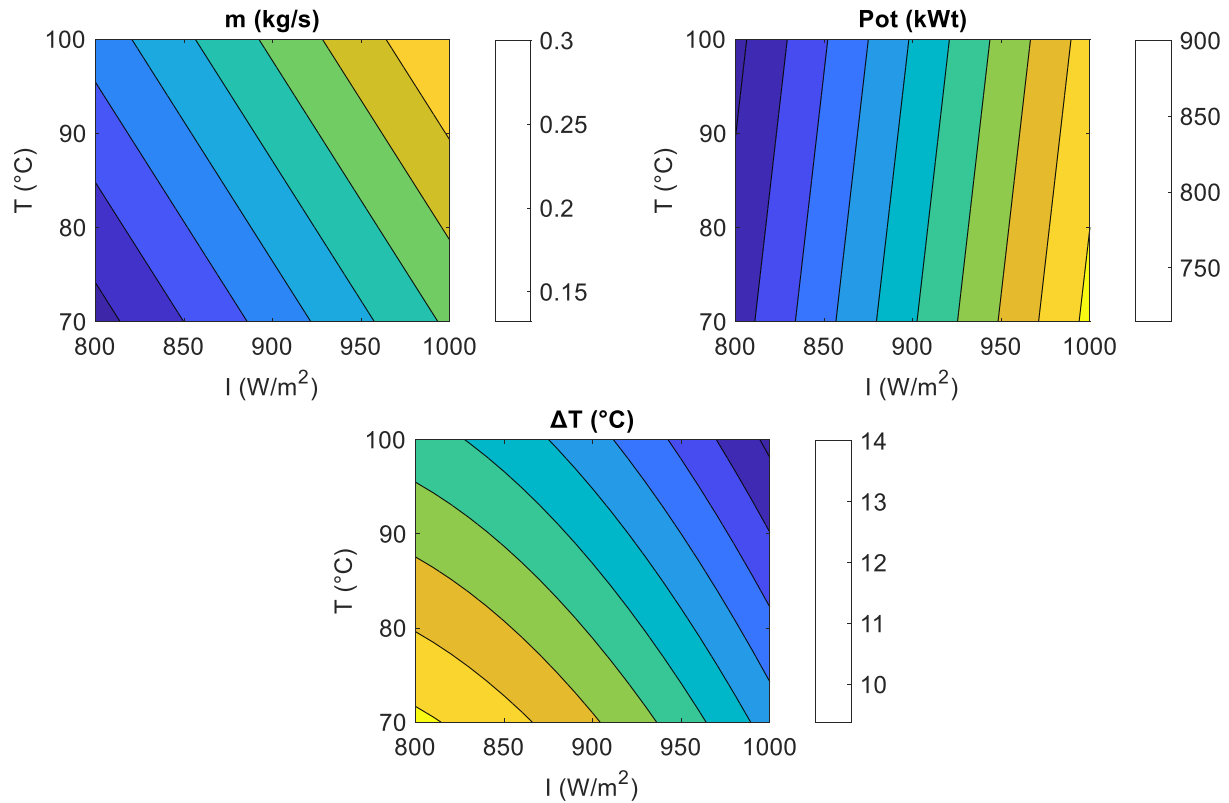


Fig. 4.28 – Level curves for mass flow, thermal power, and over-heating temperature difference.

4.5 Nomenclature

General symbols

D_a	Diameter at a boundary (m)
F_c	Soiling factor (dimensionless)
G	Flow rate (GPM)
I_b	Direct beam solar radiation (W/m^2)
$K(\theta)$	Incident angle modifier (dimensionless)
k	Thermal conductivity (W/m K)
\dot{m}_x	Maximum mass flow rate (kg/s)
Pot_{sal}	Thermal power (kW_{th})
T_a	Ambient temperature (°C)
T_{out}	Outlet temperature (°C)
T^*	Reduced temperature ($m^2 K/W$)
x	Steam quality (dimensionless)

Greek symbols

α	Absorptance (dimensionless)
γ	Interception factor (dimensionless)
ΔT	Difference temperature (°C)
ΔT_{amb}	Average fluid temperature above ambient (°C)
θ	Incidence angle (rad)
ε	Emittance (dimensionless)
η	Thermal efficiency (%)
η_0	Peak thermal efficiency (%)
ρ	Reflectance (dimensionless)
τ	Transmittance (dimensionless)

4.6 References

- [1] Moss T, Brosseau D. Final test results for the Schott HCE on a LS-2 collector. Albuquerque (NM, USA): SANDIA; 2005. 22p. Report No.: SAND2005-4034.
- [2] Dudley V, Kolb G, Sloan M, Kearney D. SEGS LS2 solar collector: Test results. Springfield (VA, USA): SANDIA; 1994. 140p. Report No.: SAND94-1884.
- [3] Valenzuela L, López-Martín R, Zarza E. Optical and thermal performance of large-size parabolic-trough solar collectors from outdoor experiments: A test method and a case study. *Energ.* 2014;70:456–64.
- [4] Fernández-García A, Zarza E, Pérez M, Valenzuela L, Rojas E, Valcárcel E. Experimental assessment of a small-sized parabolic trough collector: CAPSOL Project. *Proceedings of EuroSun 2010*; 2010.
- [5] Fernández-García A. Optimization tools for design and evaluation of parabolic trough solar collectors for thermal energy supply at temperatures below 250 °C. Practical approach to CAPSOL prototype [Optimización de herramientas para el diseño y evaluación de captadores solares cilindroparabólicos para el suministro de energía térmica a temperaturas inferiores a 250 °C. Aplicación práctica al prototipo CAPSOL] [Ph.D. tesis]. Almería (ES): Universidad de Almería; 2013. 346 p.
- [6] Tagle-Salazar PD, Nigam KDP, Rivera-Solorio CI. Heat transfer model for thermal performance analysis of parabolic trough solar collectors using nanofluids. *Renew Energ.* 2018;125:334-43.

- [7] Bretado M. Application of nanofluids in a parabolic trough solar concentrator for thermal energy generation [Aplicación de nanofluidos en un concentrador solar parabólico lineal para aprovechamiento de energía térmica] [master's thesis]. Monterrey (MX): Tecnológico de Monterrey; 2017.
- [8] Eck M, Zarza E, Eickhoff M, Rheinländer J, Valenzuela L. Applied research concerning the direct steam generation in parabolic troughs. *Solar Energ.* 2003;74:341-51.
- [9] Biencinto M, González L, Valenzuela L. A quasi-dynamic simulation model for direct steam generation in parabolic troughs using TRNSYS. *App Energ.* 2016;161:133-42.
- [10] Lobón D, Baglietto E, Valenzuela L, Zarza E. Modeling direct steam generation in solar collectors with multiphase CFD. *App Energ.* 2014;113:1338-48.
- [11] Tagle PD, Valenzuela L, Rivera CI, Agraz A. Feasibility análisis of a steam generation system based on small-aperture parabolic trough collectors applied to a dairy plant [Análisis de factibilidad de un Sistema de generación de vapor basado en captadores cilindroparabólicos de pequeña apertura aplicado a una fábrica de productos lácteos]. In: Asociación Española de Energía Solar ,Editor. Proceedings of the 12th Iberoamerican Congress of Solar Energy – CIES 2018; 2018 June 20-22; Madrid (Spain). p. 491-8.
- [12] Weather Spark. Weather of July 26 at Guadalajara (Mexico) [Tiempo promedio el 26 de Julio en Guadalajara (México)] [internet]. [cited 2018 May 4]. Available from: <https://es.weatherspark.com/d/3866/7/26/Tiempo-promedio-el-26-de-julio-en-Guadalajara-M%C3%A9xico#Sections-Wind>.
- [13] Ulloa H, García M, Pérez A, Meulenert A, Avila D. Weather and solar radiation in big cities: Metropolitan zone of Guadalajara (Jalisco state, Mexico) [Clima y radiación solar en las grandes ciudades: zona metropolitana de Guadalajara (estado de Jalisco, México)]. *Investigaciones Geográficas.* 2011;56:165-75.

Chapter 5 Conclusions

Conclusions

A mathematical model for predicting thermo-hydraulic behavior in PTCs is presented. Comparison with experimental data of different PTCs used in market are also analyzed as validation of the mathematical model. Different HTFs were considered according to test results found in the literature. A variety of operational and ambient conditions were simulated in order to test the mathematical model under the variation of any parameter (geometrical, optical, materials, operation, weather, etc). Furthermore, an analysis of thermal behavior for a steam generation plant was presented in order to predict mass flow of steam and thermal power of the system for a variety of solar radiation and inlet temperature of the fluid to the solar field, and to determine variability of key system's parameters.

Pressurized water, Syltherm 800 thermal oil, and water/ Al_2O_3 nanofluid were considered in simulation using single-phase approach of the model. Two mathematical models for determining heat transfer coefficient were analyzed in case of nanofluid. Comparison of simulated outlet temperature, temperature difference in collector, average temperature above ambient, and thermal efficiency show good agreement with experimental data in all cases. In general, the higher variability in simulations was obtained in thermal efficiency. The principal source of error in simulations may be the over estimation of convective losses to the ambient since it is modeled as cross-flow external forced convection with wind velocity given in experiments. Nevertheless, its variability is comparable with experimental uncertainties. Considering all cases presented, thermal efficiency difference between simulations and experiments (absolute error) is around from 2% to 3%.

Pressurized water was considered to validate the model under phase-change phenomena (two-phase approach). In this case, simulated results of temperature and pressure were compared with experiments. The results show good agreement of temperature prediction, but a slightly difference in pressure prediction. Prediction of pressure drop tends to fail at high steam quality conditions (over 70%). The model also can predict where phase change will occur, so it is possible to know where boiling will start and end for a given PTC thermal system under steady-state conditions. Average absolute errors for temperature were around 2.1 °C, and 0.1 barg for pressure drop.

The pre-design analysis presented in Section 4.4 showed that the model can predict thermal behavior of a direct steam generation system. The analysis can be used to determine sensitivity of operational parameters. It was found that outlet pressure shows high variability with solar radiation, compared to insignificant variation respect to ambient temperature and/or wind velocity. It was possible to obtain relationships for mass flow of supplied steam, thermal power of the solar field, and over-heating temperature of the steam as function of solar radiation and inlet temperature of the system with a good adjustment (high determination coefficient).

Recommendations

A key recommendation is to stay clear about measured and/or estimated optic properties. It was noticed that optic parameters have a high impact on thermal behavior when comparing experimental data with simulation results. It is important to simulate thermal system with accurate optic properties. In addition, optics are an input of the model. For thermal evaluation of non-characterized collectors, a recommended procedure may be the estimation of geometric/optic parameters (such as intercept factor, incident angle modifier, or error coefficients) using ray-tracing techniques, and optic properties (absorptance, emittance, transmittance) using data found in the literature.

Another observation about the thermal model is its over-estimation of convective heat losses. Cross-flow modeling does not always occur in the receiver surroundings. It is important to determine a good estimation of wind velocity near the solar field in order to obtain an accurate result in simulations. Nevertheless, with measured wind velocities (as shown before) it is possible to obtain a “worst case” conservative solution.

A very important factor to consider in evaluation of thermal systems for direct steam generation is convergence. The complexity of combining single-phase and two-phase heat transfer and hydraulics sometimes make “automatic” prediction of phase change too difficult. A procedure to simulate direct steam generation systems may be as follow:

- a) Fix steam quality as inlet conditions for all collectors.
- b) Run a simulation
- c) At the collector where is detected an error (due to phase change), modify steam quality. Extend it to the last collector.
- d) Run a simulation again.
- e) If there is a new error, go to c). Stop simulating when simulation finishes with no errors.

In order to simulate direct steam generation systems under a variety of inlet conditions, a recommended procedure is to save simulations as different EES files. This is also useful when tracing data of simulated results. There are many other variables to consider in direct steam generation compared with single-phase analysis. This also prevent errors whit phase-change prediction (as explained before).

Future work

Three global ideas may be considered as future work: to adapt the model to analyze thermal systems under transient conditions, adapt direct steam generation analysis with other operational modes, and re-write the code for better automatic prediction of phase change. Transient-state analysis can also estimate a transient-response characteristic of collectors: time constant. According to standards, experiments are carried out during a time equivalent or higher to 4 times time constant. Determining simulated time constant of a collector can be useful for designing of experiments to obtain efficiency curve.

Another approach is to simulate a solar field under transient state and estimate total energy converted during a time lapse. Software such as TRNSYS can be linked with EES codes, so it is possible to estimate energy conversion with a given operational planning. Simulation of direct steam generation systems under transient conditions with experimental validation may be a good research topic.

The model presented can simulate direct steam generation systems only under once-through operational mode. A thermal model for recirculation and injection modes can be useful for designing those kind of systems. It is known that recirculation and injection modes have advantages over once-through mode. Recirculation mode has a separation tank, which acts as a buffer (when operated in transient conditions), increasing thermal inertia and preventing dry-out effects in boiling section. The principal advantage of injection mode is its control and stability of outlet conditions. The major disadvantages of recirculation and injection modes are their complex design. A model that simulate recirculation/injection systems can reduce time and effort of design process of a direct steam generation system. Another topic of research is the improvement of pressure drop modeling in two-phase flow. It was shown that the model used tends to under-estimate pressure drop at high quality of wet steam.

Finally, the consideration of re-writing the EES code to get automatic prediction of thermal behavior of direct steam generation systems becomes from the experience of the first design of the code. As explained in Section 3.1.5, two-phase flow modeling fails at very low or very high steam quality. Besides that, the algorithm used to calculate average properties does not predict automatically phase change phenomena. This is the section of the EES code that should be modified.

Appendix A General user manual of windows in Engineering Equation Solver

This appendix shows a general procedure to realize thermo-hydraulic analysis using developed Engineering Equation Solver (EES) code. The analysis is divided into two approaches: single-phase and two-phase flows. Analysis with single-phase flows includes water (without phase-change), thermal oils, molten salts, and Al₂O₃/water nanofluid. Analysis with nanofluids includes both single-phase and Nusselt-correlation approach.

A.1 Input data window

The input data window is divided into three sections: ambient conditions data, collector design data, and system description data. These sections of the input data windows were previously explained in Section 3.2.2. The section that change according to the analysis is the system description section, depending on the fluid used in the analysis (inlet data sub-section). Figure A.1 shows the three types of inlet data sub-section according to heat transfer fluid used. Basic required data are fluid, temperature, pressure, and flow rate at inlet of the system. Other required data are the nanoparticle characteristics (volume concentration and diameter) when nanofluids are used, or inlet steam quality when phase-change is used. EES uses flags for quality of sub-cooled liquid and over-heated steam as -100 and 100 respectively. EES sends an error message when temperature, pressure and quality does not match at inlet (two-phase flow).

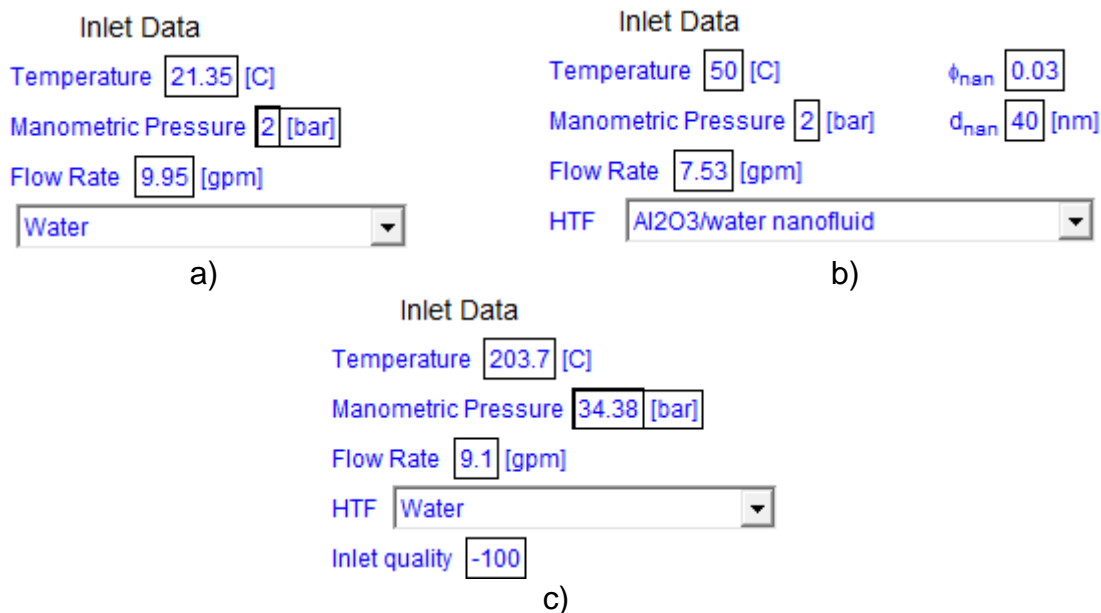





Fig. A.1 – Inlet data in system description section for different types of analysis. a) Single-phase flow without nanofluids, b) Single-phase flow using nanofluids, c) Two-phase flow

A.2 Solution in Single-phase flow

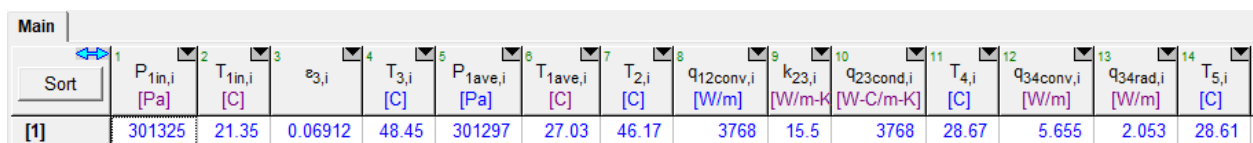
The procedure to make an analysis using single-phase is as follow:

1. Press F2, or the “solve” icon .
2. Press Ctrl + U, or the “solution window” icon . A window as shown in Figure A.2 will appear. It shows values of non-matrix variables (inputs and outputs) and internal variables of functions (only last evaluation).
3. Press Ctrl + Y, or the “arrays table” icon . A window as shown in Figure A.3 will appear. It shows matrix variables (temperatures, pressures, heat transfer flows, and others) for each section of collector according to number of collectors per row in matrix data sub-section (inlet data section).



Variable	Value	Variable	Value	Variable	Value
AbsorberMaterial\$	'321H'	α_{abs}	0.955	$\alpha_{abs,UD}$	0.96
AnnulusGas\$	'Air'	A_{cs}	0.003421 [m ²]	$A_{cs,brac}$	0.00015 [m ²]
CollectorType\$	'User-Defined'	C_r	21.94	Dir _{HCE,UD}	1
D ₂	0.066 [m]	D _{2,UD}	0.066 [m]	D ₃	0.07 [m]
D ₄	0.119 [m]	D _{4,UD}	0.119 [m]	D ₅	0.125 [m]
D _{brac}	0.00566 [m]	D _n	0.066 [m]	D _p	0.0508 [m]
$\epsilon_{3,100,UD}$	0.04	$\epsilon_{3,400,UD}$	0.2327	ϵ_4	0.86
ϵ_{sky}	0.8016	Error _{UD}	1	$\eta_{EffectiveOptEff}$	80.09
Fluid\$	'water'	f_p	1.49 [m]	$f_{p,UD}$	1.49 [m]
GlazingIntact\$	'Yes'	H _p	5.96	IAM	1
K ₄₅	1.04 [W/m ² K]	K _{a,1}	0.000884	K _{a,2}	-0.00005369
LA _r	0.003811 [ha]	LA _t	0.003811 [ha]	L _c	7.9 [m]
m	0.6265 [kg/s]	n _b	3	n _{columns}	1
OptEff _{abs}	0.8209	OptEff _{env}	0.8463	Φ_r	77.97
P _a	0.0001 [atm]	P _{amb}	1 [atm]	P _{brac}	0.106 [m]
q _{3SolAbs}	3780 [W/m]	q _{5SolAbs}	81.61 [W/m]	q _i	4822 [W/m]
Reflectivity	9	RH	70 [%]	P _{mirror, clean,UD}	0.93
S	5.308	SelectiveCoating\$	'Solel UVAC Cermet (SNL test avg)'	Shadowing _{UD}	0.91
Θ	0 [degrees]	Θ_m	0.8132	TrackingError _{UD}	1
T ₇	17.01 [C]	T _{DP}	12.43 [C]	T _{in}	21.35 [C]
v _{1volg}	9.95 [gpm]	v ₆	2.011 [m/s]	W _a	4.824 [m]
x _{in}	-100				

Fig. A.2 – Solution window






Sort	1	2	3	4	5	6	7	8	9	10	11	12	13	14
	P _{1in,i} [Pa]	T _{1in,i} [C]	$\epsilon_{3,i}$	T _{3,i} [C]	P _{1ave,i} [Pa]	T _{1ave,i} [C]	T _{2,i} [C]	q _{12conv,i} [W/m]	k _{23,i} [W/m-K]	q _{23cond,i} [W-C/m-K]	T _{4,i} [C]	q _{34conv,i} [W/m]	q _{34rad,i} [W/m]	T _{5,i} [C]
[1]	301325	21.35	0.06912	48.45	301297	27.03	46.17	3768	15.5	3768	28.67	5.655	2.053	28.61

Fig. A.3 – Arrays table

When desired various analysis is preferable to make a parametric analysis. This kind of analysis depends on which input variables are desired to change (parametrized) and compare results. For more information about parametric analysis, see Appendix B.

A.3 Solution in two-phase flow

The procedure for two-phase flow is similar to single-phase flow. Additional recommendation is to limit pressure of the fluid between atmospheric and critical pressure. Procedure of manual prediction of phase-change is as follow.

1. Press F9, or “variable info” icon . Go for the steam quality variables and fix lower and upper values as inlet steam quality, as shown in Figure A.4. Then press Ok.
2. Run the analysis (press F2, or the “solve” icon ).
3. If an error message (as shown in Figure A.5) appears, it indicates that phase change occurs at a collector or interconnecting piping. Go to “arrays table” (press Ctrl + Y, or the icon ) and check where steam quality has not been calculated (Figure A.6).
4. Change lower and upper limits of steam quality from the point detected previously. Take into account that phase-change can occur at inlet, average, or outlet of a collector or interconnecting piping.
5. Repeat from step 2 until the error message does not appear.

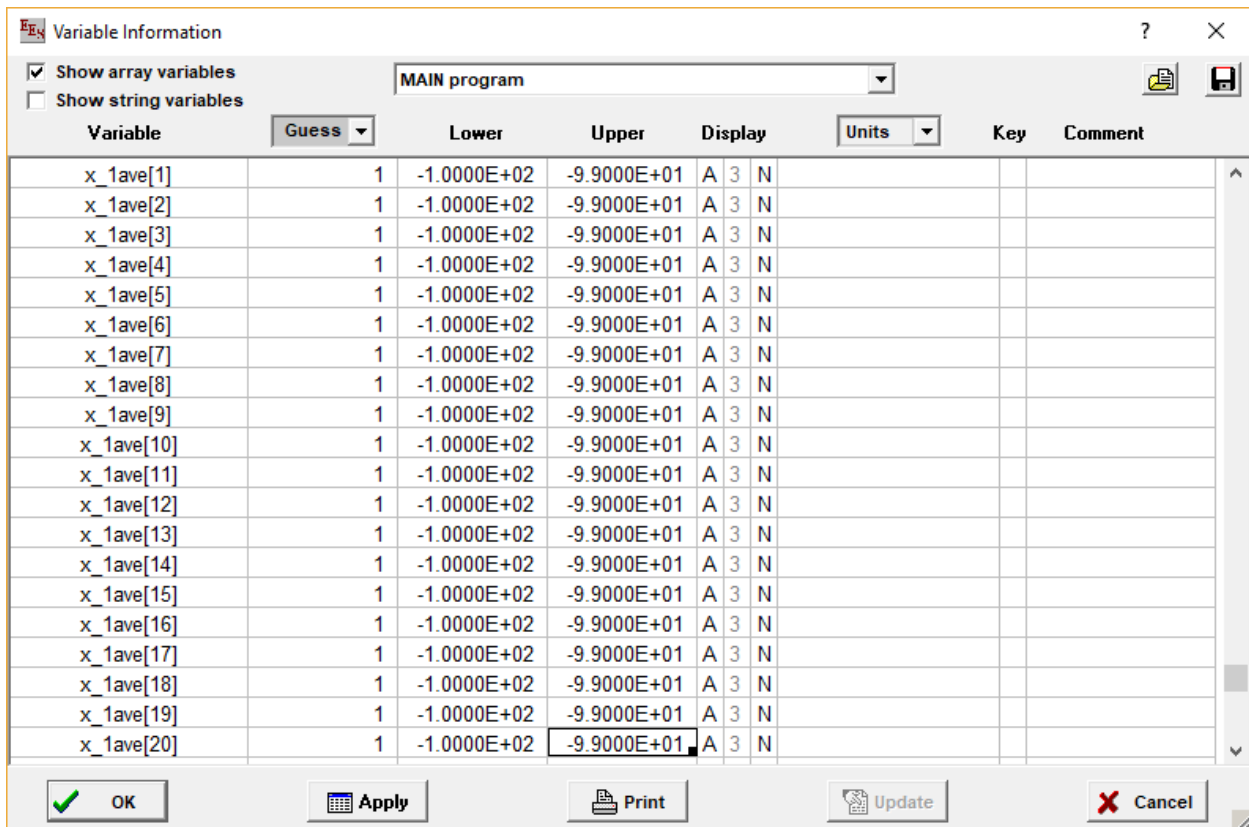


Figure A.4 – Fixing limits for manual phase-change prediction

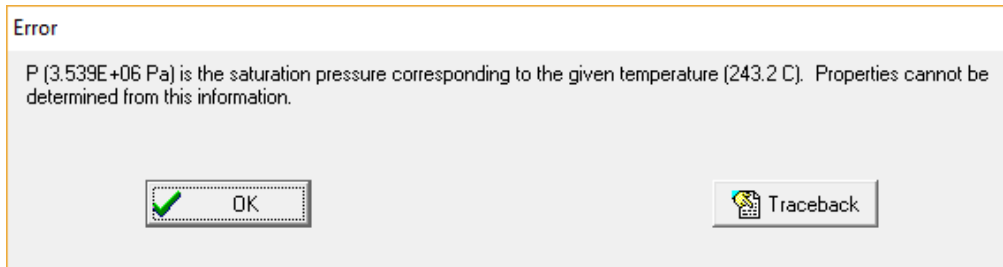


Figure A.5 – Error message for manual phase-change prediction

Main				
Sort	33 FluidStatus _i	34 X _{1ave,i}	35 X _{1in,i}	36 X _{1out,i}
[1]	liquid	-100	-100	-100
[2]		-99		
[3]		-99		
[4]		-99		


No description of fluid status in collector number 2, then there occurs phase-change.

Figure A.6 – Detecting phase-change

Lower and upper limits of phase change are: [-100,-99] for sub-cooled liquid, [0.001,0.999] for wet-steam, and [99,100] for over-heated steam.

Appendix B Parametric analysis in Engineering Equation Solver

Parametric analysis is useful when users would like to make an analysis varying one or some variables. This option allows to make many calculations as one, reducing computational time. The first step of parametric analysis is to deactivate the variables to be parametrized. The process is shown below:

1. Go to the diagram window
2. Click on  (diagram window icon)
3. Double-click on the variable to be parametrized. The variable will be shown inside a red rectangle.
4. A window (Figure B.1 a) will appear, then click on “Text” option and change the text shown (Figure B.1 b). Press “OK”.
5. The variable will be deactivated, showing the diagram window as shown in Figure B.1 c.

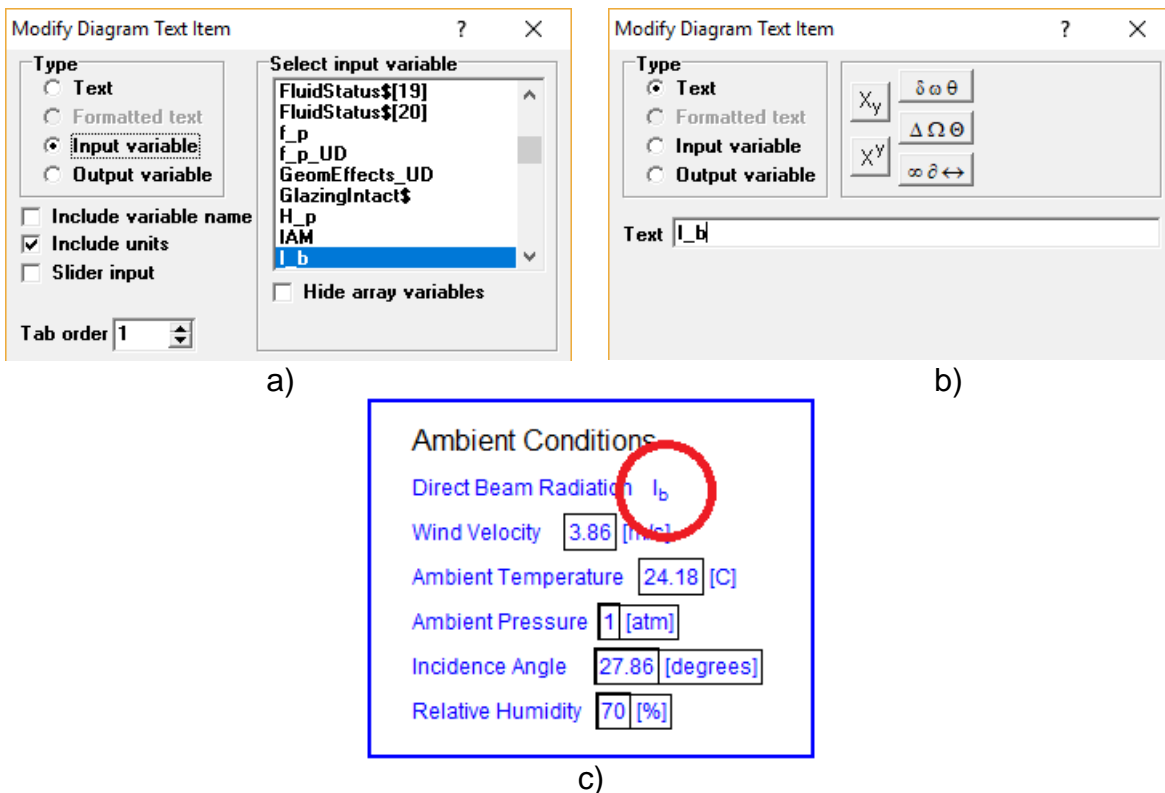



Fig. B.1 – Windows for parametrization. a) selecting the variable, b) deactivating the variable, c) Variable deactivated.

Later, pressing icon , a new parametric table will be defined. Figure B.2 shows the definition of the new parametric table. First, input variables (parametric) and outputs should be selected from the list and added to the table. Then, the values of the parametric variables should be defined. Clicking on the black triangle right up the parametric

variables (Figure B.3 a), the values can be defined by lower-upper values and by four ways as shown in Figure B.3 b. Then, click on “OK”. Finally, clicking on the green triangle (solve table) of the parametric table, the analysis will start.

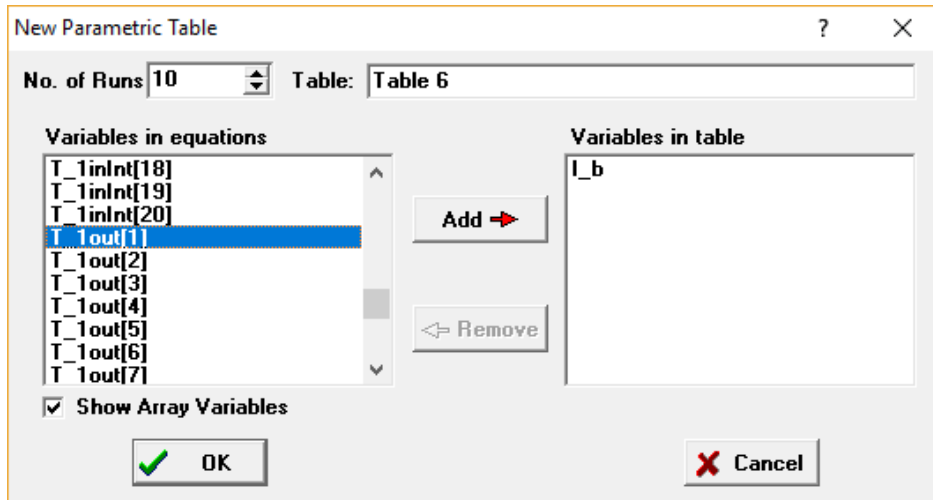
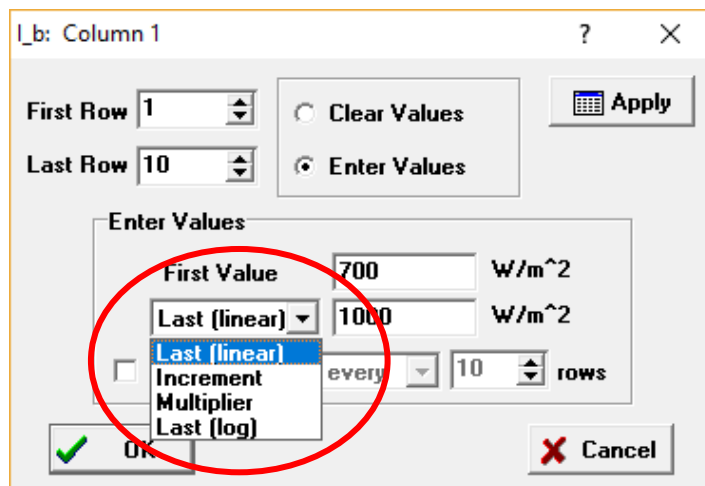


Fig. B.2 – Defining new parametric table

	1	2
	I_b [W/m ²]	$T_{1out,1}$
Run 1		
Run 2		
Run 3		
Run 4		
Run 5		
Run 6		
Run 7		
Run 8		
Run 9		
Run 10		

a)



b)

Fig. B.3 – New parametric table. a) Table, b) defining values of parametric variables

Published papers

Curriculum Vitae

Doctoral's student Pablo Daniel Tagle Salazar was born in Guayaquil, Ecuador, on May 10th, 1985. He earned his Mechanical Engineering degree from *Escuela Superior Politécnica del Litoral* (Gustavo Galindo campus) in May 2011. He has worked in many mechanical projects, principally for Holcim Ltmd. and Unilever Andina in Ecuador. His work was focus on structural analysis, design of piping systems, and other general projects for retrofitting processes in industry. Later, he was accepted in the graduate programs in Energy Engineering in January 2013. His main area of interest is solar thermal energy. Finally, he has specialized in parabolic trough collector technology during the Doctoral's program.

This document was typed in using Microsoft Word by Pablo Daniel Tagle Salazar